

**UNIVERSIDADE DE SÃO PAULO  
ESCOLA DE ENGENHARIA DE SÃO CARLOS**

**João Paulo Eguea**

**Estudo da aplicação de uma winglet de camber variável  
em um jato executivo**

**São Carlos**

**2019**



**UNIVERSIDADE DE SÃO PAULO  
ESCOLA DE ENGENHARIA DE SÃO CARLOS**

**João Paulo Eguea**

**Genetic optimization and experimental validation of a  
camber morphing winglet**

**São Carlos**

**2019**



**João Paulo Eguea**

**Estudo da aplicação de uma winglet de camber variável  
em um jato executivo**

Dissertação apresentada à Escola de Engenharia de São Carlos da Universidade de São Paulo, para obtenção do título de Mestre em Ciências - Programa de Pós-Graduação em Engenharia Mecânica.

Área de concentração: Aeronaves

Orientador: Prof. Dr. Fernando Martini Catalano

ESTE EXEMPLAR TRATA-SE DA  
VERSAO CORRIGIDA. A VERSAO  
ORIGINAL ENCONTRA-SE  
DISPONIVEL JUNTO AO  
DEPARTAMENTO DE ENGENHARIA  
MECANICA DA USP

EESC-USP

**São Carlos**

**2018**

AUTORIZO A REPRODUÇÃO E DIVULGAÇÃO TOTAL OU PARCIAL DESTE TRABALHO, POR QUALQUER MEIO CONVENCIONAL OU ELETRÔNICO, PARA FINS DE ESTUDO E PESQUISA, DESDE QUE CITADA A FONTE.

Ficha catalográfica elaborada pela Biblioteca Prof. Dr. Sérgio Rodrigues  
Fontes da EESC/USP

E32e                    Eguea, João Paulo  
                          Estudo da aplicação de uma winglet de camber variável em um jato executivo / João Paulo Eguea; orientador Fernando Martini Catalano. -- São Carlos, 2019.

                          Dissertação (Mestrado) - Programa de Pós-Graduação em Engenharia Mecânica e Área de Concentração em Aeronaves -- Escola de Engenharia de São Carlos da Universidade de São Paulo, 2019.

                          1. Jato executivo. 2. Estruturas adaptáveis.  
3. Winglet. 4. Otimização. 5. Algoritmo genético.  
6. Mapeamento de escoamento. 7. Arrasto induzido.  
I. Título.

**João Paulo Eguea**

**Genetic optimization and experimental validation of a  
camber morphing winglet**

Dissertação apresentada à Escola de Engenharia de São Carlos da Universidade de São Paulo, para obtenção do título de Mestre em Ciências - Programa de Pós-Graduação em Engenharia Mecânica.

Área de concentração: Aeronaves

Supervisor: Prof. Dr. Fernando Martini Catalano

THIS COPY IS FROM THE  
CORRECTED VERSION. THE  
ORIGINAL VERSION IS AVAILABLE  
AT THE DEPARTMENT OF  
MECHANICAL ENGINEERING,

EESC-USP

**São Carlos**

**2018**

I AUTHORIZE THE TOTAL OR PARTIAL REPRODUCTION OF THIS WORK,  
THROUGH ANY CONVENTIONAL OR ELECTRONIC MEANS, FOR STUDY AND  
RESEARCH PURPOSES, SINCE THE SOURCE IS CITED.

Catalog card prepared by Patron Service at "Prof. Dr. Sergio  
Rodrigues Fontes" Library at EESC/USP

E32s Eguea, João Paulo  
Study of the application of a camber morphing winglet  
on a business jet / João Paulo Eguea ; Thesis directed  
by Fernando Martini Catalano. -- São Carlos, 2019.

Master (Thesis) Graduate Program in Mechanical  
Engineering and Research Area in Aircraft -- São Carlos  
School of Engineering, at University of São Paulo, 2019.

1. Midsize business jet. 2. Morphing structures.  
3. Winglet. 4. Optimization. 5. Genetic algorithm.  
6. Seven-hole flow mapping. 7. Induced drag. I. Title.

## FOLHA DE JULGAMENTO

Candidato: Engenheiro **JOÃO PAULO EGUEA**.

Título da dissertação: "Estudo da aplicação de uma winglet de camber variável em um jato executivo".

Data da defesa: 18/03/2019

### Comissão Julgadora:

### Resultado:

Prof. Titular **Fernando Martini Catalano**  
**(Orientador)**  
(Escola de Engenharia de São Carlos/EESC)

APROVADO

Prof. Dr. **Leandro Dantas de Santana**  
(UTWENT/HOlanda)

APROVADO

Dr. **Alexandre Pequeno Antunes**  
(EMBRAER)

APROVADO

Coordenador do Programa de Pós-Graduação em Engenharia  
Mecânica:  
Prof. Titular **Gherhardt Ribatski**

Presidente da Comissão de Pós-Graduação:  
Prof. Titular **Murilo Araujo Romero**



*To my family that always supported me on my journey  
To my friends that followed me on it  
and to my teachers that showed me paths that I was not able see.*



## ACKNOWLEDGEMENTS

I would like to thank the Coordenação de Aperfeiçoamento de Pessoal de Nível Superior (CAPES) which scholarship made the realization of this project possible. My special thanks to Prof. Dr. Fernando Martini Catalano, for being a friend and supervisor, which support, knowledge and experience shared with me as teacher and supervisor guided me as an engineer and researcher. I would like to acknowledge Prof. Dr. Alvaro Martins Abdalla for helping me with the genetic algorithm and Andre Luiz Fontes Silva for helping me with the BLWF code. My acknowledgment to the Center for Mathematical Sciences Applied to Industry (CeMEAI) funded by FAPESP (grant 2013/07375-0) for providing computational resources for this work. Special thanks for the friendship, solicitude, aid and shared knowledge in the manufacture, assembly, maintenance and operation of the necessary equipment for the experiments of the technicians José Claudio Pinto de Azevedo, Mário Sbampato and Osnan Ignacio Faria. My affectionate thanks to Gisele Aparecida Poppi Lavadeci, secretary of the Department of Aeronautical Engineering, who always helped me with paperwork and was present for a good conversation. I would like to acknowledge the São Carlos School of Engineering Library staff, for checking the formatting and the referencing style of this text. I would like to thank my friends and laboratory colleagues, the engineers Daniel Acevedo Giraldo, Gabriel Pereira Gouveia da Silva, Laura Botero Bolivar, Lourenço Tércio Lima Pereira not only for the support on this research but also for this priceless friendship.

My special thanks for Bruno Lima, Daniel Tozadore, Danilo Barbosa, Danilo Pallamin, Eric Schneider, Pedro Nobile and Thiago Benedito for being my friends every day, sharing a home and life daily; it was a pleasure to have you all this time, thanks for your love, patience and support. I am grateful for the special friendship of Gabriela Cassão, Eduardo Chinaglia, Letícia Cursini, Luiz Ferreira, Nathália Santos, Pedro Suzuki, Rafael Pedrini, Rafael Santos, Tainá Andrello, Thiago Ercolin and Vitor Gioia. All of you matter the most to me.

My gratitude to my parents João Antonio Eguea and Jucelene Alba Eguea for being the cornerstone of my life, nothing was possible without you, whose I give all my love and my effort to make you proud; and my brother João Guilherme Eguea for being my first friend and my lifelong partner.



*“As invenções são, sobretudo, o resultado de um trabalho teimoso.”*

*Alberto Santos Dumont*



## ABSTRACT

EGUEA, J. P. **Genetic optimization and experimental validation of a camber morphing winglet.** 2019. 117p. Dissertation (Master) - São Carlos School of Engineering, University of São Paulo, São Carlos, 2019.

International aviation regulations on emissions are becoming more strict. Improvements goals on fuel efficiency demand development of technologies capable of reducing fuel consumption and gas emissions. Morphing structures capability to adapt their aerodynamic shape for optimal condition in flight brings potential for reduction of aircraft drag and operating fuel consumption, minimizing gas emissions and fuel expenses. This study presents an investigation on the impact of a camber morphing winglet on midsize business jet using numerical simulation and wind tunnel experiments. A genetic algorithm was used to optimize the winglet sections camber for different flight conditions. Optimized geometries achieved total drag reduction of up to 0.58% compared to original winglet for single condition optimization, reaching up to 7 % reduction on consumed fuel on a typical mission. This efficiency improvement allows aircraft to carry 900 kg additional load, comprising the morphing system and extra payload. There is an indication of even better results for applications on a bigger commercial jet. Presented methodology is also suitable for new winglet fixed geometry design or incorporating morphing technology. Aerodynamic balance force measurements showed that optimized winglets increased the wing effective aspect ratio ( $AR_{eff}$ ), reducing the lift-induced drag, and maximum lift coefficient ( $C_{L_{max}}$ ). However, maximum lift to drag ratio ( $\frac{L}{D_{max}}$ ) was reduced on  $C_L$  optimization region due to flow differences between optimization and wind tunnel conditions. Aerodynamic efficiency improvement was found for greater lift coefficients ( $C_L$ ). Reductions on wing tip vortex size and intensity due to winglet installation are seen on measured vorticity map, showing lift-induced drag reduction according to Maskell's equation. Parabolic drag polar and Maskell's equation methods were used for lift-induced drag calculation, using balance force and flowing mapping data for calculations. The presented concept showed considerable aircraft performance improvement, using a feasible device with greater certification ease than other morphing structures concepts, once the failure of this system would not compromise flight safety. Further investigation using computational fluid dynamics (CFD) and wind tunnel experiments is necessary to develop and test a functional camber morphing winglet device.

**Keywords:** Midsize business jet. Morphing structures. Winglet. Optimization. Genetic algorithm. Seven-hole flow mapping. Lift induced drag.



## RESUMO

EGUEA, J. P. **Estudo da aplicação de uma winglet de camber variável em um jato executivo**. 2019. 117p. Dissertação (Mestrado) - Escola de Engenharia de São Carlos, Universidade de São Paulo, São Carlos, 2019.

Regulamentações internacionais sobre emissões estão se tornando mais rigorosas. Metas de melhoria da eficiência de consumo de combustível demandam o desenvolvimento de tecnologias capazes de reduzir o consumo e emissões de gases. Estruturas capazes de adaptar sua forma aerodinâmica para condição ótima em voo trazem potencial de redução do arrasto e consumo de combustível da aeronave, minimizando as emissões de gases e gastos com combustível. Este estudo apresenta uma investigação sobre o impacto de uma winglet de camber variável em um jato executivo da categoria mid size utilizando simulação numérica e experimentos em túnel de vento. Um algoritmo genético foi usado para otimizar o camber das seções para diferentes fases de voo. As geometrias otimizadas reduziram o arrasto total em até 0.58% comparadas a winglet original na otimização de condição única, alcançando até 7% de redução no combustível consumido em missão típica. Essa melhoria de eficiência permite a aeronave carregar 900 kg de carga adicional, composta pelo sistema de adaptação e carga paga extra. Há uma indicação de resultados ainda melhores para aplicação em um jato comercial maior. A metodologia apresentada é apropriada para projeto de uma nova winglet de geometria fixa ou que incorpore a tecnologia de adaptação. Medidas de força com balança aerodinâmica mostraram que as winglets otimizadas aumentaram o alongamento efetivo da asa ( $AR_{eff}$ ), reduzindo o arrasto induzido, e o coeficiente de sustentação máximo ( $C_{L_{max}}$ ). No entanto, a máxima razão entre sustentação e arrasto ( $\frac{L}{D_{max}}$ ) foi reduzida dentro do intervalo de  $C_L$  da otimização devido as diferenças entre as condições do escoamento na otimização e no túnel de vento. Melhoria na eficiência aerodinâmica foi obtida para coeficientes de sustentação ( $C_L$ ) maiores. Reduções no tamanho e intensidade do vórtice de ponta de asa são vistas nos mapas de vorticidade medidos, mostrando redução do arrasto induzido segundo a equação de Maskell. Os métodos da polar de arrasto parabólica e da equação de Maskell foram usados para o cálculo do arrasto induzido, utilizando nos cálculos os dados de força da balança e o mapeamento do escoamento. O conceito apresentado mostrou melhoria considerável no desempenho da aeronave, utilizando um sistema factível e com maior facilidade para certificação que outros conceitos de estruturas adaptáveis, uma vez que a falha desse sistema não comprometeria a segurança do voo. Mais estudos são necessárias para desenvolver e testar uma winglet de camber variável funcional.

**Palavras-chave:** Jato executivo. Estruturas adaptáveis. Winglet. Otimização. Algoritmo genético. Mapeamento de escoamento. Arrasto induzido.



## LIST OF FIGURES

Figure 1 – IATA pillars for emissions reductions . . . . .	32
Figure 2 – IATA emissions reductions estimation . . . . .	32
Figure 3 – Boundary layer and viscous drag production . . . . .	35
Figure 4 – Cylinder and airfoil flow separation . . . . .	36
Figure 5 – Airfoil shock wave . . . . .	36
Figure 6 – Wing tip vortex structure . . . . .	37
Figure 7 – Commercial transonic aircraft typical drag components . . . . .	37
Figure 8 – Wing tip devices currently in use on modern aircraft. . . . .	40
Figure 9 – Winglet drag trade off . . . . .	40
Figure 10 – Morphing system representation . . . . .	45
Figure 11 – Generic midsize business jet geometry . . . . .	47
Figure 12 – Winglet geometry and camber adaptable sections . . . . .	47
Figure 13 – Airfoil used on the winglet sections for the morphing optimization . . . . .	47
Figure 14 – Mission profile . . . . .	48
Figure 15 – Forces acting on plane during climb . . . . .	49
Figure 16 – Forces acting on plane during cruise . . . . .	51
Figure 17 – Forces acting on plane during descent . . . . .	52
Figure 18 – Gen representation on the winglet optimization . . . . .	55
Figure 19 – Crossover process example . . . . .	57
Figure 20 – Crossover process example . . . . .	57
Figure 21 – Genetic algorithm optimization process block diagram . . . . .	58
Figure 22 – Population size and number of generations influence on optimum individual fitness . . . . .	59
Figure 23 – $f_1$ surface and maximum compared to GA optimum points . . . . .	60
Figure 24 – $f_2$ surface and maximum compared to GA optimum points . . . . .	60
Figure 25 – $f_3$ surface and maximum compared to GA optimum points . . . . .	61
Figure 26 – $f_4$ surface and maximum compared to GA optimum points . . . . .	61
Figure 27 – Best evolution through the generations for climb condition . . . . .	65
Figure 28 – Best, worst and mean individual fitness evolution through the generations for climb condition . . . . .	66
Figure 29 – Best individual fitness evolution through the generations for heavy cruise condition . . . . .	66
Figure 30 – Best, worst and mean individual fitness evolution through the generations for heavy cruise condition . . . . .	67
Figure 31 – Best individual fitness evolution through the generations for mid cruise condition . . . . .	67

Figure 32 – Best, worst and mean individual fitness evolution through the generations for mid cruise condition . . . . .	68
Figure 33 – Best individual fitness evolution through the generations for light cruise condition . . . . .	68
Figure 34 – Best, worst and mean individual fitness evolution through the generations for light cruise condition . . . . .	69
Figure 35 – Evolution of sections airfoil of the best and worst individual through the generations for climb condition . . . . .	70
Figure 36 – Evolution of sections airfoil of the best and worst individual through the generations for heavy cruise condition . . . . .	71
Figure 37 – Evolution of sections airfoil of the best and worst individual through the generations for mid cruise condition . . . . .	72
Figure 38 – Evolution of sections airfoil of the best and worst individual through the generations for light cruise condition . . . . .	73
Figure 39 – Fuel consumption for max range mission with additional weight . . . . .	76
Figure 40 – Wind tunnel circuit drawing . . . . .	79
Figure 41 – Wing model dimensions and tunnel coordinate system . . . . .	80
Figure 42 – Prototyped winglet model before surface smoothing and painting . . . . .	80
Figure 43 – Winglet models used on experiment . . . . .	81
Figure 44 – Wing model inside the test section . . . . .	81
Figure 45 – Lift force balance calibration . . . . .	82
Figure 46 – Drag force balance calibration . . . . .	82
Figure 47 – Lift coefficient comparison for $Re = 2.5 \times 10^5$ and $M = 0.07$ . . . . .	84
Figure 48 – Drag coefficient comparison for $Re = 2.5 \times 10^5$ and $M = 0.07$ . . . . .	84
Figure 49 – Lift to drag ratio comparison for $Re = 2.5 \times 10^5$ and $M = 0.07$ . . . . .	85
Figure 50 – Seven-hole drawing with wind tunnel coordinates . . . . .	86
Figure 51 – Wake mapping mesh positioning in relation to the tunnel walls . . . . .	87
Figure 52 – Vector field and $\bar{\omega}_x$ on plane at $c_{ref}$ behind the wing tip trailing edge at $\alpha = 12^\circ$ , $M = 0.07$ and $Re = 2.5 \times 10^5$ for no tip configuration . . . . .	89
Figure 53 – Vector field and $\bar{\omega}_x$ on plane at $c_{ref}$ behind the wing tip trailing edge at $\alpha = 12^\circ$ , $M = 0.07$ and $Re = 2.5 \times 10^5$ for climb configuration . . . . .	89
Figure 54 – Vector field and $\bar{\omega}_x$ on plane at $c_{ref}$ behind the wing tip trailing edge at $\alpha = 12^\circ$ , $M = 0.07$ and $Re = 2.5 \times 10^5$ for heavy cruise configuration . . . . .	90
Figure 55 – Vector field and $\bar{\omega}_x$ on plane at $c_{ref}$ behind the wing tip trailing edge at $\alpha = 12^\circ$ , $M = 0.07$ and $Re = 2.5 \times 10^5$ for mid cruise configuration . . . . .	90
Figure 56 – Vector field and $\bar{\omega}_x$ on plane at $c_{ref}$ behind the wing tip trailing edge at $\alpha = 12^\circ$ , $M = 0.07$ and $Re = 2.5 \times 10^5$ for light cruise configuration . . . . .	91
Figure 57 – Stream function boundary conditions . . . . .	93

## LIST OF TABLES

Table 1 – Airframe technologies for fuel reduction under TRL 4 . . . . .	33
Table 2 – Engine performance parameters . . . . .	54
Table 3 – Engine model validation . . . . .	54
Table 4 – GA parameters used on the camber morphing winglet optimization . . .	59
Table 5 – Test functions for GA validation . . . . .	59
Table 6 – GA validation results . . . . .	62
Table 7 – Parameters of conditions on camber morphing winglet optimization . . .	64
Table 8 – Total drag comparison between baseline and optimized camber morphing winglets . . . . .	73
Table 9 – Induced drag comparison between fixed geometry and optimized camber morphing winglets . . . . .	74
Table 10 – Maximum range mission optimization points parameters . . . . .	75
Table 11 – 1000 NM mission optimization points parameters . . . . .	75
Table 12 – Mission simulation results . . . . .	76
Table 13 – Midsize business jet main dimensions . . . . .	79
Table 14 – Lift coefficient and lift to drag ratio maximum values . . . . .	85
Table 15 – Coefficients of parabolic drag polar fit . . . . .	92
Table 16 – Induced drag at $M = 0.07$ , $Re = 2.5 \times 10^5$ and $\alpha = 12^\circ$ calculated using parabolic drag polar fit . . . . .	92
Table 17 – Induced drag calculation methods comparison . . . . .	94
Table 18 – Induced drag calculation methods comparison at $M = 0.07$ , $Re =$ $2.5 \times 10^5$ and $\alpha = 12^\circ$ . . . . .	94



## LIST OF ABBREVIATIONS AND ACRONYMS

BOW	Basic operating weight
CFD	Computational fluid dynamics
CMW	Camber morphing winglet
DAQ	Data acquisition hardware
DOC	Direct operating cost
EESC	Escola de Engenharia de São Carlos (São Carlos School of Engineering)
FAR	Federal Aviation Regulation
FDM	Fused deposition method
GA	Genetic algorithm
IAS	Indicated air speed
IATA	International Air Transport Association
ICAO	International Civil Aviation Organization
IFR	Instrument Flight Rules
LAE	Laboratório de Aerodinâmica Experimental (Experimental Aerodynamics Laboratory)
MDO	Multi-disciplinary optimization
TRL	Technology readiness level
TOW	Take-off weight
UAV	Unmanned aerial vehicle
USP	University of São Paulo



## LIST OF SYMBOLS

$a$	Speed of sound
$a_0$	Speed of sound at sea level
$AR$	Aspect ratio
$AR_{eff}$	Effective aspect ratio
$b$	Wing span
$C_D$	Drag coefficient
$C_{D_0}$	Zero lift drag coefficient
$C_{D_i}$	Induced drag coefficient
$C_L$	Lift coefficient
$\frac{C_L}{C_D}$	Lift to drag ratio
$C_{L_{cruise}}$	Design cruise lift coefficient
$C_{L_{maneuver}}$	Design maneuver lift coefficient
$C_{L_{max}}$	Maximum lift coefficient
$C_{p_{max}}$	Maximum pressure coefficient
$c_{ref}$	Wing model reference chord
$c_{root}$	Root chord
$D$	Drag force
$e$	Oswald's span efficiency factor
$F$	Individual fitness
$F'$	Scaled individual fitness
$F_{climb}$	Individual fitness on climb condition
$F_{cruise}$	Individual fitness on cruise condition
$F_{descent}$	Individual fitness on descent condition
$g$	Gravity's acceleration

$g_{conv}$	Number of generations set as convergence criteria
$g_{conv_{min}}$	Minimum number of generations to ensure convergence to global optimum
$h$	Flight altitude
$k$	Drag coefficient derivative in relation to lift coefficient squared
$k_1$	Fitness scaling equation angular coefficient
$k_2$	Fitness scaling equation linear coefficient
$L$	Lift force
$\frac{L}{D}$	Lift to drag ratio
$\frac{L}{D_{max}}$	Maximum lift to drag ratio
$M$	Mach number
$M_\infty$	Mach number on far field
$MAC$	Mean aerodynamic chord
$MTOW$	Maximum take-off weight
$p_e$	Elitism percentage
$p_m$	Mutation probability percentage
$n$	Population size
$n_{min}$	Minimum population size to ensure convergence to global optimum
$n_{sample}$	Measurement sample number
$n_{var}$	Number of variables analysed
$O_D(V)$	Drag measurement voltage output
$O_L(V)$	Lift measurement voltage output
$p$	Air pressure
$P_{ind}$	Individual selection probability
$P_{le}$	Morphing leading edge parameter
$P_{te}$	Morphing trailing edge parameter

$P_{total\infty}$	Total pressure on the far field
$P_{total_i}$	Total pressure on $i^{th}$ hole of seven-hole probe
$P_{total_m}$	Mean of all total pressures measured by the seven-hole probe
$q_\infty$	Dynamic pressure on far field
$RoC$	Rate of climb
$RoD$	Rate of descent
$Re$	Reynolds number
$R_L$	Maneuver and cruise lift coefficients ratio
$sum(F')_{pop}$	Sum of the fitness of all population's individuals
$S$	Platform area
$S_{ref}$	Wing model reference area
$S_w$	Wing platform area
$T$	Aircraft thrust
$T_{max}$	Maximum thrust at sea level
$T_{max_{av}}$	Maximum thrust available
$T_{max_{cont}}$	Maximum continuous thrust
$t_{loit}$	Loiter duration
$TSFC$	Thrust-specific fuel consumption
$TSFC_0$	Reference thrust-specific fuel consumption
$U_\infty$	Far field flow velocity
$\vec{u}$	Flow velocity vector
$u_n$	Velocity component normal to reference surface
$u, v, w$	Flow velocities components
$\bar{u}, \bar{v}, \bar{w}$	Velocities components divided by the far field flow velocity
$V$	Air speed
$Var_i$	Genetic algorithm optimization variable

$\frac{x}{c}$ <i>morphed</i>	Morphed airfoil $\frac{x}{c}$ coordinate
$X, Y, Z$	Wind tunnel coordinates
$W$	Aircraft weight
$W_i$	Aircraft instantaneous weight
$W_{initial}$	Aircraft weight at the beginning of cruise
$W_{final}$	Aircraft weight at the end of cruise
$W_{ld}$	Aircraft weight when the aircraft stops at the airport gate
$W_{to}$	Aircraft weight at the end of take-off
$\frac{y}{c}$ <i>c</i>	Morphed airfoil camber line $\frac{y}{c}$ coordinate
$\frac{y}{c}$ <i>l</i>	Airfoil lower side $\frac{y}{c}$ coordinate
$\frac{y}{c}$ <i>l</i> <sub>0.25c</sub>	Airfoil lower side $\frac{y}{c}$ coordinate at $x = 0.25c$
$\frac{y}{c}$ <i>l</i> <sub>0.75c</sub>	Airfoil lower side $\frac{y}{c}$ coordinate at $x = 0.75c$
$\frac{y}{c}$ <i>morphed</i>	Morphed airfoil $\frac{y}{c}$ coordinate
$\frac{y}{c}$ <i>u</i>	Airfoil upper side $\frac{y}{c}$ coordinate
$\frac{y}{c}$ <i>u</i> <sub>0.25c</sub>	Airfoil upper side $\frac{y}{c}$ coordinate at $x = 0.25c$
$\frac{y}{c}$ <i>u</i> <sub>0.75c</sub>	Airfoil upper side $\frac{y}{c}$ coordinate at $x = 0.75c$
$\alpha$	Wing flow incidence angle
$\alpha_p$	Flow incidence angle relative to wind tunnel Y direction
$\alpha_{section}$	Wing section angle of attack
$\alpha_u$	Airfoil upper side morphing angle
$\alpha_l$	Airfoil lower side morphing angle
$\beta_p$	Flow incidence angle relative to wind tunnel Z direction
$\gamma$	Specific heats ratio
$\eta_{overall}$	Engine efficiency
$\lambda$	Tapper ratio
$\Lambda$	Swept angle

$\rho$	Air density
$\rho_0$	Air density at sea level
$\sigma_D$	Drag measurement standard deviation
$\sigma_L$	Lift measurement standard deviation
$\tau$	Air temperature
$\tau_0$	Air temperature at sea level
$\phi_c$	Aircraft climb angle
$\phi_t$	Engine thrust angle in relation to the flight path
$\bar{\Psi}$	Stream function
$\vec{\omega}$	Flow vorticity vector
$\bar{\omega}_x$	Flow vorticity on ZY plane



# CONTENTS

<b>1</b>	<b>PROBLEM DESCRIPTION</b>	<b>31</b>
<b>2</b>	<b>LITERATURE REVIEW</b>	<b>35</b>
<b>2.1</b>	<b>Drag breakdown</b>	<b>35</b>
<b>2.2</b>	<b>Drag reduction technologies</b>	<b>38</b>
2.2.1	Lift independent drag	38
2.2.2	Lift induced drag	39
<b>2.3</b>	<b>Winglet design</b>	<b>40</b>
<b>2.4</b>	<b>Morphing aircraft</b>	<b>43</b>
<b>3</b>	<b>CAMBER MORPHING WINGLET NUMERICAL EVALUATION</b>	<b>45</b>
<b>3.1</b>	<b>Camber morphing concept</b>	<b>45</b>
<b>3.2</b>	<b>Aircraft geometry</b>	<b>46</b>
<b>3.3</b>	<b>Aircraft performance model</b>	<b>48</b>
3.3.1	Climb equations	49
3.3.2	Cruise equations	50
3.3.3	Descent equations	52
3.3.4	Loiter equations	53
3.3.5	Engine model	53
<b>3.4</b>	<b>Optimization algorithm</b>	<b>54</b>
<b>3.5</b>	<b>Aerodynamic Model</b>	<b>62</b>
<b>3.6</b>	<b>Single point optimization</b>	<b>63</b>
3.6.1	Optimization structure	63
3.6.2	Results	64
<b>3.7</b>	<b>Mission optimization</b>	<b>74</b>
<b>4</b>	<b>WIND TUNNEL EXPERIMENT</b>	<b>79</b>
<b>4.1</b>	<b>Aerodynamic forces measurement</b>	<b>81</b>
4.1.1	Methodology	81
4.1.2	Results	83
<b>4.2</b>	<b>Wake mapping</b>	<b>86</b>
4.2.1	Methodology	86
4.2.2	Results	88
<b>4.3</b>	<b>Induced drag calculation</b>	<b>91</b>
4.3.1	Drag polar method	91
4.3.2	Maskell's equation method	92

4.3.3 Methodology comparison . . . . . 94

**5 CONCLUSIONS . . . . . 95**

**BIBLIOGRAPHY . . . . . 97**

**APPENDIX . . . . . 103**

**APPENDIX A – BLWF INPUT FILE EXAMPLE . . . . . 105**

## 1 PROBLEM DESCRIPTION

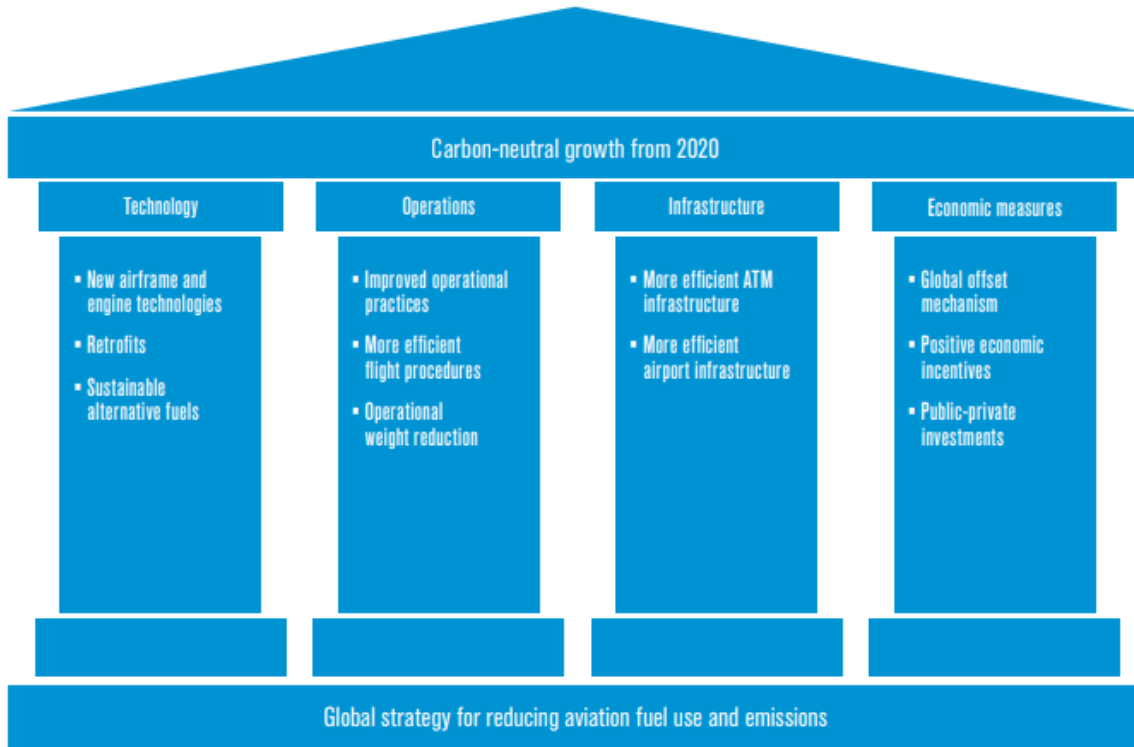
According to the International Air Transport Association (IATA) (2013), 2 % of man-made  $CO_2$  emissions is produced by aviation. These emissions are mainly caused by aircraft engines fuel burn. So, aircraft fuel consumption has direct impact on aviation market sustainability and both environmental and economic aspects of the market are influenced by aircraft efficiency.

The International Civil Aviation Organization - ICAO fuel efficiency improvement goal is proof of the commitment of the aviation industry on reducing its environmental impact. The ICAO resolution A38-18 have the intention of reducing aircraft gas emissions and sets goals on fuel efficiency yearly improvement of 2% and reaching carbon-neutral growth by 2020, affecting new aircraft projects (INTERNATIONAL CIVIL AVIATION ORGANIZATION - ICAO, 2013). Also, expenses with fuel represent a great deal of airliner operational costs, reaching about 20% of the total value (INTERNATIONAL AIR TRANSPORT ASSOCIATION - IATA, 2018). Technologies capable of improving aircraft performance usage affects companies economic aspects, influencing new aircraft buy choice. It also affects charter companies, once those fuel expenses are included on service price. These facts are motivators for researches aiming aircraft drag reduction.

International Air Transport Association - IATA (2013) defined a four-pillar strategy to reach the emissions reduction goals (Figure 1). Figure 2 shows the expected  $CO_2$  emissions reduction expected to be reached with these pillars. The report lists the established and in development technologies, grouping them as airframe, engine and fuel/energy technologies.

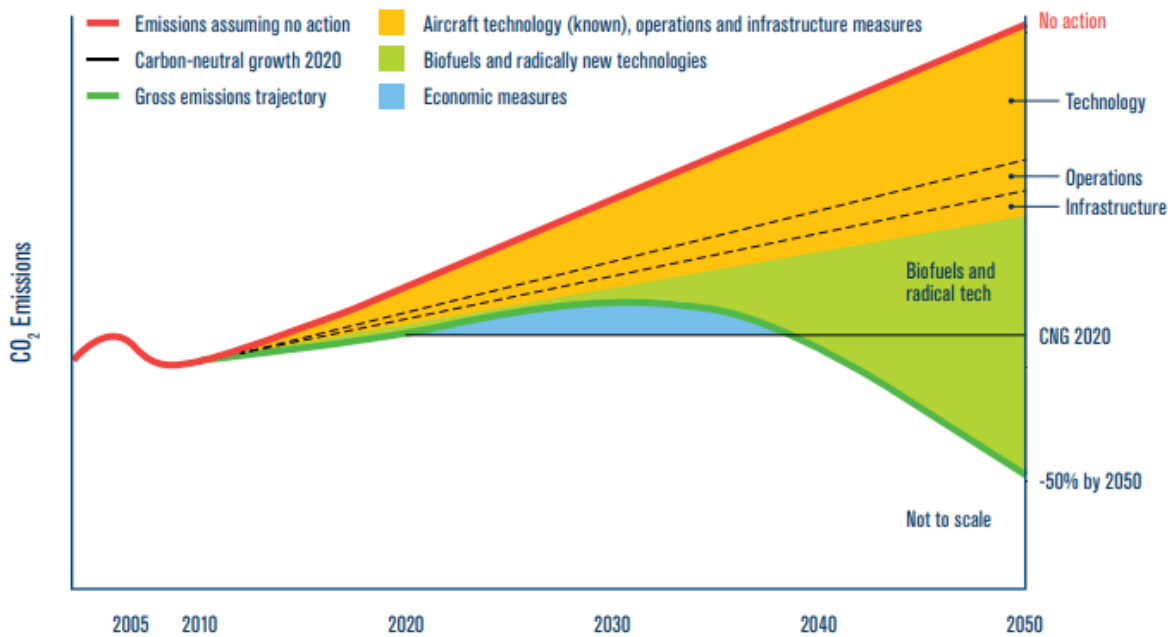
The report gives information about the fuel reduction benefits, development status and calculated technology availability. Considering the technology readiness level (TRL) classification, researches work most on technologies with TRL 1 to TRL 4. Technologies presented on the report at this development stage are shown in Table 1.

Figure 1: IATA pillars for emissions reductions



Source: INTERNATIONAL AIR TRANSPORT ASSOCIATION - IATA (2013)

Figure 2: IATA emissions reductions estimation



Source: INTERNATIONAL AIR TRANSPORT ASSOCIATION - IATA (2013)

Table 1: Airframe technologies for fuel reduction under TRL 4

<b>Technology</b>	<b>Applicability to aircraft program</b>	<b>Fuel reduction benefits</b>	<b>TRL</b>	<b>Availability technology</b>
Truss-Braced Wing/Strut-Braced Wing	after 2020	10 to 15%	2	2028
Hybrid-Wing-Body	after 2020	10 to 25%	4	2026
Cruise-Efficient STOL	after 2020	< 1%	3	2027
Morphing Airframe	after 2020	5 to 10%	3	2027
Flying without landing gear	after 2030	10 to 20%	1	2032
High-Lift / Low-Noise Devices	after 2020	1 to 3%	4	2026
Hinge-less Flap	after 2030	1 to 2%	3	2027
Windowless Design	after 2020	5 to 7%	4	2026
SAFC (Solid Acids as Fuel Cell )	after 2030	1 to 5%	2	2028

Source: INTERNATIONAL AIR TRANSPORT ASSOCIATION - IATA (2013)

Morphing airframe technology presents a TRL 3 and potential fuel consumption reduction of up to 10 %, making this technology attractive research topic. The literature shows potential for development on the topic.

Morphing structures enables the aircraft to adapt its geometry to optimum performance at all flight conditions. The aircraft geometry is limited to one fixed shape, optimized for best performance on a typical mission. This does not imply that it has optimum performance for every flight phase, operating on a sub-optimal condition for flight conditions outside the optimization target. Morphing structures brings the possibility of operating on optimal performance at all flight envelope conditions, reducing wing loads, fuel consumption and gas emissions.

Application of morphing structures on aircraft components can influence the aircraft drag in different ways. The aircraft total drag can be divided into friction, pressure, wave, interference and lift-induced drag. Lift-induced drag component typically accounts for 40% in cruise flight and about 80% on the climb phase (KROO, 2005), representing a considerable part of the total drag during all flight. Devices capable of reducing lift-induced drag component can have great impact on aircraft fuel consumption and gas emissions. This drag component may be reduced by increasing the wing aspect ratio ( $AR$ ) and wing span or using wing tip devices. Winglets are an established technology widely used on aviation industry, capable of reducing tip vortex size, change its position and using the wing tip rotating flow to produce a pressure distribution that results on a forward pointing force. This implies on induced drag reduction.

The concept of a morphing winglet can have great impact on aircraft performance, significantly reducing drag and emissions. Also, winglets are smaller than other structures and will not cause a critical failure if the morphing system is not working properly. This makes the morphing winglet a cheaper and more secure technology, increasing the chance

of application on the industry. These factors make morphing winglets an attractive research topic.

This research presents an applicability study of the camber morphing winglet (CMW) on a midsize business jet using both numerical and experimental approach. The winglet geometry is optimized for different flight conditions using a genetic algorithm, varying its sections camber using the morphing device concept developed by Martins e Catalano (2003). Its performance is compared to a fixed geometry plane. The BLWF code (KARAS; KOVALEV, 2004) is used for the aerodynamic simulations and wind tunnel experiments are carried out to analyze the effects of the winglet on the wing performance.

Chapter 2 presents a literature review on the drag reduction technologies, winglet design and morphing structures to better understand the camber morphing winglet scenario. Chapter 3 presents the numerical optimization, presenting the performance model, genetic algorithm, aerodynamic simulation tool and discussing the results of the single point and full mission optimizations. Chapter 4 presents and discusses the wind tunnel experiments procedures and results. Chapter 5 draws the conclusions on the studied camber morphing winglet concept applicability.

## 2 LITERATURE REVIEW

The theoretical basis of this work is presented in this chapter. The literature review aimed to better understand the drag production and map the state of the art in winglet design and morphing structures. The Web of Science, Scopus and Google Scholar databases were used to look for literature on these topics

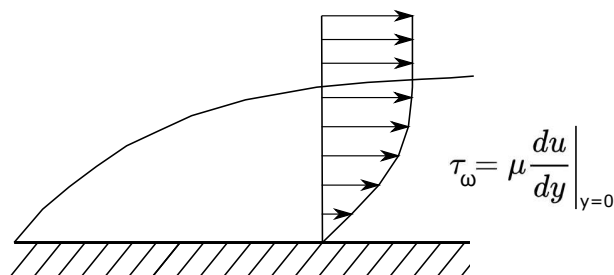
### 2.1 Drag breakdown

According to International Air Transport Association (2013), reaching the gas emission reduction on aviation goal in 2020 is only possible with the development of technologies for drag reduction. Understanding the drag production is the key to analyse in development technologies and their applicability. So, the first step was a review on drag breakdown.

The wing total drag may be divided in five components (ROSKAM; LAN, 2016):

- **Friction drag:** the friction drag caused by viscosity. Air velocity on the body surface is zero and increases through the boundary layer (BL). The velocity difference between the layers produces shear stress responsible for the friction drag. The friction drag is directly proportional to body surface area. Turbulent flow results on higher friction drag than laminar flow.

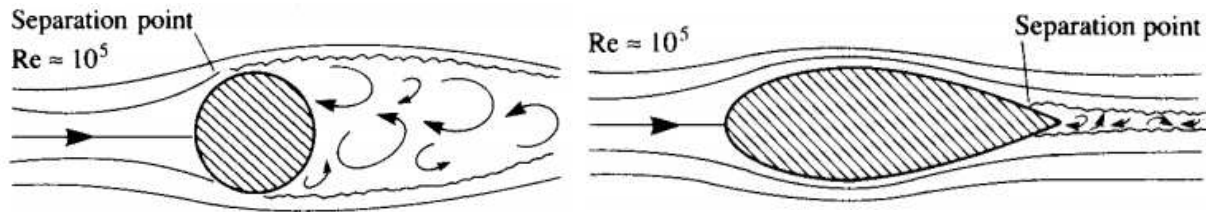
Figure 3: Boundary layer and viscous drag production



Source: The author

- **Pressure drag:** caused by the pressure distribution on the body. The pressure difference between forward and backward regions of the body generates the pressure drag. This drag component is strongly dependent on body shape and flow separations.

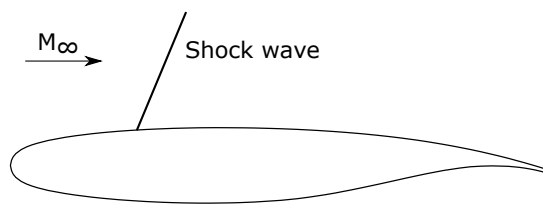
Figure 4: Cylinder and airfoil flow separation



Source: Anderson Jr. (2010)

- **Wave drag:** results from pressure differences through the shock wave. This drag component occurs when there are velocities higher than the sound speed on some regions of the body. Wave drag appears on transonic flight regimes and increases the higher the Mach number is.

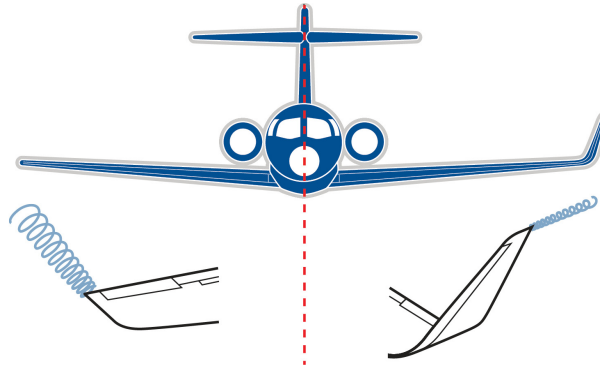
Figure 5: Airfoil shock wave



Source: The author

- **Induced drag:** caused by the flow from the pressure to suction sides on wing tip due pressure difference on the surfaces. This vortex flow induces angles on wing sections, reducing wing lift. The flow energy is dissipated on vortex rotating flow, resulting in lift-induced drag production. This component is dependent on body lift. The higher the lift, the higher is pressure difference and induced drag.

Figure 6: Wing tip vortex structure

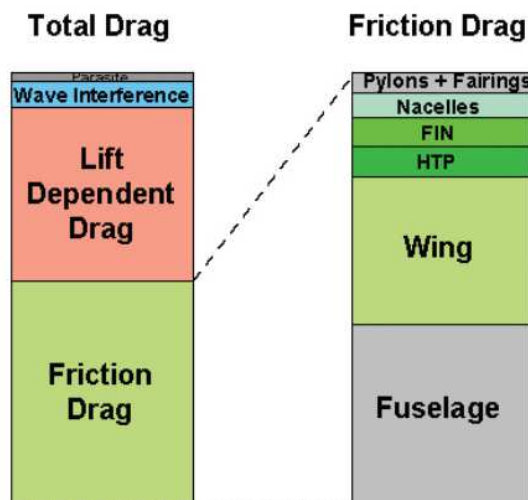


Source: <https://www.aopa.org/news-and-media/all-news/2017/may/flight-training-magazine/winglets> visited on 04 apr. 2019

- **Interference drag:** caused by the interaction of flow around two bodies placed side-by-side. The flow interaction causes changes on velocity profiles, pressure gradients and lift distribution on bodies, causing friction, pressure and induced drag.

Figure 7 shows typical drag breakdown for commercial transonic aircraft (SCHRAUF, 2005). Friction drag and lift dependent drag, or lift-induced drag, correspond to the great part of total drag. Investing on technologies capable of reducing these components is the key to reach the IATA carbon neutral growth goal by 2020.

Figure 7: Commercial transonic aircraft typical drag components



Source: Schrauf (2005)

## 2.2 Drag reduction technologies

### 2.2.1 Lift independent drag

Annex 1 of International Air Transport Association (2013) presents aerodynamic technologies capable of reducing drag and their relevance for achieving the fuel and emissions reduction goals. Passive and active technologies for friction drag reduction are presented, being the most relevant ones:

- **Laminar Flow Drag Coatings:** application of coating on surfaces that reduces or damps boundary layer disturbances, creating a surface that avoids laminar flow degradation. Reductions of 20% for wing skin friction drag were obtained using a compliant coating, reducing total drag by 5% (GAD-EL-HAK,2002).
- **Turbulent Flow Drag Coating:** application of coating on surfaces that reduces skin friction drag on turbulent boundary layer. Studies show that riblets can reduce drag by 10% (DUAN; CHOUDHARI, 2012)
- **Natural Laminar Flow:** consists of optimizing aircraft shape and surface for delaying laminar to turbulent boundary layer transition. This technology can be used to maintain laminar flow on aircraft nacelles, wing and tail, reducing skin friction drag (BRASLOW, 2011; Boeing Press Release, 2006; COLLIER, )
- **Hybrid Laminar Flow:** it has the purpose of maintaining laminar flow over most of the aircraft surfaces using surface suction or blowing, reducing fuel burn by 15% (BRASLOW, 2011). Flight tests results showed 10% drag reduction if Boeing 757 entire wing was modified. Airbus also showed potential of 10% fuel burn reduction on Airbus A320 using active flow control on wing, tail and nacelles (WALL, 2008; WALL; NORRIS, 2008).

Friction, pressure and wave drag are independent of the body lift coefficient ( $C_L$ ). The technologies cited so far on affect mainly friction drag. However, other technologies can reduce some of these other lift independent components. Transonic shock control can reduce wave drag by 50% without affecting friction drag by manipulating shock wave structure (BIRKEMEYER; ROSEMANN; STANEWSKY, 2000; OGAWA; BABINSKY, 2006).

Camber variable surfaces can be used both for high-lift devices and control surfaces continuous and seamless deflections. This technology can increase aircraft maximum lift to drag ratio ( $\frac{L}{D}$ ), adapting aircraft geometry to flight conditions and reducing total drag. Carter et al. (2007) presented work using a mission adaptive compliant wing. Application of compliant adaptive wing was able to improve  $\frac{L}{D}$  by 3.3%, saving 15% on fuel costs for a B737 or A320 sized aircraft (HETRICK et al., 2007).

### 2.2.2 Lift induced drag

Some technologies were developed for reducing lift-induced drag. Lift-induced drag ( $C_{D_i}$ ) can be approximated as Eq. 2.1, being proportional to the lift coefficient ( $C_L$ ), wing aspect ratio ( $AR$ ) and Oswald's span efficiency factor ( $e$ ).

$$C_{D_i} = \frac{C_L^2}{\pi AR e} \quad (2.1)$$

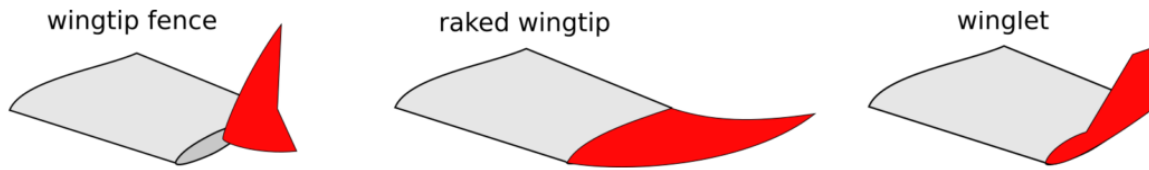
The definition of aspect ratio is  $AR = \frac{b^2}{S_w}$ , where  $b$  is the wing span and  $S_w$  is the wing area. From that definition and Eq. 2.1, it is possible to note that increasing wing span, maintaining its area, reduces induced drag. This way, technologies that enable greater wing span can be used for induced drag reduction, as the Boeing's 777-X folding wing tip (FIELD, 2018). Truss and strut-braced wing concept have been studied as a possibility to increase wing span and reduce weight without compromising its structural integrity. Gern et al. (2005) study showed a reduction of nearly 20% take-off gross weight and 29% on fuel burn, compared to a technologically similar cantilever-wing configuration.

Another alternative for lift-induced drag reduction is wing tip devices capable of moving the vortex far away from the wing or reduce its strength and size. Coimbra (1997) and Annex 1 of International Air Transport Association (2013) listed wing tip devices used for induced drag reduction and their effects. The wing tip devices currently in use on modern aircraft are:

- **Wing fence:** swept vertical surfaces extending above and below wing level used to move and reduce the tip vortex size (MANN; ELSHOLZ, 2005).
- **Raked wing tip:** a planar wing tip with a high degree of swept angle. The raked wing tip reduces the tip vortex strength by reducing wing tip chord and increasing the wing span (HALPERT et al., 2010).
- **Winglet:** near-vertical lift extensions of the wingtip. The winglet reduces the wing tip vortex size and strength, reducing the induced drag. It also uses the vortex flow to generate thrust.

Figure 8 shows examples of listed wing tip devices. These devices are capable of reducing wing induced drag and fuel burn by 5%. However, wing tip devices increase aircraft wetted area, increasing skin friction drag, and wing tip load, causing alteration on wing root bending moment. Increase on wing bending moment can increase wing weight due to additional structures for resisting this load. In order to solve this dilemma, a discussion on the winglet design is presented in the next section, explaining its working principle and presenting a chronological review about its impact on aircraft performance.

Figure 8: Wing tip devices currently in use on modern aircraft.

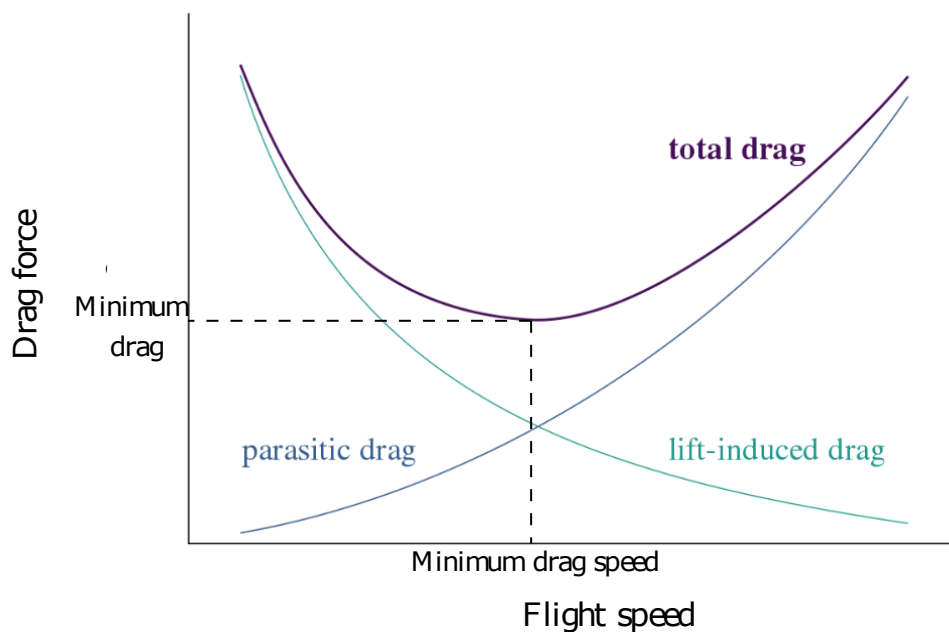


Source: Razvan Apetrei (2017)

### 2.3 Winglet design

Winglets are wing tip devices capable of producing thrust from the tip flow and reducing the vortex size and strength (KROO, 2001), reducing wing induced drag component. On the other hand, the additional area causes friction drag increase and interference drag generation at the wing-winglet union. The winglet must be optimized to minimize the total drag, making a trade-off between the induced drag reduction and parasite drag increase on a certain condition (Figure 9).

Figure 9: Winglet drag trade off



Source: The author

Analysing winglet design structural aspects, winglet installation causes wing tip loading increase due winglet produced forces. This causes a flexo-compression increase on wing root, implying on heavier wing structure to resist the load. Both winglet aerodynamic and wing weight effects should be considered on design process.

Whitcomb (1976) developed a theoretical methodology for winglet design and tested a model of a commercial jet model with no wing tip, span extension and winglet. Span extension and winglet produced the same wing root bending moment, implying same design weight penalty. Experimental results showed that winglet usage reduced induced drag by 20% and increased lift to drag ratio ( $\frac{C_L}{C_D}$ ) by 9% at design Mach number ( $M$ ) and  $C_L$ , compared to no tip wing. Winglet increase on  $\frac{C_L}{C_D}$  was more than double of the ones obtained with span extension. Heyson, Riebe e Fulton (1977) confirmed recommendations presented by Whitcomb (1976) by simulating winglets using different wing geometries and comparing them to extended span wings with same root bending moment. They concluded that winglets present higher effect on induced drag than extensions for a constant bending moment.

Further investigation on winglet and span extension trade-off was presented by Jones e Laslinski (1980). They used the integrated bending moment along wing span and ideal wing structure as constrain for concept comparison. The computational study showed that both winglets and span extensions achieve same induced drag reduction for same ideal wing weight.

Following winglet design discussion, Jupp (2001) presented a study on wing weight, induced and parasite drag trade-off for wings and wing tip devices geometries. It showed how complex wing and devices geometry optimization process can be, being a multidisciplinary approach needed to find the best design.

Numerical methods are used to design and optimize winglet geometry for different flight conditions. Drag reduction of 4.9% for take-off and landing configurations and 1.6% for cruise condition were achieved by changing wing tip dihedral and swept angles, using computational fluid dynamics tools to estimate an equivalent drag variation defined considering aerodynamic effects and root bending moment influence on drag (BUSCHER; RADESPIEL; STREIT, 2006).

An exploration of aerodynamic and structural effects of winglets was performed by Takenaka et al. (2008), using a genetic algorithm to optimize winglet geometry for a commercial jet aircraft. Minimal block fuel and maximum take-off weight (MTOW) were defined as design objectives, resulting in an optimum geometry that increased the MTOW by around 0.6% and reduced block fuel by almost 5%. A pareto analysis gave insight on the relations between winglet geometry parameters, drag components and structural loads. A specific investigation on winglet cant angle effect was presented by Khalil et al. (2016), showing  $\frac{C_L}{C_D}$  increase of 11% for best cant angle winglet with respect to wing with no tip device.

Wing extension and winglets were again compared on the study by Ning e Kroo (2010). A multidisciplinary analysis about ideal structural weight, viscous and induced drag was performed by optimizing wing and winglet torsion angles. Discrete vortex Weissinger

model (WEISSINGER, 1947) was used to predict the wing sections angles of attack ( $\alpha_{section}$ ) and viscous drag, assuming a section drag parabolic variation with section lift. Induced drag component was calculated at Trefftz plane by using a drag-free wake leaving wing planform trailing edge. Tip extensions showed better performance for  $\frac{C_{L_{maneuver}}}{C_{L_{cruise}}} = 1$ , while winglets showed better results for  $\frac{C_{L_{maneuver}}}{C_{L_{cruise}}} = 2.5$ .

An experimental work using aerodynamic balance, surface pressure distribution and wake surveys with a multi-hole Pitot probe tested wing tip blowing, fixed and adaptive multi-winglets concepts (CÉRON-MUÑOZ et al., 2013). Multi-winglets showed wing effective aspect ratio ( $AR_{eff}$ ) increase of 55% and maximum range and rate of climb were increased by 7% and 12%, respectively. Wing-tip blowing increased wing maximum efficiency, however, showed not feasible for commercial application due to its large energy requirements. This makes winglets a better option for performance improvement.

As shown so far, winglets have an impact on aircraft aerodynamic efficiency, fuel burn and weight. Doing so, winglets installation on existing aircraft affect its direct operating costs (DOC). Reduction 2% on DOC was achieved with winglet installation for a long-range passenger aircraft, however, DOC reduction due to improved aerodynamics was compensated by DOC penalty due weight increase for a regional passenger aircraft scenario (ELHAM; TOOREN, 2014).

Winglets also are used for improving Un-manned-Aerial-Vehicle (UAV) performance. Best winglet configuration increased a Medium-Altitude-Long-Endurance Un-manned-Aerial-Vehicle flight time by 10%.

The literature review brings some important characteristics of winglet design, a multidisciplinary process that must analyse concepts compliance with project requirements. The results show winglet high potential on improving aircraft performance at different flight conditions, considering different constraints for each one of them. However, the final design consists of a unique fixed geometry that will not present optimum performance for the whole flight envelope, but optimum design for all flight conditions sum. This limitation can be overcome by using components capable of adjusting their shape on flight. The so-called morphing structures enable aircraft to adjust its geometry for optimum performance at each flight conditions, resulting in a final configuration that sums all optimum designs. Winglet performance characteristics suggest that combining winglet technology with morphing structures technologies may enable even greater aircraft performance.

Based on this idea, a literature review on morphing structures is presented in the next section in order to understand its capabilities, benefits and downsides.

## 2.4 Morphing aircraft

Morphing structures are components capable of adjusting their shape to aircraft flight condition. Different aircraft components may use the morphing technology for control, load alleviation or performance improvement. Plenty of studies on this topic are available on literature and are listed on the review made by Barbarino et al. (2011).

Studies on morphing wings capable of changing its platform shape are found, most of them performed for unmanned air vehicle (UAV) wings. Blondeau, Richeson e Pines (2003) tested a three section inflatable telescopic UAV wing capable of increasing its aspect ratio by 114%. However, wind tunnel experiments showed an increase on parasitic drag due to wing sections seams, reducing its lift to drag ratio ( $\frac{L}{D}$ ) by 25% smaller than its fixed wing counterpart compared to a rigid wing with same platform geometry. Further studies on this concept showed aspect ratio increase of 250% achieving the same  $\frac{L}{D}$  of fixed geometry wing (SAMUEL; PINES, 2007). An electromechanical system to change a UAV wing span, chord, sweep and twist angle on a wind tunnel test, showing potential on achieving a minimal drag condition for a  $C_L$  range (NEAL et al., 2004; NEAL; FARMER; INMAN, 2006).

Computational studies were also performed on UAV wing platform morphing system, optimizing span and section camber. Aerodynamic and structural analysis showed that this concept was able to reduced drag by up to 30% in different flight stages, representing performance improvements in off-design conditions Gamboa et al. (2009). Also, maximum speed was increased while takeoff distance was reduced. It was noted that flexible skin deformation may spoil morphing aerodynamics benefits, being an important issue on morphing wing development.

A variable stiffness spar (VSS) concept capable of changing wing twist for enhanced roll control was developed by Chen et al. (2000). Computational results showed that this concept was able to improve roll performance of an advanced fighter at subsonic and transonic flight conditions, increasing roll rate by up to 22%. Experimental analysis of the VSS concept was performed by Florance et al. (2004).

Wing geometry variable according to external aerodynamic loads may be optimized, increasing aerodynamic performance on cruise (SZODRUCH, 1985; SMITH; NELSON, 1990; SICLARI; NOSTRAND; AUSTIN, 1996; MARTINS; CATALANO, 2003) and maneuver (THORNTON, 1993). A 24.6% increase in aircraft range was obtained with camber morphing wing concept by (MARTINS; CATALANO, 2003). Performance improvement due to camber morphing wing concept proposed by Martins e Catalano (2003) was confirmed by experimental results obtained by Cosin et al. (2010), that used a genetic algorithm (GA) for optimizing wing sections camber with wind tunnel on loop.

Great performance improvement is obtained using morphing wing concepts. How-

ever, safety is an important issue for these devices. Wing morphing system failures would be critical, possibly compromising flight safety. This makes certification of such devices really difficult. Yet, morphing structures concept can be applied to other aircraft components that do not compromise flight in case of failure.

Wing tip devices have great potential for morphing applications, once they can greatly improve aircraft performance by changing their shape without affecting flight safety. A variable cant angle winglet was tested as an auxiliary control surface (BOURDIN; GATTO; FRISWELL, 2008). Computational and experimental results showed that this winglet concept can be used for control on certain conditions, but can not ensure substitute all conventional control surfaces for a full control envelop.

Performance increase using variable geometry wing tip devices were also analysed. A multidisciplinary optimization (MDO), using a genetic algorithm, of morphing winglet (MORPHLET project) concept capable of changing section dihedral showed increase of 3.5 to 5.2% on specific air range (URSACHE et al., 2007). Further investigations on the MORPHLET project confirmed the calculated specific air range increase and 3.1% improvement on  $\frac{C_L}{C_D}$  at climb (SMITH et al., 2012). It determined take-off and landing maximum lift increase of 13.8%, reducing the take-off and landing distances by 7% and 7.8%, respectively. Study of a morphing winglet concept based on unsymmetrical stiffness by citeonlinewang2016morphingwinglet presented  $\frac{C_L}{C_D}$  increase of 5% with a weight increase of 3.5%, showing both positive and negative effects of this technology.

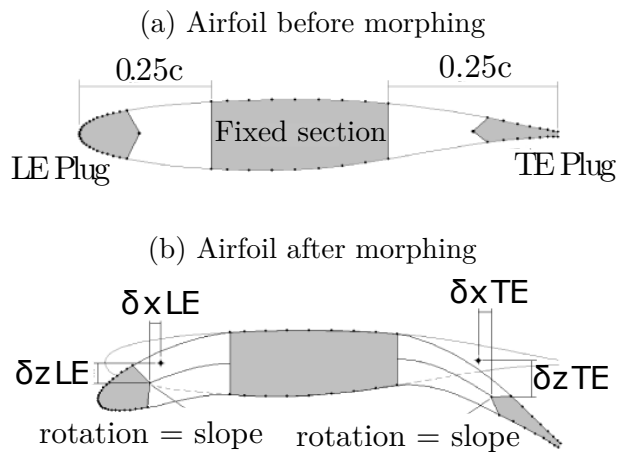
Great possibilities for performance improvement are expected from applying morphing technologies on wing tip devices. However, no investigation on application of a camber morphing winglet was found on literature. In this context, the camber morphing winglet investigation contributes for further advance on morphing aircraft and performance improvement.

### 3 CAMBER MORPHING WINGLET NUMERICAL EVALUATION

#### 3.1 Camber morphing concept

The morphing concept developed by Martins e Catalano (2003) enables camber changes on airfoil section by moving both the leading and trailing edges (Fig. 10). The wing central section ( $0.25 < \frac{x}{c} < 0.75$ ) is held fixed in order to preserve the wing structural box integrity. Leading and trailing edges plugs are used to ensure feasible geometries, avoiding geometries with no physical or aerodynamic meaning. These characteristics make this system an attractive option for the camber morphing winglet application, attending the highlighted safety and feasibility goals for the device.

Figure 10: Morphing system representation



Source: Martins e Catalano (2003)

Two parameters defined the morphed section geometry, setting the leading ( $P_{le}$ ) and trailing ( $P_{te}$ ) edge deflections. The parameters were limited on interval that produced feasible geometries, as:

$$-2.45 \leq P_{le} \leq 1.3 \quad (3.1)$$

$$-0.1 \leq P_{te} \leq 0.05 \quad (3.2)$$

Based on these parameters, the camber line equation is calculated using Eq. 3.3 to 3.7. The airfoil surface and camber line are interpolated using cubic splines to ensure their

smoothness. The presented camber morphing system was used for studying the camber morphing winglet application.

$$\frac{y}{c_c} = \begin{cases} 0.5 \left( \frac{y}{c_u} + \frac{y}{c_l} \right) + \frac{P_{te}}{\left( \frac{y}{c_{l_{0.25c}}} - 2 \right)^2} \left( \frac{y}{c_l} - \frac{y}{c_{l_{0.25c}}} \right)^2 & 0 \leq \frac{y}{c_u} < 0.25 \\ 0.5 \left( \frac{y}{c_u} + \frac{y}{c_l} \right) & 0.25 \leq \frac{y}{c_u} \leq 0.75 \\ 0.5 \left( \frac{y}{c_u} + \frac{y}{c_l} \right) + \frac{P_{te}}{\left( 1 - \frac{y}{c_{l_{0.75c}}} \right)^3} \left( \frac{y}{c_l} - \frac{y}{c_{l_{0.75c}}} \right)^3 & 0.75 < \frac{y}{c_u} \leq 1 \end{cases} \quad (3.3)$$

$$\tan(\alpha_u) = \begin{cases} 2 \left( \frac{P_{te}}{\left( \frac{y}{c_{u_{0.25c}}} - 2 \right)^3} \right) \left( \frac{y}{c_u} - \frac{y}{c_{u_{0.25c}}} \right) & 0 \leq \frac{y}{c_u} < 0.25 \\ 0 & 0.25 \leq \frac{y}{c_u} \leq 0.75 \\ 3 \left( \frac{P_{te}}{\left( 1 - \frac{y}{c_{u_{0.75c}}} \right)^3} \right) \left( \frac{y}{c_u} - \frac{y}{c_{u_{0.75c}}} \right) & 0.75 < \frac{y}{c_u} \leq 1 \end{cases} \quad (3.4)$$

$$\tan(\alpha_l) = \begin{cases} 3 \left( \frac{P_{te}}{\left( 1 - \frac{y}{c_{l_{0.75c}}} \right)^3} \right) \left( \frac{y}{c_l} - \frac{y}{c_{l_{0.25c}}} \right)^2 & 0 \leq \frac{y}{c_l} < 0.25 \\ 0 & 0.25 \leq \frac{y}{c_l} \leq 0.75 \\ 3 \left( \frac{P_{te}}{\left( 1 - \frac{y}{c_{l_{0.75c}}} \right)^3} \right) \left( \frac{y}{c_l} - \frac{y}{c_{l_{0.75c}}} \right)^2 & 0.75 < \frac{y}{c_l} \leq 1 \end{cases} \quad (3.5)$$

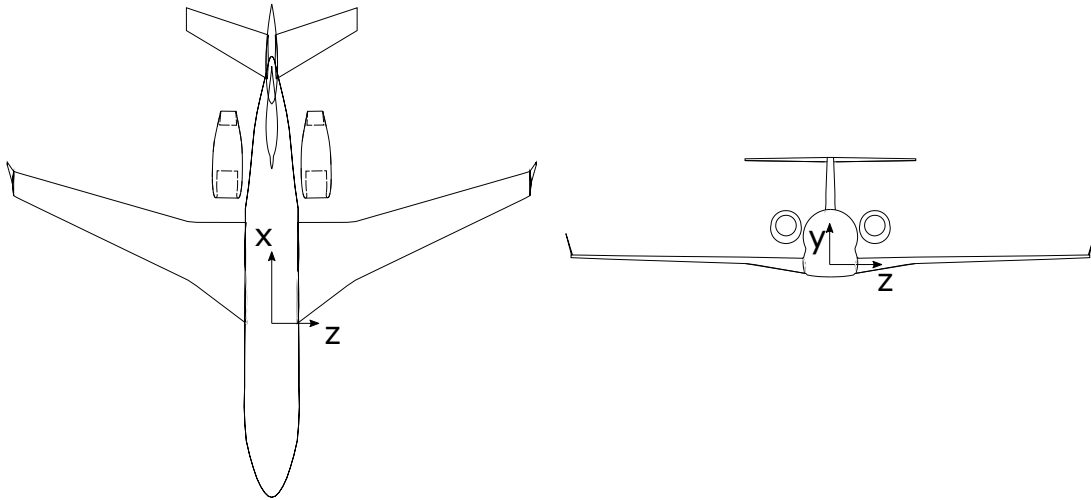
$$\frac{x}{c_{morphed}} = \begin{cases} \frac{x}{c_u} - \sin(\alpha_l) \left| \frac{y}{c_u} - 0.5 \left( \frac{y}{c_u} + \frac{y}{c_l} \right) \right| & \text{Upper side} \\ \frac{x}{c_l} + \sin(\alpha_2) \left| \frac{y}{c_u} - 0.5 \left( \frac{y}{c_u} + \frac{y}{c_l} \right) \right| & \text{Lower side} \end{cases} \quad (3.6)$$

$$\frac{y}{c_{morphed}} = \begin{cases} \frac{y}{c_c} + \cos(\alpha_l) \left| \frac{y}{c_u} - 0.5 \left( \frac{y}{c_u} + \frac{y}{c_l} \right) \right| & \text{Upper side} \\ \frac{y}{c_c} - \cos(\alpha_2) \left| \frac{y}{c_u} - 0.5 \left( \frac{y}{c_u} + \frac{y}{c_l} \right) \right| & \text{Lower side} \end{cases} \quad (3.7)$$

### 3.2 Aircraft geometry

In order to demonstrate the camber morphing winglet technology benefits, a midsize business jet was selected as reference aircraft (Fig. 11). Typical business jets have a low wing configuration, T-tail and nacelle installed on fuselage. Winglets are widely used on these jets, both for performance and aesthetic reasons.

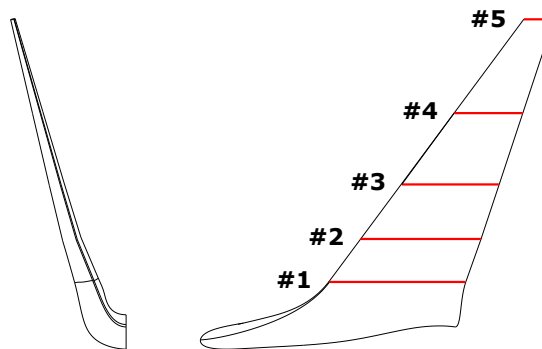
Figure 11: Generic midsize business jet geometry



Source: The author

Figure 12 shows the winglet close up, detailing the variable camber sections position. The same airfoil (Fig. 13) was used on the five sections, being the camber variation the only difference between them. The surfaces between the camber variable sections are interpolated using the BLWF code geometry construction function.

Figure 12: Winglet geometry and camber adaptable sections



Source: The author

Figure 13: Airfoil used on the winglet sections for the morphing optimization



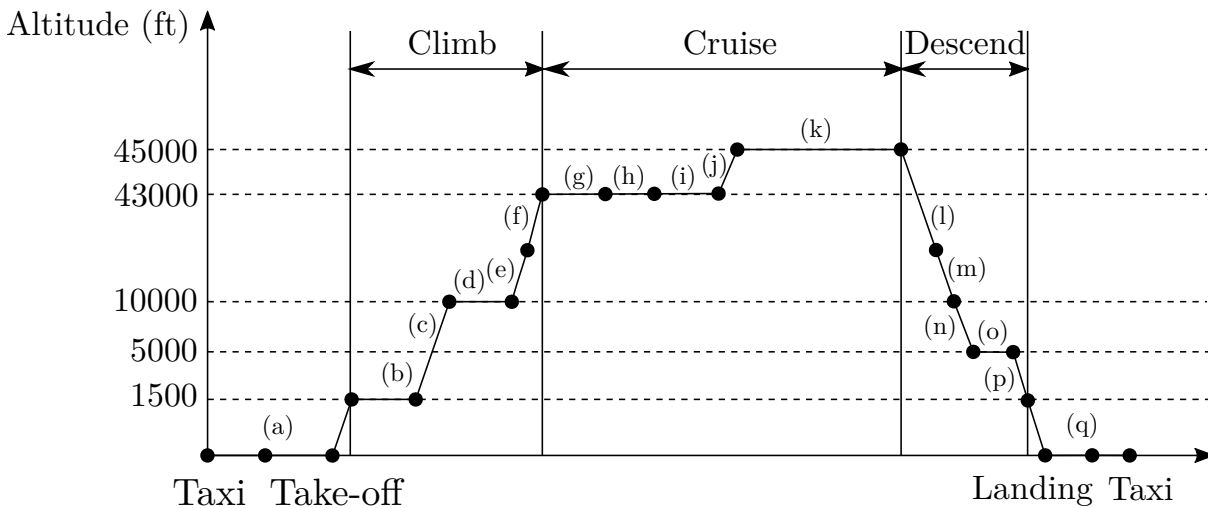
Source: The author

### 3.3 Aircraft performance model

A performance model was used to simulated aircraft flight on a typical mission and the camber morphing winglet fuel consumption improvements evaluation. The aircraft typical mission was defined based on the instrument flight rules (IFR) which includes takeoff, climb, cruise, descent and landing phases (Fig. 14) having fuel enough for flying to an alternative airport 200 NM away and 30 minute loiter after arriving at the destination from the Federal Aviation Administration (1978, 1997).

Embraer's Legacy 500 was selected as benchmark for the simulation airspeeds for each phase (AGÊNCIA NACIONAL DE AVIAÇÃO CIVIL, 2014), aircraft weights, range, engine parameters and mission fuel consumption (BUSINESS & COMMERCIAL AVIATION, 2015). These values were used for performance model calibration.

Figure 14: Mission profile



Source: The author

- (a) Engine start, warm up, taxi, take-off and climb to 1500 ft . It is considered a weight at the end of this phase as  $W_{to} = 0.98TOW$  (ROSKAM, 2015)
- (b) Acceleration from  $Mach = 0.3$  to  $IAS = 154 \frac{m}{s}$  at  $h = 1500ft$
- (c) Climb at constant  $IAS = 154 \frac{m}{s}$  from 1500 ft to 10000 ft
- (d) Acceleration from  $IAS = 154 \frac{m}{s}$  to  $IAS = 165 \frac{m}{s}$  at  $h = 10000ft$ .
- (e) Climb at constant  $IAS = 165 \frac{m}{s}$  from 10000 ft until  $Mach = 0.8$
- (f) Climb at constant  $Mach = 0.8$  to  $h = 43000ft$
- (g) Cruise at  $Mach = 0.8$  and  $h = 43000ft$

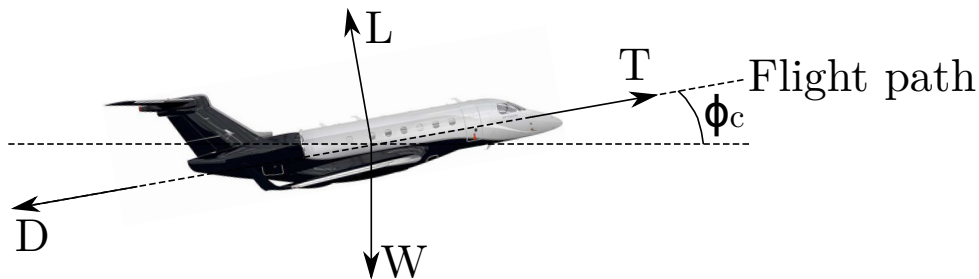
- (h) Acceleration from  $Mach = 0.8$  to  $Mach = 0.8124$  at  $h = 43000ft$
- (i) Cruise at  $Mach = 0.8124$  and  $h = 43000ft$
- (j) Climb from  $h = 43000ft$  to  $h = 45000ft$  at  $M = 0.8124$
- (k) Cruise at  $Mach = 0.8124$  and  $h = 45000ft$
- (l) Descent from  $h = 45000ft$  at constant  $M = 0.8$  until  $IAS = 165\frac{m}{s}$
- (m) Descent to  $h = 10000ft$  at constant  $IAS = 165\frac{m}{s}$
- (n) Descent to  $h = 5000ft$  at constant  $IAS = 154\frac{m}{s}$
- (o) Loiter at  $h = 5000ft$  for  $t_{loit} = 30min$
- (p) Descent from  $h = 5000ft$  to  $h = 1500ft$  at constant  $IAS = 154\frac{m}{s}$
- (q) Landing from 1500 ft, taxi and engine shut down. It is considered a weight at the end of the taxi as  $W_{ld} = 0.992W_i$  (ROSKAM, 2015)

Roskam e Lan (2016) presented a methodology to represent the aircraft dynamics during flight, allowing the calculation of the velocity, altitude and weight variations throughout the mission. The mission was divided into time steps during which the forces acting on the aircraft are considered constant. Sections 3.3.1 to 3.3.3 describe each flight phase and show their dynamics equations.

### 3.3.1 Climb equations

The forces acting on the airplane during climb are shown on Figure 15. Roskam e Lan (2016) defines, assuming constant small climbing angles ( $\phi_c < 15^\circ$ ) and considering engine thrust aligned with flight path ( $\phi_t = 0$ ), the climb dynamics equations as:

Figure 15: Forces acting on plane during climb



Source: The author

- Normal to the flight path

$$L = W \quad (3.8)$$

- Along the flight path

$$T - D - \frac{W}{g} \frac{dV}{dt} = W \sin \phi_c \quad (3.9)$$

Since we have that the rate of climb (*RoC*) is:

$$RoC = \frac{dh}{dt} = V \sin \phi_c \quad (3.10)$$

It can be deduced from Equations 3.8 to 3.10 that:

$$RoC = \frac{(T-D)V}{1 + \frac{V}{g} \frac{dV}{dh}} \quad (3.11)$$

$\frac{dV}{dh}$  is calculated based on climb condition:

- For constant IAS climb

$$\frac{dV}{dh} = 0.567M^2 \quad (3.12)$$

- For constant Mach climb

$$\frac{dV}{dh} = -0.133M^2 \quad (3.13)$$

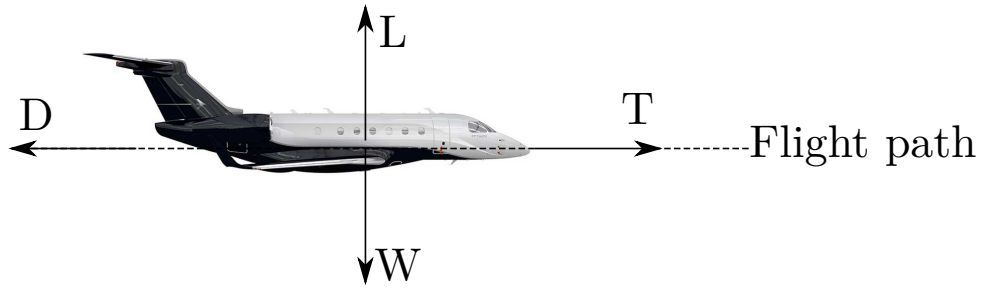
Business jets need to climb to cruise flight level as fast as possible in order to minimize flight time and fuel consumption. This way, the optimization has the objective is set to maximize the rate of climb *RoC*. Equation 3.11 shows that *RoC* is proportional to thrust (*T*) and lift to drag ratio ( $\frac{L}{D}$ ), being maximum *RoC* obtained by maximizing these two parameters. The engine maximum continuous thrust ( $T = T_{maxcont} = 0.625T_{maxav}$ ) is used during all the climb, in order to maximize the *RoC*. The maximum continuous thrust depends only on the flight height (Section 3.3.5), being independent of geometries variations due to the morphing winglet. This way, the optimization algorithm will look for a maximum  $\frac{L}{D}$  configuration, maximizing the genetic algorithm objective function (Eq. 3.14), resulting on maximum *RoC*, minimum fuel consumption and time to climb.

$$F_{climb} = 10 \frac{C_L}{C_D} \quad (3.14)$$

### 3.3.2 Cruise equations

The forces acting on the aircraft on constant Mach number and altitude cruise are shown on Figure 16. The dynamics equations for are:

Figure 16: Forces acting on plane during cruise



Source: The author

- Normal to the flight path

$$L = W \quad (3.15)$$

- Along the flight path

$$T = D \quad (3.16)$$

From the engine model shown on Section 3.3.5, weight variation is determined by:

$$dW = -TSFC \times T \times dt \quad (3.17)$$

From Equations 3.15 to 3.17 we have that:

$$T = D = W \frac{C_L}{C_D} \quad (3.18)$$

$$R = -\frac{VC_L}{TSFCC_D} \int_{W_{initial}}^{W_{final}} \frac{dW}{W} = \frac{V}{TSFC} \frac{C_L}{C_D} \ln \frac{W_{initial}}{W_{final}} \quad (3.19)$$

So, the maximum range is obtained by maximizing  $V \frac{C_L}{C_D}$ . The cruise speed must avoid to exceed the drag-divergence Mach when maximizing  $V \frac{C_L}{C_D}$ . The air speed can be related to the Mach number using the relation:

$$V = M \sqrt{\frac{\tau}{\tau_0}} a_0 \quad (3.20)$$

Substituting the velocity relation from Equation 3.20 at Equation 3.19 results:

$$R = \frac{a_0 \sqrt{\frac{\tau}{\tau_0}}}{TSFC} M \frac{C_L}{C_D} \ln \frac{W_{initial}}{W_{final}} \quad (3.21)$$

For a fixed range, final weight can be calculated using Eq. 3.21 as:

$$R = \frac{a_0 \sqrt{\frac{\tau}{\tau_0}} M \frac{C_L}{C_D} \ln \frac{W_{initial}}{W_{final}}}{TSFC} \Rightarrow W_{final} = W_{initial} - \frac{R \times TSFC}{a_0 \sqrt{\frac{\tau}{\tau_0}} M \frac{C_L}{C_D}} \quad (3.22)$$

From Eq. 3.22, the minimum fuel consumption is obtained by increasing  $M \frac{C_L}{C_D}$  or reducing the  $TSFC$ . The  $TSFC$  depends on the engine efficiency only and is not affected by the camber morphing winglet geometries changes. Also, the mission profile defines a constant height and Mach number cruise ( $M = cte$ ). This way,  $\frac{C_L}{C_D}$  must be reduced in order to reduce aircraft fuel consumption on cruise. So, the objective function is:

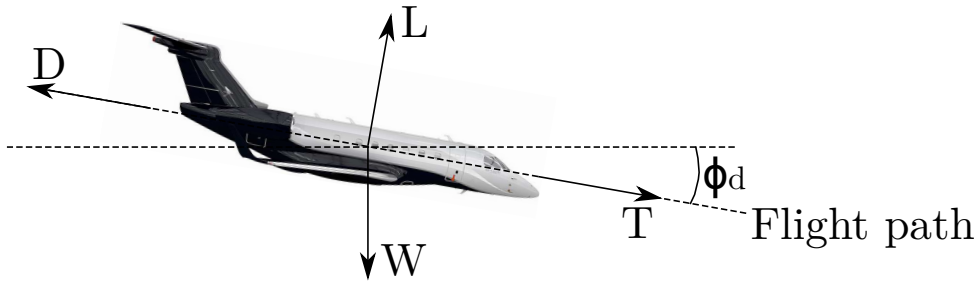
$$F_{cruise} = 10 \frac{C_L}{C_D} \quad (3.23)$$

The optimization maximizes the objective function, finding the winglet geometry that minimizes fuel consumption on cruise.

### 3.3.3 Descent equations

Forces acting on the airplane on descent are shown on Figure 17. The rate of descent ( $RoD$ ) is similar to the  $RoC$  equation, being calculated as:

Figure 17: Forces acting on plane during descent



Source: The author

$$RoD = \frac{(T-D)V}{1 + \frac{W}{g} \frac{dV}{dh}} \quad (3.24)$$

The  $\frac{dV}{dh}$  is calculated using Equations 3.12 and 3.13, according to descent condition. Similarly to climb, the objective is to minimize time of descent, flight time and aircraft fuel consumption on descent. Equation 3.24 shows that  $RoD$  is proportional to thrust ( $T$ ) and lift to drag ratio ( $\frac{L}{D}$ ), being maximum  $RoD$  obtained by maximizing these two parameters.

Once the aircraft thrust ( $T$ ) is fixed at a minimal ( $T_{idle} = 0.06T_{max_{av}}$ ), the maximum  $RoD$  is obtained by maximizing  $\frac{L}{D}$ . This way, the optimization objective function for descent is:

$$F_{descent} = 10 \frac{C_L}{C_D} \quad (3.25)$$

### 3.3.4 Loiter equations

Loiter is defined as constant speed and height flight condition, being the dynamics equations similar to cruise equations. This way, objective function for loiter defined as:

$$F_{loiter} = 10 \frac{C_L}{C_D} \quad (3.26)$$

### 3.3.5 Engine model

The engine thrust and fuel consumption is modelled based on the Legacy 500 propulsion system and fuel consumption information (BUSINESS & COMMERCIAL AVIATION, 2015). The variation on maximum thrust ( $T_{max_{av}}$ ) and thrust specific fuel consumption ( $TSFC$ ) with altitude and speed are based on engine models presented by Eshelby (2000), Mair e Birdsall (1996) and Ojha (1995). The used equations are:

$$T_{max_{av}} = T_{max} \left( \frac{\rho}{\rho_0} \right)^{0.7} \quad (3.27)$$

$$TSFC = TSFC_0 \sqrt{\frac{T}{T_0}} M^{0.48} \quad (3.28)$$

Aircraft weight variation during flight is calculates using Equation 3.29, where  $dt$  is the time step used on simulation.

$$\Delta W = -TSFC \times T \times dt \quad (3.29)$$

Engine parameters  $T_{max}$ ,  $TSFC_0$ ,  $T_{max_{cont}}$  and  $T_{idle}$  were determined by simulating two missions, using ranges, BOW, payload and fuel weights of a Legacy 500 (BUSINESS & COMMERCIAL AVIATION, 2015). The model values are adjusted to match Legacy 500 fuel consumption, climb and cruise durations, resulting on the parameters shown on Table 2.

Table 2: Engine performance parameters

$T_{max}$ [N]	$T_{max_{cont}}$ [-]	$T_{idle}$ [-]	$TSFC_0$ [ $\frac{kg}{Ns}$ ]
62600	$0.625T_{max_{av}}$	$0.06T_{max_{av}}$	$1.859 \times 10^{-5}$

Source: The author

Simulation fuel consumption error was smaller than 0.5% compared to aircraft fuel consumption listed on Business & Commercial Aviation (2015) and shown on Table 3.

Table 3: Engine model validation

Range [NM]	Fuel consumption [kg]	Simulation fuel consumption [kg]	Error [%]
3125	5103	5127	0.3
1000	1701	1680	0.5

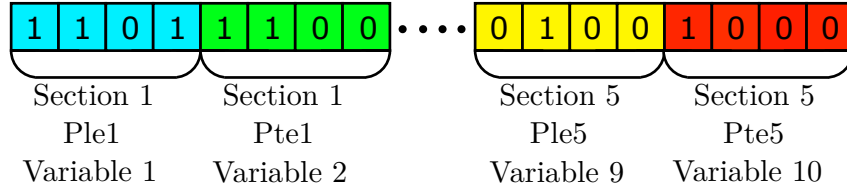
Source: Business & Commercial Aviation (2015)

### 3.4 Optimization algorithm

The camber morphing winglet optimization problem consists of a non-linear objective function problem of unknown shape with multiple variables. This way, gradient-based algorithms are not suitable for this application. The genetic algorithm (GA) is a gradient independent evolutionary optimization method based on the natural selection process. It is useful for multidisciplinary problems with unknown non-linear objective functions, being already used on wing geometry optimizations problems (CAYIROGLU; KILIC, 2017; COSIN et al., 2010; OYAMA et al., 1997). Good results were found using GA for aerodynamics optimization problem. This makes the GA an attractive optimization algorithm for the camber morphing winglet optimization problem.

The GA is a stochastic optimization method that starts from a random initial population and by means of algorithm operators, which mimics the natural evolution process, moves towards the optimum solution. The population is composed of individuals represented by binary chromosomes. Each gen in the chromosome is a four-digit binary number that defines a variable that defines the leading ( $P_{le}$ ) and trailing ( $P_{te}$ ) edge parameters of the five winglet camber variable sections (Fig. 18).

Figure 18: Gen representation on the winglet optimization



Source: The author

The  $P_{le}$  and  $P_{te}$  are calculated as function of the variables ( $Var_i$ ):

$$P_{le_i} = 0.25Var_i - 2.45 \quad i = 2, 4, 6, 8, 10 \quad (3.30)$$

$$P_{te_i} = 0.01Var_i - 0.1 \quad i = 1, 3, 5, 7, 9 \quad (3.31)$$

This results on a chromosome 40 bits long composed by 10 variables. The  $P_{le}$  and  $P_{te}$  parameters are defined on the intervals showed on Eq. 3.1 and 3.2, with variations of  $\Delta P_{le} = 0.25$  and  $\Delta P_{te} = 0.01$ . The variations on the section camber as function of  $P_{le}$  and  $P_{te}$  are shown on Eq. 3.3 to 3.7. In order to guarantee that only feasible geometries are generated, a constraint on both leading and trailing angles of all sections was set. The limitations defined that the angles of a section can only be equal or bigger than the angles of the previous section, avoiding alternating camber direction changes from winglet root to tip. These constrain is defined on  $P_{le}$  and  $P_{te}$  parameters as:

$$P_{le_i} = \max(0.25Var_i - 2.45, P_{le_{i-2}}) \quad i = 4, 6, 8, 10 \quad (3.32)$$

$$P_{te_i} = \max(0.01Var_i - 0.1, P_{te_{i-2}}) \quad i = 3, 5, 7, 9 \quad (3.33)$$

The population individual's chromosomes define winglet geometries that differ sections camber only. Each individual fitness is calculated using the aerodynamic coefficients obtained from BLWF simulation (Section 3.5) and the objective functions defined on Eq. 3.14 to 3.26. Goldberg (1989) recommends a fitness scaling before the individual's selection process for reproduction is done. Fitness scaling avoids population dominance by exceptional individuals on first generations, which would cause premature convergence. Fitness scaling is defined in Eq. 3.34. The parameters  $k_1$  and  $k_2$  are calculated from the Eq. 3.35 and 3.37.

$$F' = k_1F + k_2 \quad (3.34)$$

$$k_1 = \frac{F_{mean}}{(F_{max} - F_{mean})} \quad (3.35)$$

$$k_2 = (2 - k_1) F_{mean} \quad (3.36)$$

No individual may have  $F' \leq 0$ , so if  $F'_{min} = k_1 F_{min} + k_2 \leq 0$  then the scaling parameters  $k_1$  and  $k_2$  are recalculated using Eq. 3.36 and 3.38. Finally the individual selection probability is defined by Eq. 3.39.

$$k_1 = \frac{F_{mean}}{(F_{mean} - F_{min})} \quad (3.37)$$

$$k_2 = -k_1 F_{min} \quad (3.38)$$

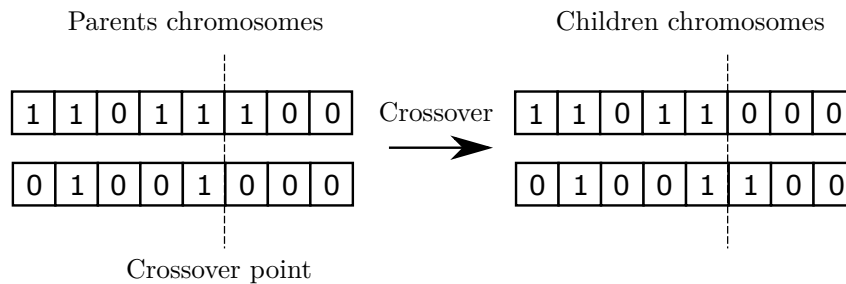
$$P_{ind} = \frac{F'}{sum(F')_{pop}} \quad (3.39)$$

The GA uses principles of selection of the fittest to move towards optimum solution from the initial population. The individual selection process for reproduction is based on two methods:

- **Elitism:** individuals with the best fitness are selected and added to the next generation population. These best individuals direct selection process is used to ensure that at least a percentage of the best individuals in each generation will be selected for mating. A typical elitism percentage ( $p_e$ ) of 5% was used on the morphing winglet optimization.
- **Roulette wheel selection:** next population remaining individuals are selected using fitness proportionate selection. Each individual has a selection probability proportional to its fitness, so fittest individuals have greater chances of being selected. A random selection is made based on the probabilities, defining the individuals that will be mated. The method is similar to a roulette wheel in a casino, where a ball is randomly spun and has a chance to stop on the roulette numbers.

The selected individuals are paired and undergo the crossover process. This process is responsible for the evolution and optimum-wise movement of the solution. Crossover consists of a random chromosome parts exchange between selected couples. The crossover point is randomly selected and all chromosome information after this point is exchanged between the mated individuals, generating the next generation population. Figure 19 illustrates the crossover process.

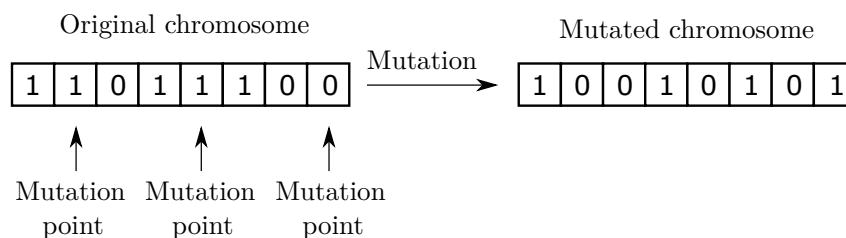
Figure 19: Crossover process example



Source: The author

These new individuals are then subjected to a mutation process. Mutation process consists of random change on chromosome information that occurs with a certain probability. This process is responsible for inserting genetic variability on the population, avoiding premature and local optimal convergence. However, high mutation probability ( $p_m$ ) can insert bad individuals on the population, delaying convergence. The  $p_m$  was selected by testing values and analysing solution convergence on a fixed condition camber morphing winglet problem, being  $p_m = 0.25\%$  chosen as final value. Figure 20 illustrates the mutation process.

Figure 20: Crossover process example



Source: The author

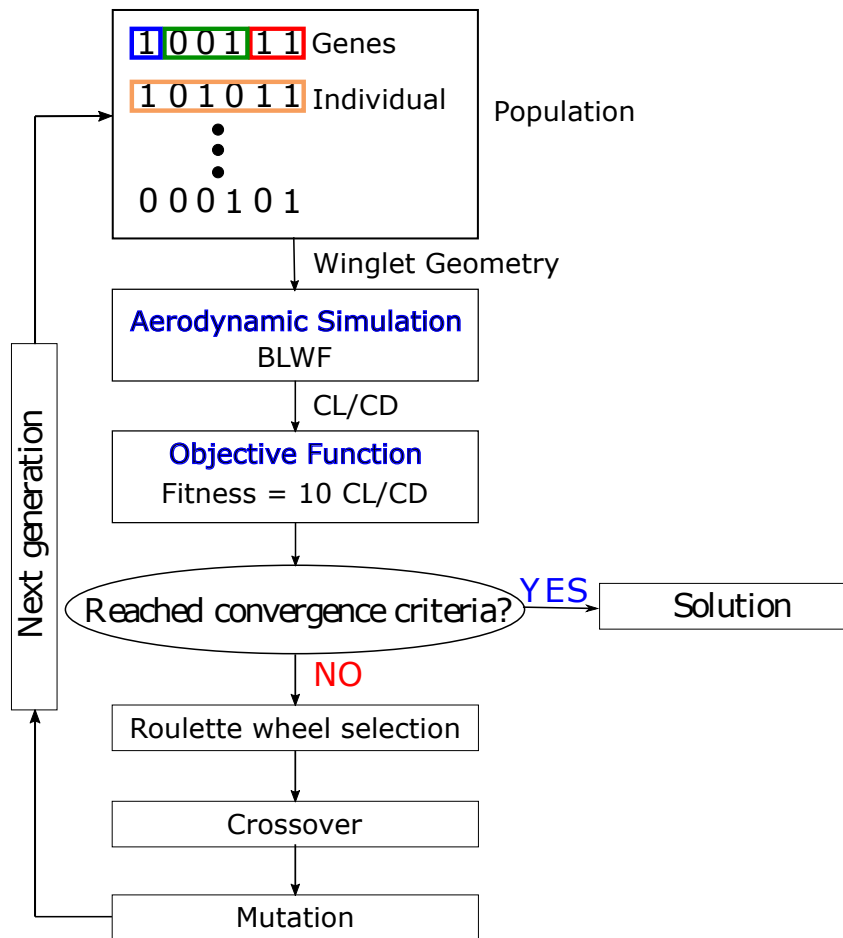
A new population is defined after mutation. The individuals of the new generation are evaluated, selected, subjected to crossover and mutation like the previous generation, defining a new generation. This process is repeated until the convergence criterion is reached. Figure 21 shows a representation of the GA used in this study.

The GA solution quality is very sensitive to population size and number of generations for convergence. Thierens e Goldberg (1994) suggested that the minimum population size ( $n_{min}$ ) and minimum number of generations ( $g_{conv_{min}}$ ) for convergence to a global optimum are  $n_{min} = 2l$  and  $g_{conv_{min}} = \frac{\pi}{2} \sqrt{2\pi l}$ , where  $l$  is the chromosome length. An analysis on the influence of  $n$  and  $g_{conv}$  was done to validate the minimum values suggested by Thierens e Goldberg (1994).

According to the method presented by Thierens e Goldberg (1994), an estimative

on the minimal population size and generations can be made from the chromosome length. The camber morphing winglet optimization chromosome has  $l = 40$ , then calculated values are  $n_{min} = 80$  and  $g_{conv_{min}} = 18$ . In order to check convergence, populations of size  $n = 10g_{conv}$  were tested on a camber morphing winglet optimization for climb condition. The best fitness after  $g_{conv}$  was compared for the different population sizes. The results show that  $n = 300$  and  $g_{conv} = 30$  are the minimum population size and number of generations required to ensure convergence (Fig. 22).

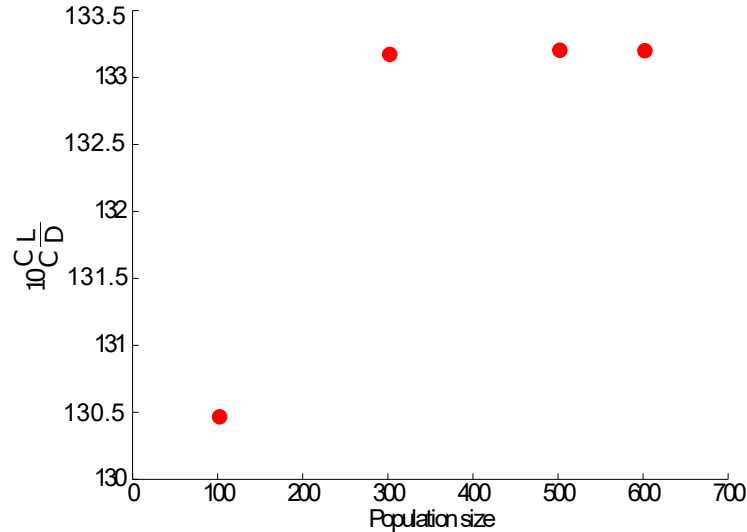
Figure 21: Genetic algorithm optimization process block diagram



Source: The author

After the GA code validation and parameters analysis, the camber morphing winglet GA optimization parameters were selected as shown in Table 4. A maximum of 30 generations was chosen as stop criterion, ensuring convergence according to available computing resources. These parameters were used on both the single point and full mission optimizations.

Figure 22: Population size and number of generations influence on optimum individual fitness



Source: The author

Table 4: GA parameters used on the camber morphing winglet optimization

$n$ [-]	$g_{conv}$ [-]	$l$ [-]	$N^\circ$ Variables	$p_m$ [%]	$p_e$ [%]
300	30	40	10	0.25	5

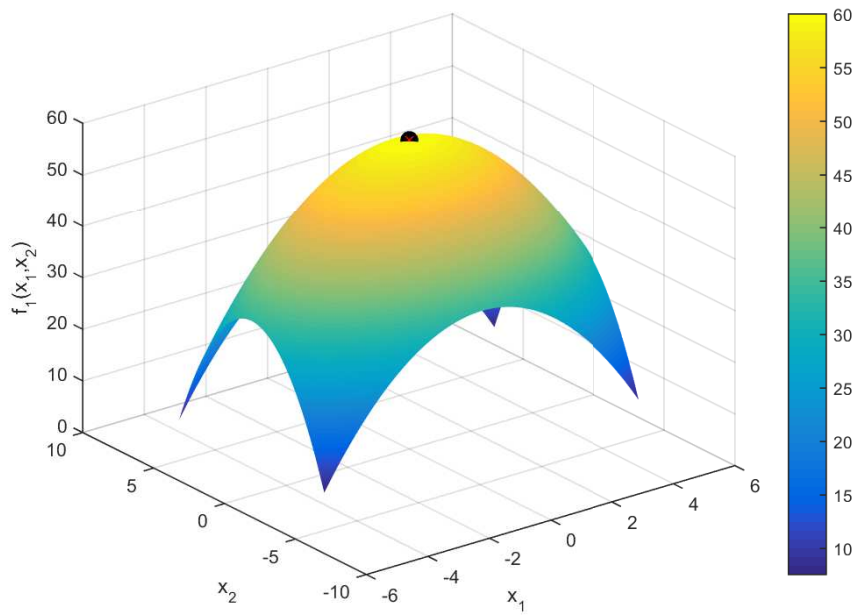
Source: The author

Four test functions, base on De Jong (1975) proposition, were used to check GA capability to find optimum using the set of parameters on Table 4. This validation functions equations are shown on Table 5 . The GA was able to find an optimal solution for all cases, being tested for a total of 50 random initial populations tested for every function (Fig. 23 to 26). Table 6 shows function maximum compared to GA found optimum value, showing that the select GA parameters ensure convergence towards the global optimum.

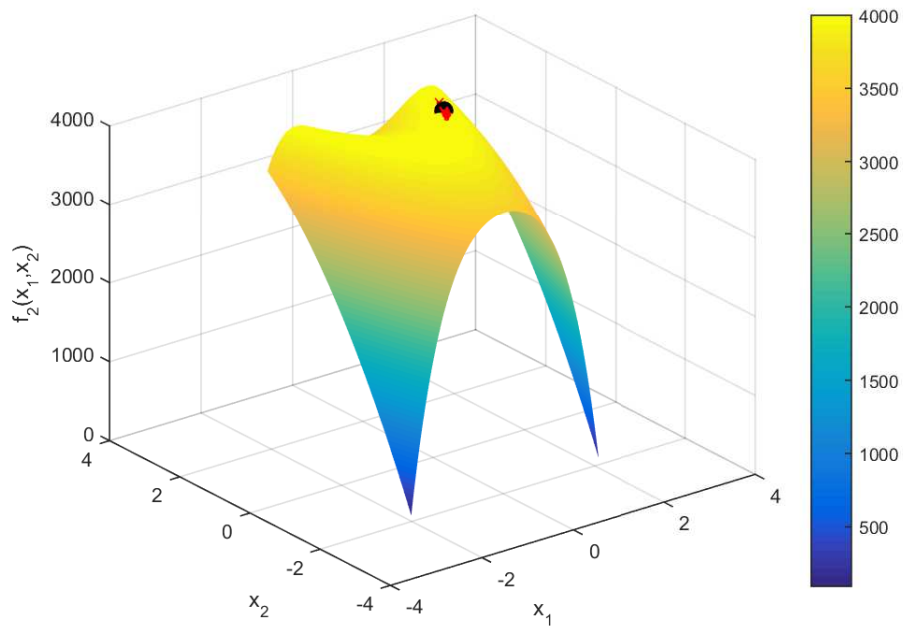
Table 5: Test functions for GA validation

Function ( $f$ )	Limits
$f_1(x_1, x_2) = 60 - \sum_{i=1}^2 x_i^2$	$-5.12 \leq x_i \leq 5.12$
$f_2(x_1, x_2) = 4000 - 100(x_1^2 - x_2)^2 - (1 - x_1^2)$	$-2.048 \leq x_i \leq 2.048$
$f_3(x_1, x_2) = 60 - \sum_{i=1}^2 \text{floor}(x_i)$	$-5.12 \leq x_i \leq 5.12$
$f_4(x_1, x_2) = 1250 - \sum_{i=1}^2 ix_i^2$	$-1.28 \leq x_i \leq 1.28$

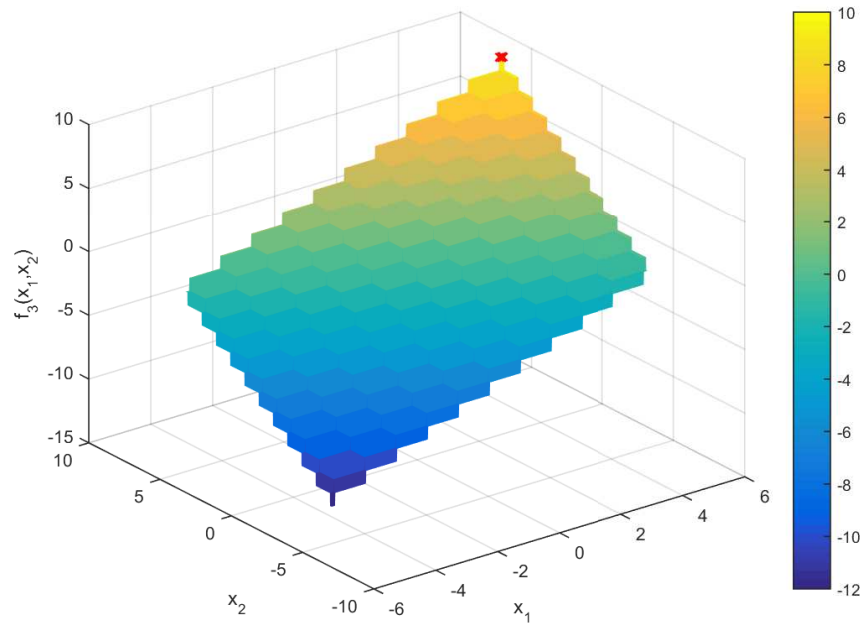
Source: The author

Figure 23:  $f_1$  surface and maximum compared to GA optimum points

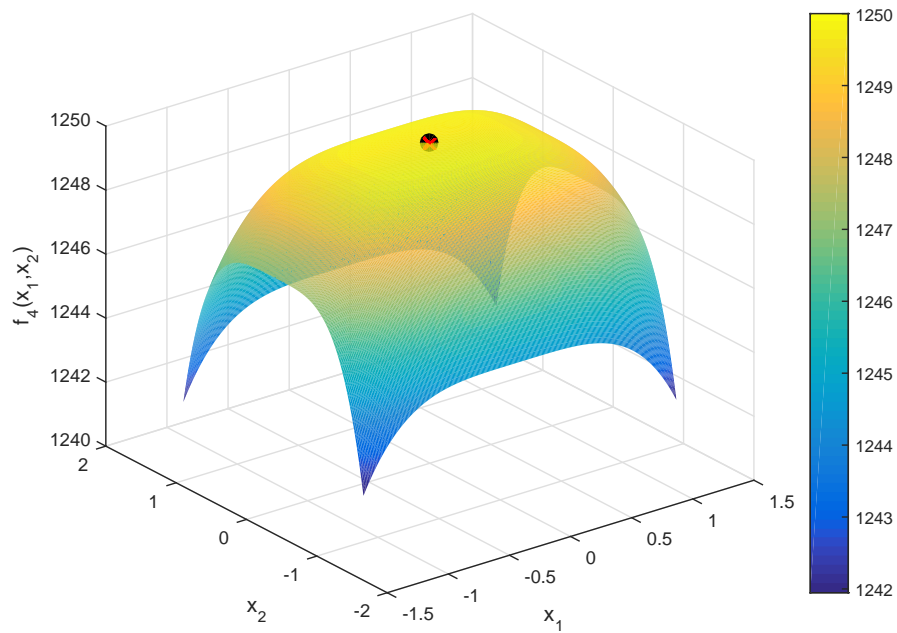
Source: The author

Figure 24:  $f_2$  surface and maximum compared to GA optimum points

Source: The author

Figure 25:  $f_3$  surface and maximum compared to GA optimum points

Source: The author

Figure 26:  $f_4$  surface and maximum compared to GA optimum points

Source: The author

Table 6: GA validation results

Function ( $f$ )	$f_{max}$	GA max	GA error [%]
$f_1$	60	59.99	0.02
$f_2$	4000	3999	0.25
$f_3$	10	10	0
$f_4$	1250	1250	0

Source: The author

### 3.5 Aerodynamic Model

Business jet flight envelop includes subsonic and transonic conditions at a great range of Reynolds ( $Re$ ) and Mach numbers ( $M$ ). The chosen aerodynamic evaluation software must simulate Reynolds variation and transonic effects, calculating influence on lift and drag with reasonable precision so different winglets geometries can be compared.

The lifting-line and vortex-lattice methods do not simulate transonic effects, making them not proper for this work. CFD codes are capable of simulating both viscous and transonic effects making them a possible choice for the aerodynamic analysis. However, the GA is an evolutionary algorithm, based on the analysis of a population of individuals for some generations. These individuals must be simulated so they can be evaluated at every generation. Using a CFD code for aerodynamic simulation would be very time consuming, being a faster solver needed.

BLWF code is a fast aerodynamic evaluation tool, capable of performing preliminary aerodynamic analysis on transonic transport aircraft configurations. The German Aerospace Center (DLR) compared wing-fuselage configuration BLWF simulation with wind tunnel experiments results, analysing the code lift and drag estimation accuracy (ZHANG; HEPPERLE, 2010). BLWF was able to estimate with reasonable accuracy lift, drag and lift to drag ratio for Mach numbers smaller than model drag divergence Mach number, finding good results for Mach up to  $m = 0.9$ . The simulation accuracy increases the smaller the Mach number. The results showed that the BLWF code is well suitable subsonic and transonic aerodynamic tool for a preliminary analysis of transonic transport aircraft configurations, as a business jet.

The BLWF (KARAS; KOVALEV, 2004) code adopts the full potential governing equations coupled with an integral boundary layer subroutine. Jameson e Caughey (1977) presents the full potential model equations and conditions. Air density ( $\rho$ ) is not considered constant on mass conservation equation (Eq. 3.40) and is calculated using the isentropic formula (Eq. 3.42). Velocities components ( $u, v, w$ ) are calculated from velocity potential ( $\Phi$ ) as shown on Eq. 3.41. The pressure ( $p$ ) and air speed ( $V$ ) are normalized on the far field as  $p = 1$  and  $V = 1$ . This way the pressure ( $p$ ) and speed of sound ( $a$ ) are calculated

using Eq. 3.43 and 3.44.

$$\frac{\partial(\rho u)}{\partial x} + \frac{\partial(\rho v)}{\partial y} + \frac{\partial(\rho w)}{\partial z} = 0 \quad (3.40)$$

$$u = \frac{\partial\Phi}{\partial x} \quad v = \frac{\partial\Phi}{\partial y} \quad w = \frac{\partial\Phi}{\partial z} \quad (3.41)$$

$$\rho = \left(1 + \frac{\gamma-1}{2} M_\infty^2 (1 - V^2)\right)^{\frac{1}{\gamma-1}} \quad \text{where} \quad V^2 = u^2 + v^2 + w^2 \quad (3.42)$$

$$p = \frac{\rho^\gamma}{\gamma M_\infty^2} \quad (3.43)$$

$$a^2 = \frac{\rho^{\gamma-1}}{M_\infty^2} \quad (3.44)$$

Airspeed on far field is defined as constant and equal to  $M_\infty$  and normal velocity ( $u_n$ ) is equal zero on body surface. Additionally, it is considered continuity of  $\Phi$  and  $\rho u_n$  on shock jump. Wave drag is calculated from the variation of normal velocity through shock wave under the isentropic assumption.

Jameson e Caughey (1977) describes the finite volume method used for solving the full potential equations on BLWF. The integral boundary layer subroutine method used on the software is described by Mclean e Randall (1978). BLWF also includes a mesh generator for all surfaces, as described by Yu (1980). BLWF generates an initial mesh that is used for aircraft simulation. A second mesh is generated by refining the first mesh using the results from the first simulation and another solution is calculated using the new mesh.

Geometry information and conditions for calculations are given using a text document as defined on the software manual (KARAS; KOVALEV, 2004). An example of the input file is given in Appendix A. The aerodynamic simulations are performed at every optimization point, with fixed  $C_L$ ,  $M$  and  $Re$ . The program outputs aircraft's parts individual  $C_L$ ;  $C_D$  components and lift distribution over lifting surfaces. These coefficients are used to evaluate aircraft performance at each condition during the optimization process.

## 3.6 Single point optimization

### 3.6.1 Optimization structure

The single point optimization consisted of optimizing winglet sections camber using the genetic algorithm for a fixed flight condition. A wing, winglet and fuselage configuration was used on the single point optimization, being defined four conditions similar to flight phases in a business jet envelop. All four conditions are fixed, so no weight variations were considered throughout the optimization process.

The climb condition was chosen for the camber morphing winglet single point optimization for demanding higher values of  $C_L$ , implying in high induced drag. Adapting the winglet geometry to an optimum configuration can have great impact on time to climb and mission fuel consumption, making an investigation on camber morphing winglet effectiveness on climb necessary.

During the cruise phase, the lift coefficient is smaller than on climb due to the high flight speed. However, most of the flight time is spent on cruise and weight has considerable variation during this phase, and so does lift coefficient. This way, the camber morphing winglet could adjust the winglet geometry to maximize the performance of the aircraft during cruise, having a great impact on fuel consumption. Three cruise corresponding to cruise right after finishing climb (heavy cruise), at the middle of the mission (mid cruise) and right before descent (light cruise) were selected for single point optimization.

The conditions are defined according to its lift, Reynolds and Mach numbers as shown in Table 7. The lift coefficient for the flight conditions was determined using basic operating weight (BOW), payload, flight speeds and fuel capacity averages for midsize business jet category (BUSINESS & COMMERCIAL AVIATION, 2015) and using the fuel-fraction method presented by Roskam (2015).

Table 7: Parameters of conditions on camber morphing winglet optimization

<b>Flight condition</b>	$Re[-]$	$M[-]$	$C_L[-]$
Climb	$14.8 \times 10^6$	0.6	0.5150
Heavy cruise	$9.75 \times 10^6$	0.75	0.4885
Mid cruise	$9.75 \times 10^6$	0.75	0.4525
Light cruise	$9.75 \times 10^6$	0.75	0.4165

Source: The author

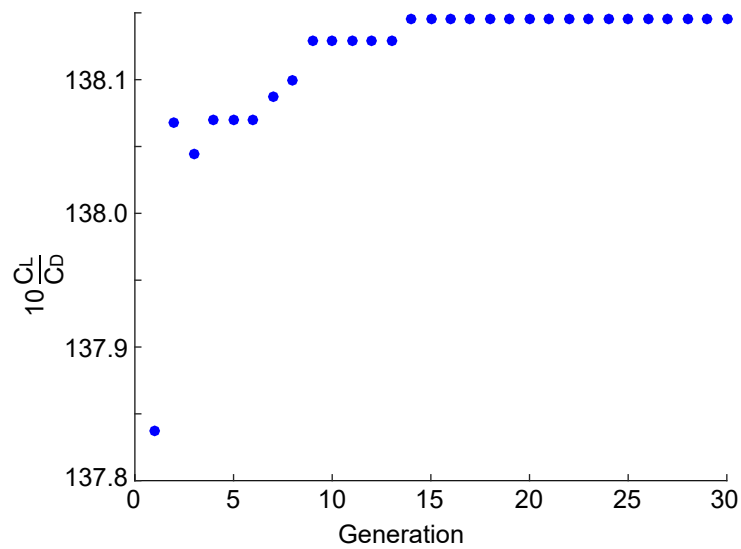
### 3.6.2 Results

The GA optimization (Section 3.4) was performed adopting the flight conditions described on Section 3.6.1. An analysis of the population fitness and winglets geometry evolution throughout generations was made to investigate solution behavior.

Population best, the worst and mean individuals fitness evolution for each condition are shown in Fig. 27 to 34. The best individuals show fitness improvement until around the 15<sup>th</sup> generation, showing that the generation number was overestimated. Steps on fitness increase are seen for all cases, showing that the GA finds locally optimum geometries and is able to avoid getting stuck at them. However, fitness variation from first generation best individual to optimum is small. This can be caused by population size bigger than the necessary for optimization, generating well-fitted individuals on first generations.

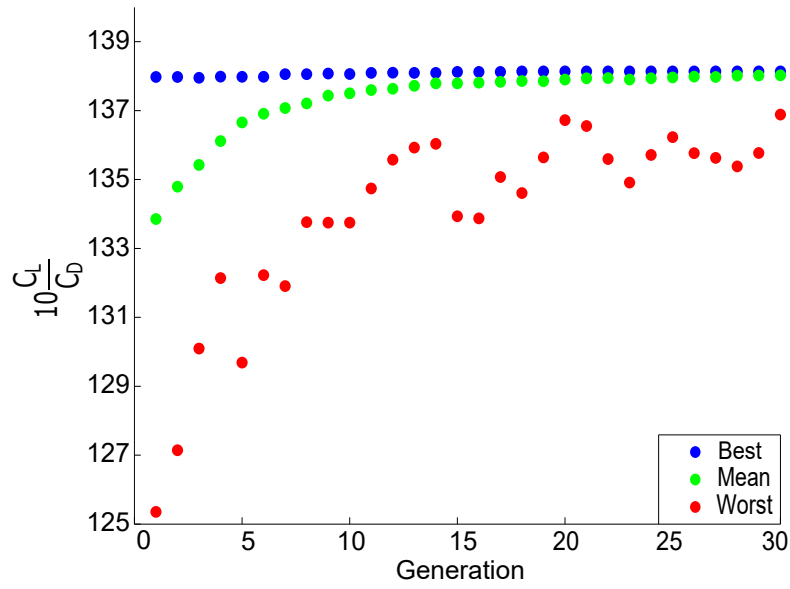
Analysing the fitness evolution of the mean and worst individuals throughout generations, a clear convergence to an optimum can be seen after 30 generations. Both mean and worst individuals fitness move towards the best individual fitness, despite oscillations on worst individual fitness due to random bad individuals generation caused by the mutation process.

Figure 27: Best evolution through the generations for climb condition



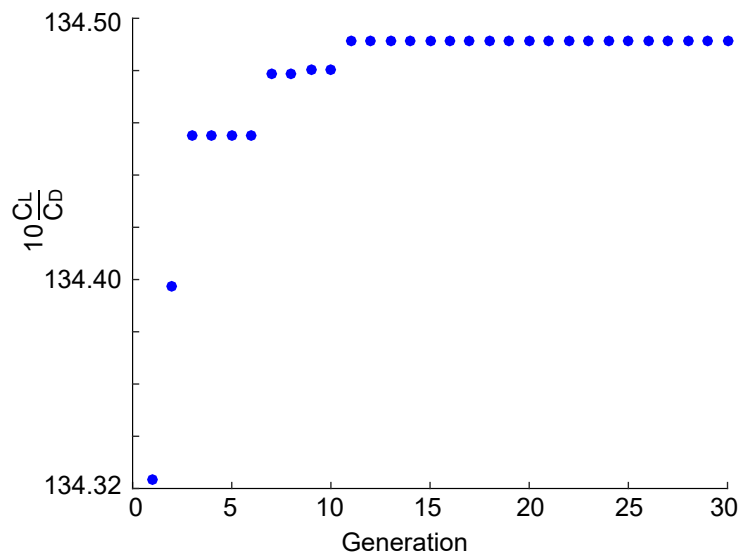
Source: The author

Figure 28: Best, worst and mean individual fitness evolution through the generations for climb condition



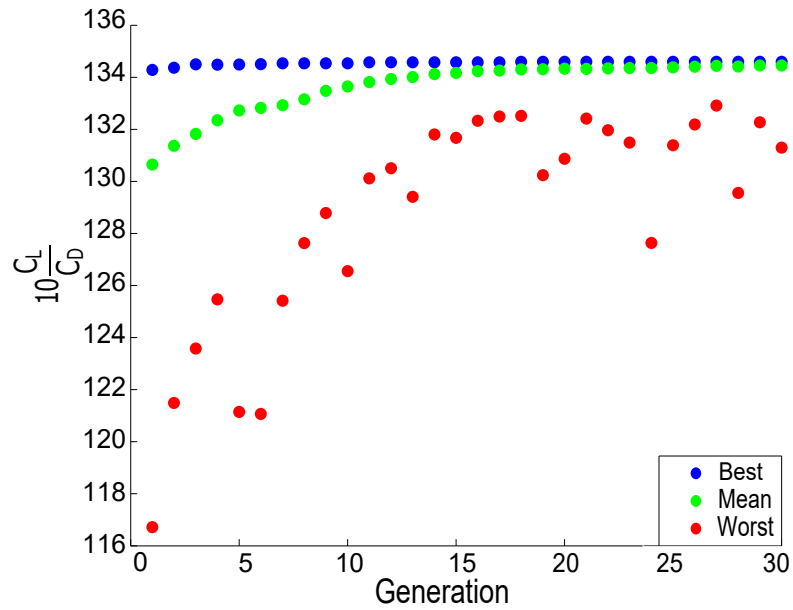
Source: The author

Figure 29: Best individual fitness evolution through the generations for heavy cruise condition



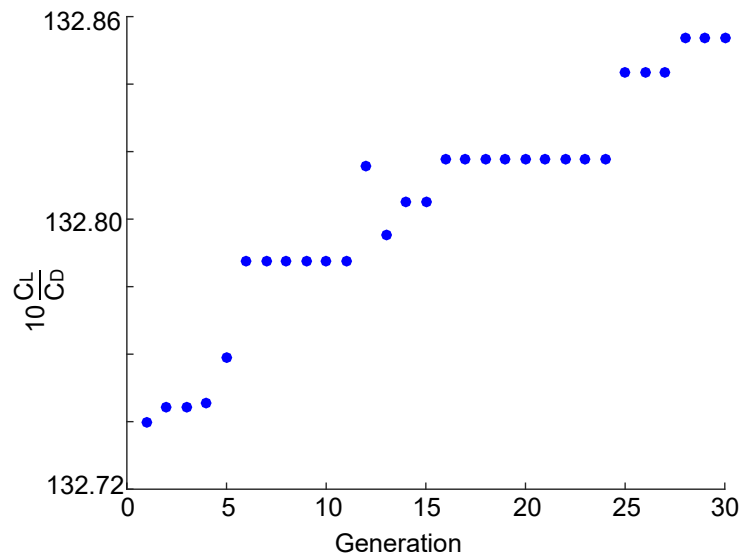
Source: The author

Figure 30: Best, worst and mean individual fitness evolution through the generations for heavy cruise condition



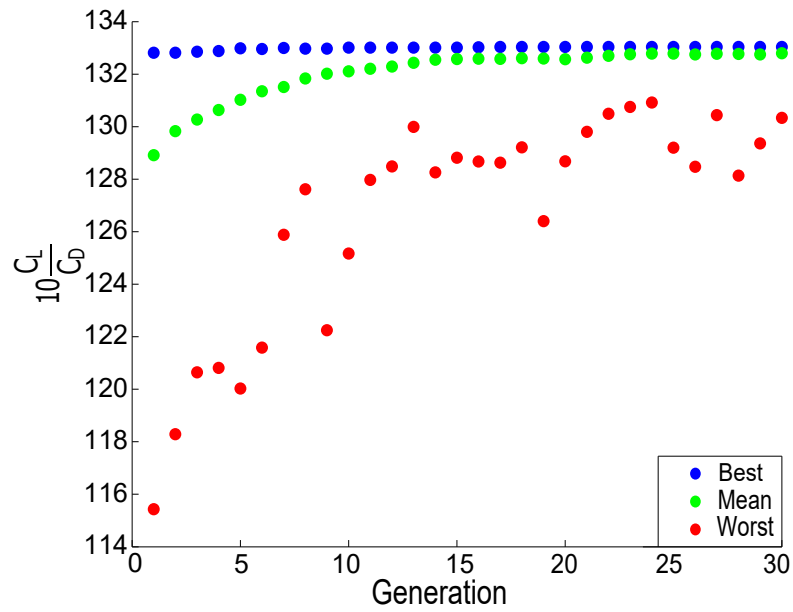
Source: The author

Figure 31: Best individual fitness evolution through the generations for mid cruise condition



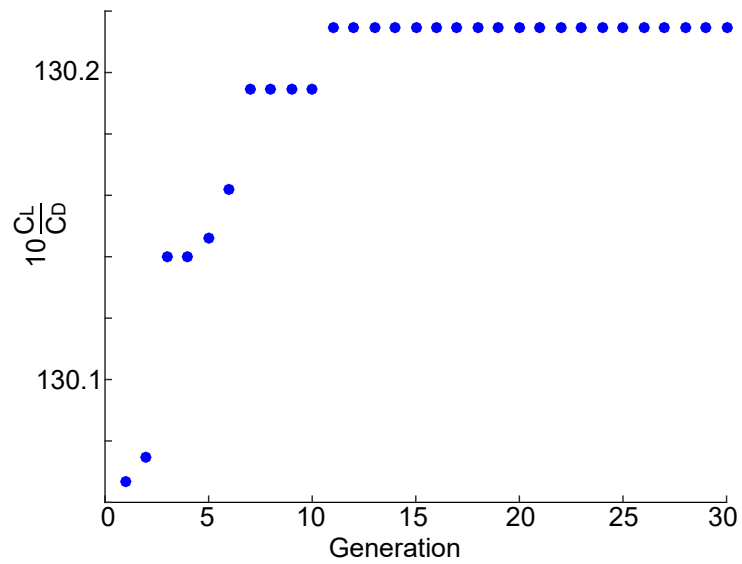
Source: The author

Figure 32: Best, worst and mean individual fitness evolution through the generations for mid cruise condition



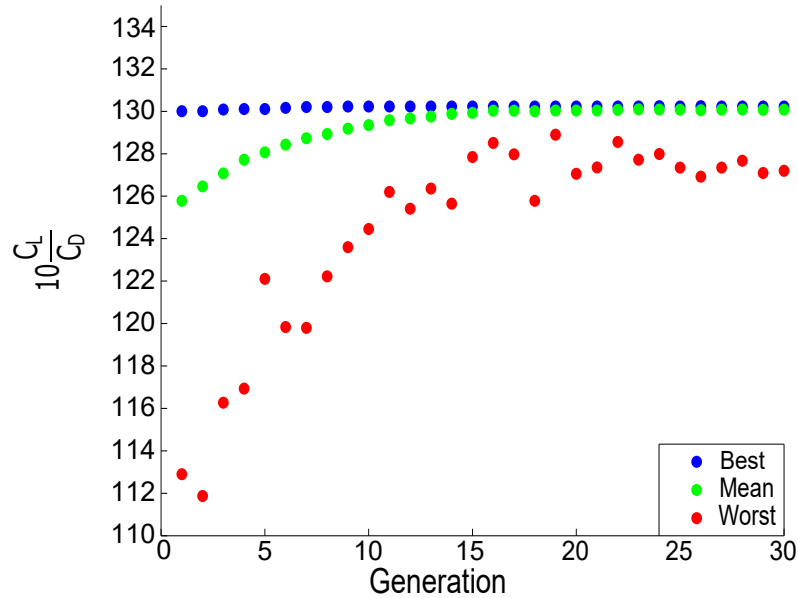
Source: The author

Figure 33: Best individual fitness evolution through the generations for light cruise condition



Source: The author

Figure 34: Best, worst and mean individual fitness evolution through the generations for light cruise condition



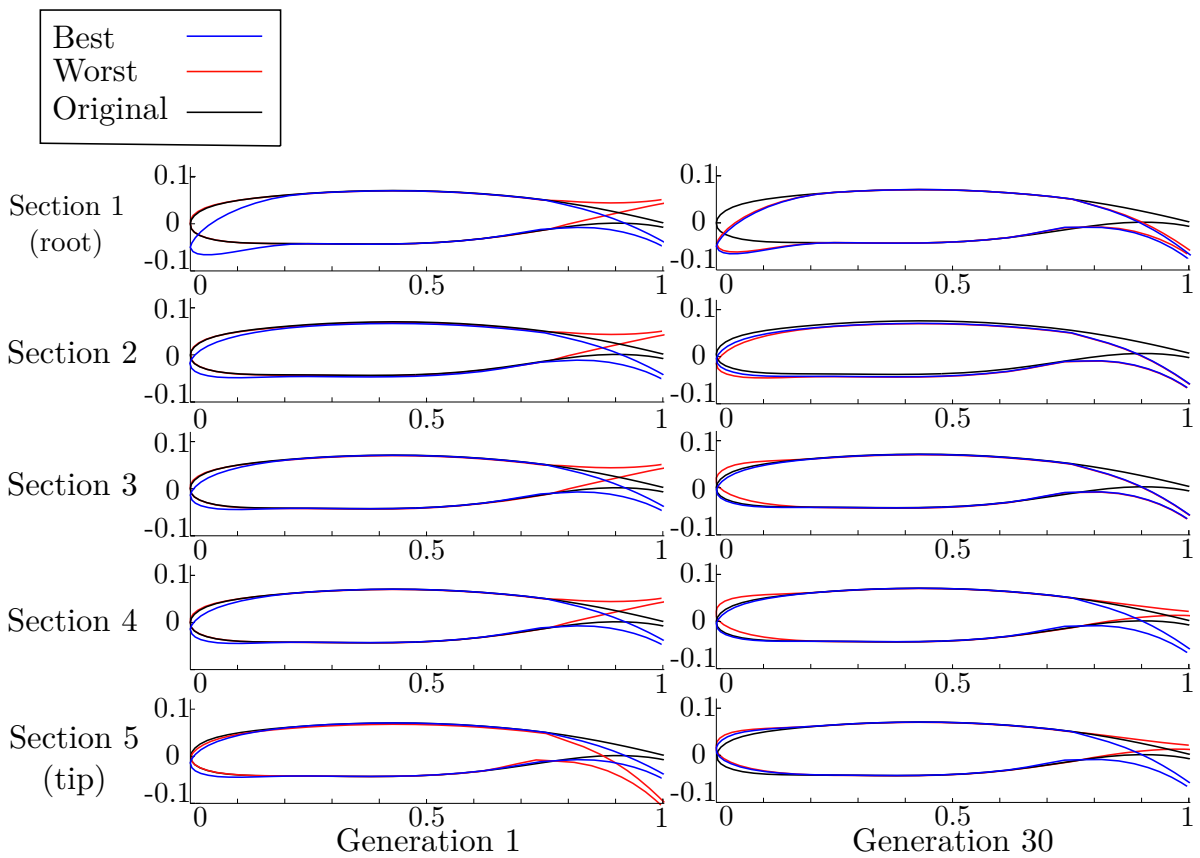
Source: The author

An investigation on camber variation throughout winglet span and optimization generations (Figures 35 to 38) was made to check if the results correspond to the expected camber variation tendencies. The original airfoil is shown on figures to help to understand the differences of the optimized sections.

The climb configuration root section exhibits a great angle on both leading and trailing edge, resulting in a very cambered airfoil. Following sections still have great trailing edge angles but presents almost no leading edge angle. The same trend is seen on the leading edge of all cruise configurations. Cerón-Muñoz e Catalano (2006) measurements show that that lateral flow angle on winglet reduces on winglet spanwise direction, requiring more camber on the root section than on others. The optimization camber variation on the spanwise direction is in accordance with these experimental results.

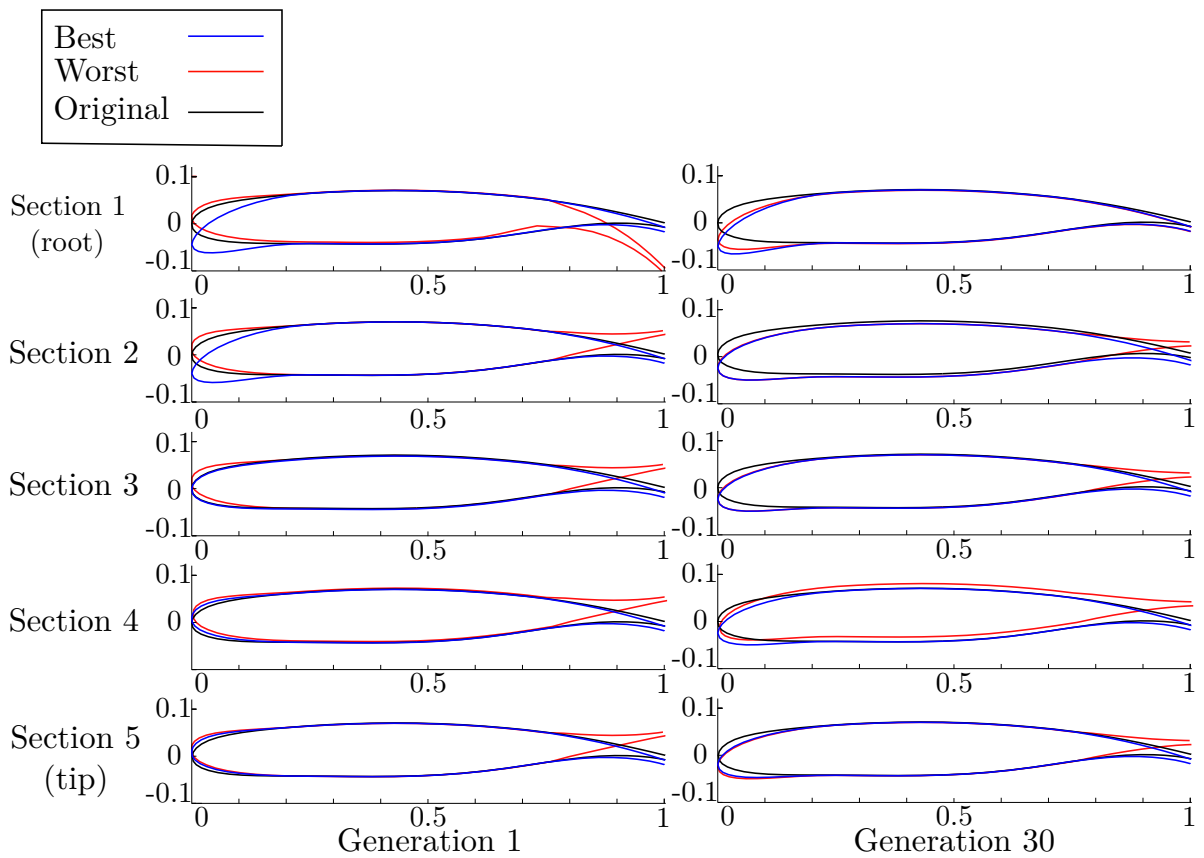
Smaller  $C_L$  implies less induced drag and smaller induced angles on winglet sections, resulting in less cambered sections. Optimization section evolution shows a leading and trailing edge deflections decrease with  $C_L$  reduction, meeting the literature expectations.

Figure 35: Evolution of sections airfoil of the best and worst individual through the generations for climb condition



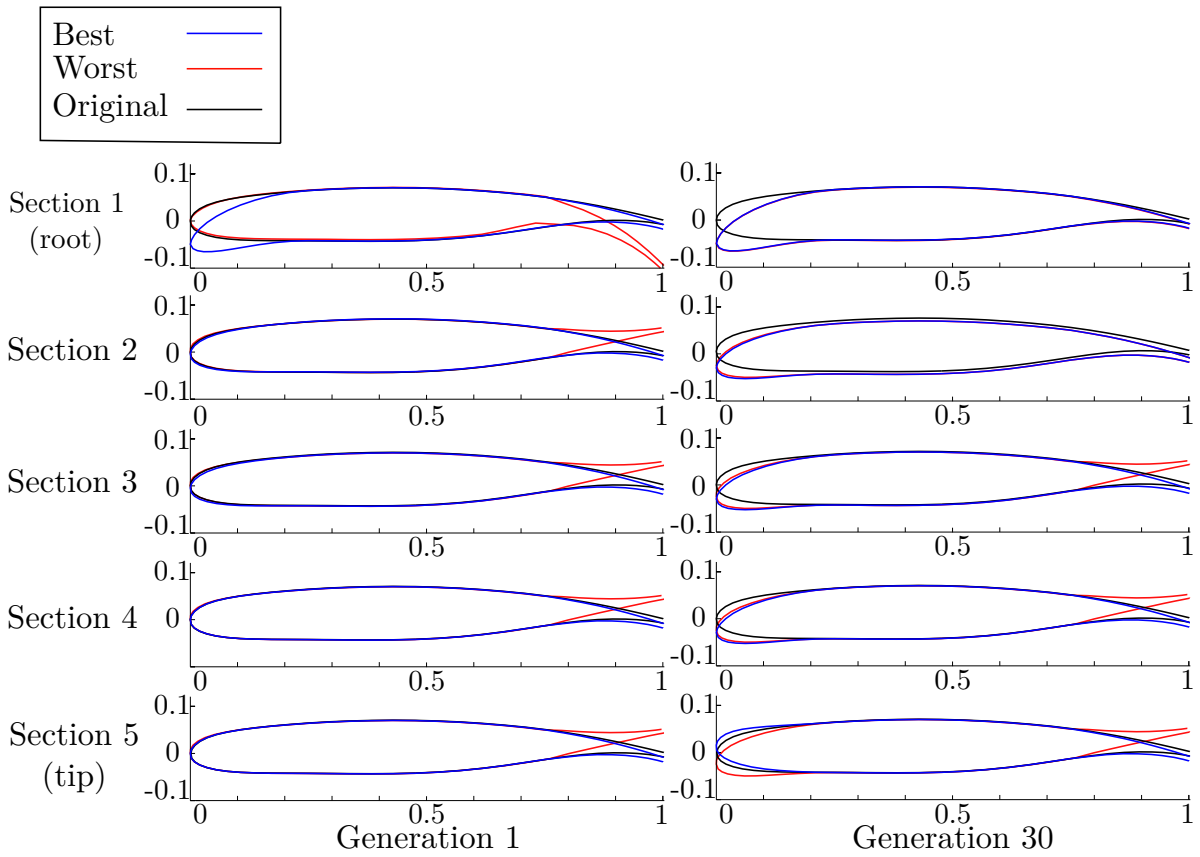
Source: The author

Figure 36: Evolution of sections airfoil of the best and worst individual through the generations for heavy cruise condition



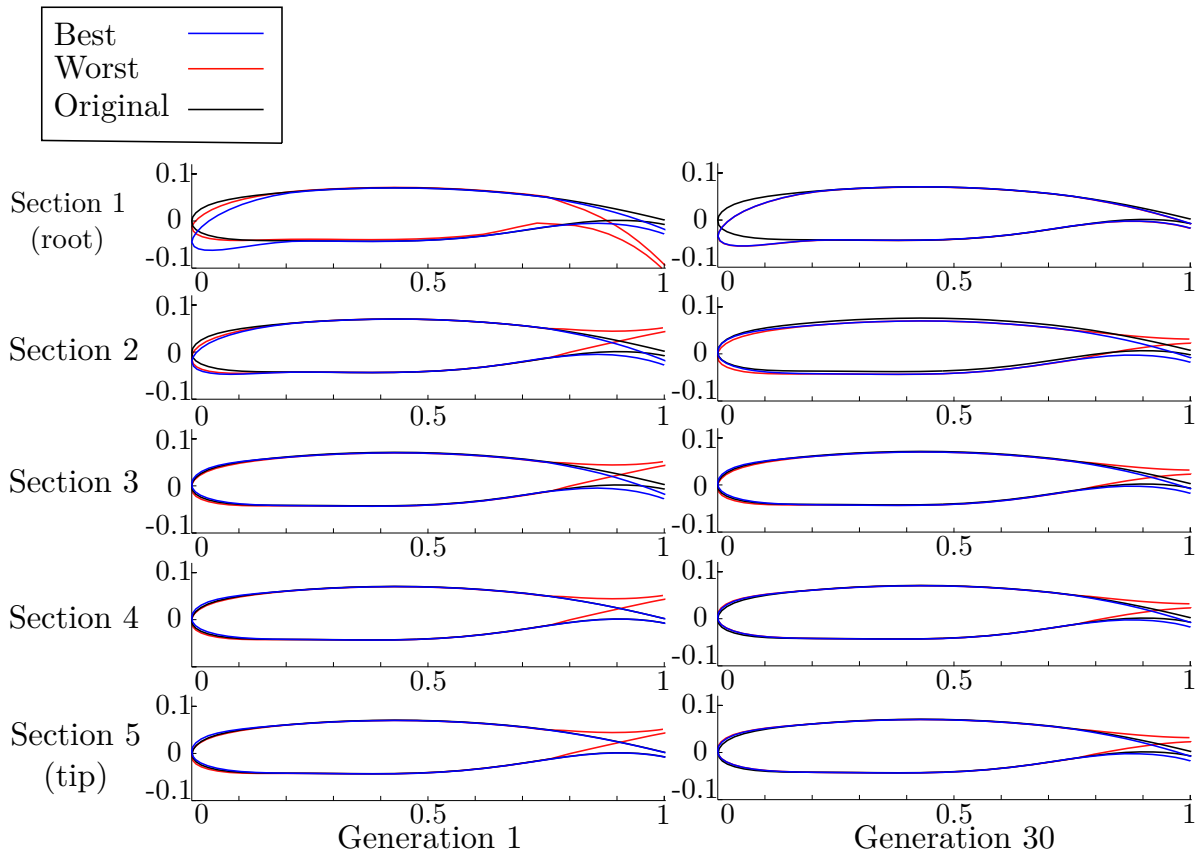
Source: The author

Figure 37: Evolution of sections airfoil of the best and worst individual through the generations for mid cruise condition



Source: The author

Figure 38: Evolution of sections airfoil of the best and worst individual through the generations for light cruise condition



Source: The author

Table 8 and 9 show the total and induced drag components for the four flight conditions, comparing optimized geometry with baseline fixed geometry winglet. Both total and induce drag are reduced with the morphing winglet, however, the reduction on total drag is bigger than induced drag reduction at three of them. This shows that the camber morphing was able to reduce other lift independent drag components. The heavy cruise geometry was the only one that induced drag reduction was bigger than total drag reduction.

Table 8: Total drag comparison between baseline and optimized camber morphing winglets

Condition	$C_{D_{total}} (\times 10^{-4}) [-]$		$C_{D_{induced}} (\times 10^{-4}) [-]$	
	Baseline	Optimized	$\Delta C_D$	$\% \Delta C_D$
Climb	377.4	375.2	-2.2	-0.58
Heavy cruise	362.6	362.5	-0.1	-0.03
Mid cruise	343.2	342.7	-0.5	-0.15
Light cruise	321.8	321.3	-0.5	-0.16

Source: The author

Table 9: Induced drag comparison between fixed geometry and optimized camber morphing winglets

<b>Condition</b>	$C_{D_{total}} (\times 10^{-4}) [-]$		$C_{D_{induced}} (\times 10^{-4}) [-]$	
	<b>Baseline</b>	<b>Optimized</b>	$\Delta C_D$	$\% \Delta C_D$
Climb	75.0	74.2	-0.8	-1.1
Heavy cruise	66.5	66.1	-0.4	-0.6
Mid cruise	58.6	58.2	-0.4	-0.7
Light cruise	49.9	49.6	-0.3	-0.6

Source: The author

### 3.7 Mission optimization

Mission optimization was performed using the typical business jet mission profile, which was divided by time steps of different sizes resulting in 19 optimization points including climb, cruise and descent conditions. The full configuration (wing, fuselage, winglet, nacelle and tail) was used on the mission optimization.

Aircraft take off weights are based on Legacy 500 values (BUSINESS & COMMERCIAL AVIATION, 2015). Lift was calculated based on calculated aircraft weights, lift, speed and altitude at every selected point as defined on Section 3.3. Based on calculated  $C_L$ ,  $Re$  and  $M$ , BLWF code simulations were performed for estimating winglets geometries  $C_D$  (Section 3.5). The simulation results are used at the GA (Section 3.4 for finding the best configuration for the given condition). The optimum configuration aerodynamic coefficients are used on the presented performance equations for calculation of aircraft acceleration,  $RoC$ , required thrust,  $RoD$  and fuel consumption. After these calculations, the next condition is defined based on weight, height and speed variations. Take off and landing phases are exceptions aircraft weight variation is calculated using the weight fraction method (ROSKAM, 2015) due to the difficulty of simulating these conditions without flap and slats information. No control surface deflections were applied and no stability calculations were performed during the mission simulation. Tables 10 and 11 show mission optimization points parameters for the two mission simulations.

Table 10: Maximum range mission optimization points parameters

Range = 3125 NM			TOW = 16100 kg			
Condition	W [kg]	h [ft]	V [ $\frac{m}{s}$ ]	$C_L$ [-]	$M$ [-]	$Re$ [6]
Climb	15775	1500	102	0.60	0.30	17.1
	15760	1500	157	0.25	0.47	26.5
	15736	6540	170	0.25	0.51	25.3
	15713	10000	182	0.24	0.55	24.8
	15688	10000	192	0.22	0.58	26.2
	15626	22300	235	0.22	0.75	23.1
	15573	29400	243	0.26	0.80	19.4
	15521	38000	236	0.39	0.80	14.1
Cruise	15478	43000	236	0.49	0.80	11.1
	15437	43000	236	0.49	0.80	11.1
	14954	43000	236	0.47	0.80	11.1
	14441	43000	240	0.44	0.81	11.2
	13941	43000	240	0.43	0.81	11.2
	13633	43000	240	0.42	0.81	11.2
	13161	43000	240	0.40	0.81	11.2
	12714	43000	240	0.39	0.81	11.2
	12278	43000	240	0.38	0.81	11.2
	12061	45000	240	0.41	0.81	10.2
Descent	12057	35300	241	0.26	0.81	16.1

Source: The author

Table 11: 1000 NM mission optimization points parameters

Range = 1000 NM			TOW = 12700 kg			
Condition	W [kg]	h [ft]	V [ $\frac{m}{s}$ ]	$C_L$ [-]	$M$ [-]	$Re$ [6]
Climb	12441	1500	102	0.47	0.30	17.1
	12426	1500	157	0.20	0.47	26.5
	12403	8100	174	0.19	0.53	24.2
	12381	10000	190	0.17	0.58	24.8
	12356	10000	192	0.17	0.58	26.2
	12299	26200	247	0.16	0.80	20.4
	12246	37700	236	0.22	0.80	14.2
	Cruise	12210	43000	236	0.30	0.80
11953		43000	240	0.37	0.81	11.1
11844		45000	240	0.36	0.81	10.1
11742		45000	240	0.36	0.81	10.1
11639		45000	240	0.36	0.81	10.2
11542		45000	240	0.35	0.81	10.2
11442		45000	240	0.35	0.81	10.2
11342		45000	240	0.35	0.81	10.2
11245		45000	240	0.35	0.81	10.2
Descent		11242	35460	240	0.34	0.81
	11236	30000	253	0.34	0.83	19.4
	11233	12000	198	0.35	0.61	34.3

Source: The author

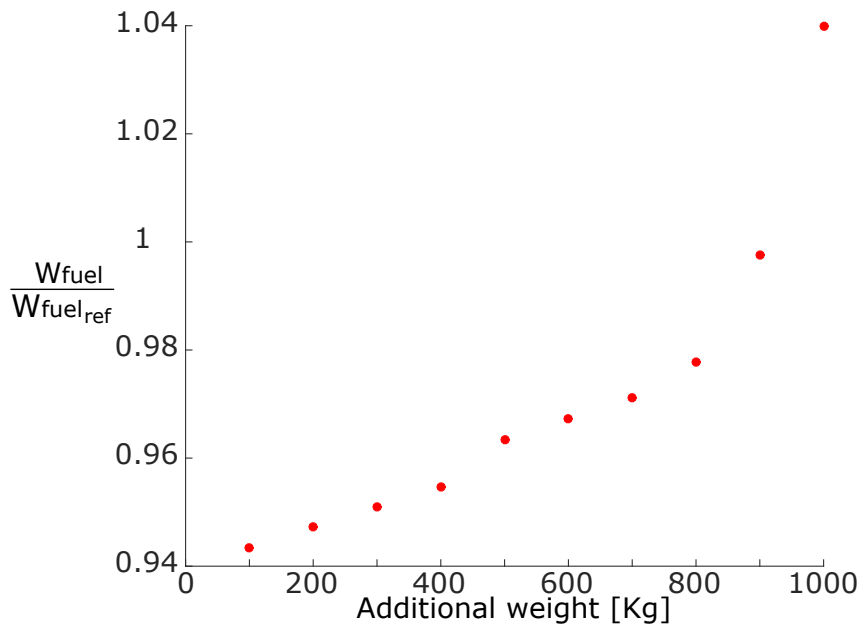
Table 12 presents the comparison of the simulation results from the original fixed geometry and camber morphing winglet.

Table 12: Mission simulation results

<b>Range = 3125 NM</b>			
	<b>Original winglet</b>	<b>Camber morphing winglet</b>	<b><math>\Delta</math> [%]</b>
Time to climb (@ 430 FL) [min]	18	18	0.0
Climb fuel consumption [kg]	314	314	0.0
Cruise time [h]	6.67	6.67	0.0
Cruise fuel consumption [kg]	3755	3673	-2.2
Mission fuel consumption [kg]	4770	4565	-4.3
<b>Range = 1000 NM</b>			
	<b>Original winglet</b>	<b>Camber morphing winglet</b>	<b><math>\Delta</math> [%]</b>
Time to climb (@ 430 FL) [min]	9.7	9.7	0.0
Climb fuel consumption [kg]	252	248	-1.6
Cruise time [h]	2.08	2.08	0.0
Cruise fuel consumption [kg]	1036	1027	-0.9
Mission fuel consumption [kg]	1912	1777	-7.0

Source: The author

Figure 39: Fuel consumption for max range mission with additional weight



Source: The author

The camber morphing winglet achieved the same time to climb as the baseline winglet for both missions, even reducing aircraft fuel consumption on this phase for 1000 NM mission. The most of mission time is spent on cruise condition, so small improvements on this phase can result in great aircraft fuel consumption reduction. Fuel consumption on cruise was reduced for both cases and direct relation with mission length can be seen. The reduction is greater the mission range, once camber morphing winglet adapts its geometry

for best configuration at flight conditions that the baseline winglet works on a sub-optimal regime. Aircraft total fuel consumption reduction can reach up to 7%.

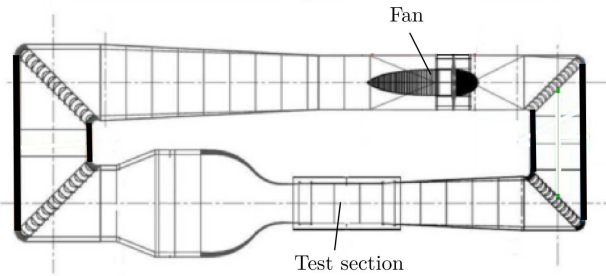
A weight sensitiveness analysis is performed by simulating mission flight with additional weight, in order to check if fuel consumption reduction persists when considering the morphing system weight. The morphing winglet allows the addition of 900 kg for the max range mission consuming the same fuel as the original winglet (Figure 39). This additional load can include the camber morphing system weight and additional payload, showing that the concept brings performance improvements even when its negative effects are considered.



## 4 WIND TUNNEL EXPERIMENT

After the camber morphing winglet numerical evaluation, a couple of wind tunnel experiments were made to validate and investigate the concept effects on the wing aerodynamics. The wind tunnel experiments were carried out on a rectangular closed circuit and test section, with dimensions  $1.68m \times 1.3m \times 3m$ , at the Experimental Aerodynamics Laboratory (LAE) at São Carlos School of Engineering (EESC-USP). The wind tunnel circuit is shown in Fig. 40. This tunnel is equipped with a 110 Hp fan capable of reaching wind speeds of 50 m/s with flow turbulence level of 0.25 %.

Figure 40: Wind tunnel circuit drawing



Source: The author

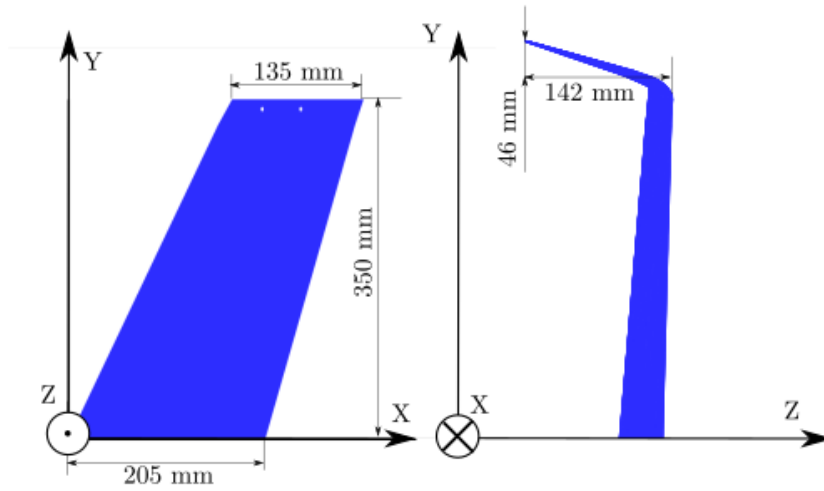
The wing model corresponds to the wing tip part of the aircraft described on Subsection 3.2 on a 1:7.37 scale of the real wing. The model geometry and dimensions are shown in Fig. 41 and Table 13. The model tip allows the installation of different winglet models, being the optimized winglets geometries for the climb; heavy, mid and light cruise conditions, obtained on the single point optimization (Section 3.6), used on the experiment.

Table 13: Midsize business jet main dimensions

$c_{ref}$ [m]	$S_{ref}$ [m <sup>2</sup> ]
$0.174 \pm 0.0005$	$0.0595 \pm 0.00026$

Source: The author

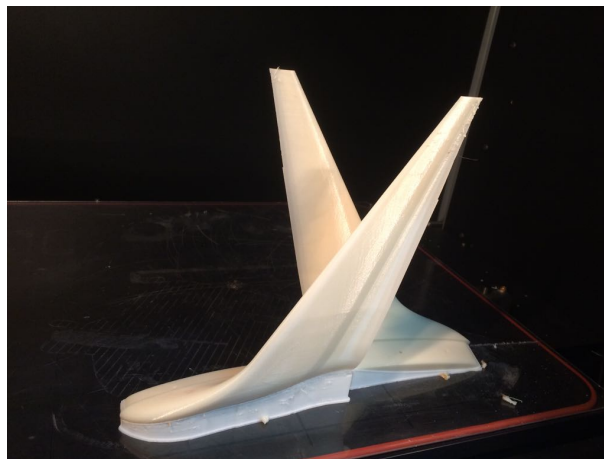
Figure 41: Wing model dimensions and tunnel coordinate system



Source: The author

The wing and winglets models were prototyped using an ABS M30 fuse depositing modeling technique (FDM) on Stratasys Fortus 360MC with a layer thickness of 0.1778 and geometry tolerance of  $\pm 0.127$  mm (Fig. 42). Prototyped surfaces were smoothed using a primer application followed by a water sanding, being this process repeated twice. A final layer of black paint was applied to increase the model's visibility in the test section (Fig. 43).

Figure 42: Prototyped winglet model before surface smoothing and painting



Source: The author

Figure 43: Winglet models used on experiment

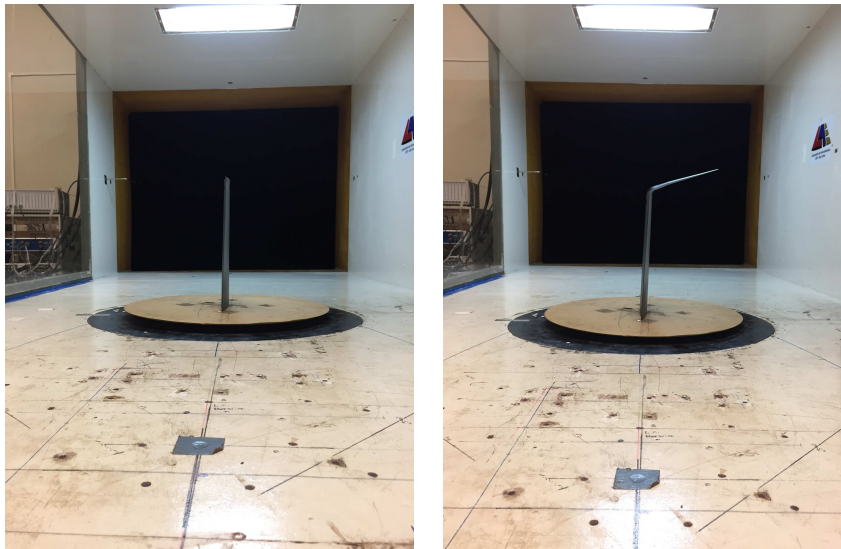


Source: The author

A round plate of diameter of 600 mm is fixed on wing root to reduce tip effects and move the model away from the tunnel walls boundary layer (Fig. 44).

Figure 44: Wing model inside the test section

(a) Model without winglet      (b) Model with light cruise winglet



Source: The author

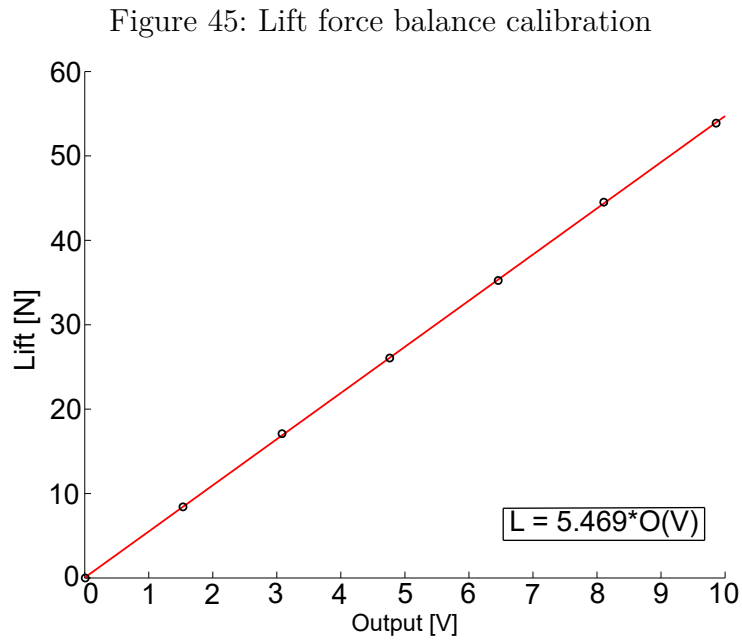
## 4.1 Aerodynamic forces measurement

### 4.1.1 Methodology

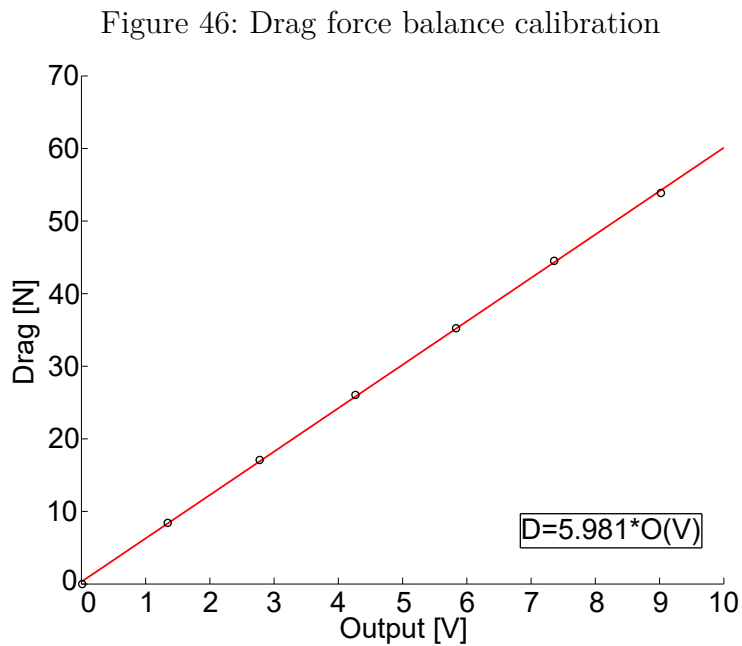
The wind tunnel is equipped with an aerodynamic balance capable of measuring the model lift, drag and pitching moment. Only the lift and drag forces are measured on winglets experiment using a complete bridge with strain gauges assuming independence of the lift and drag measurements.

Both lift and drag are calibrated using a set of known weights to produce a force on these aerodynamic forces directions, reading the voltage output on the acquisition

board and relating the force and voltage output data. The linear regression from Matlab is used to find the relation between applied forces and voltage output with 95 % confidence bounds relation shown in Fig. 45 and 46.



Source: The author



Source: The author

The dynamic pressure is measured using a TSI Model 8705 DEP-CALC micro-manometer with a precision of 1% of reading or  $\pm 1$  Pa.

### 4.1.2 Results

The force measurement was performed on a flow with  $Re = 2.5 \times 10^5$ ,  $M = 0.07$  and  $U_\infty = 25 \frac{m}{s}$ . The wing was tested at a flow incidence angle ( $\alpha$ ) ranging from  $-6^\circ$  to  $25^\circ$  with angle variations ( $\Delta\alpha$ ) of  $1^\circ$ , using a total of 10000 samples during 10 seconds for every measurement. The winglets had a forced transition at 10% of chord with roughness strip and plate drag is removed from all drag data points.

The measurement uncertainty is calculated using the pressure and area measuring tools uncertainty and voltage output measurement variance from the lift and drag bridges applied to the lift and drag coefficients; and lift to drag ratio equations:

$$C_L \pm \Delta C_L = \frac{5.469 \times \left[ O_L(V) \pm \frac{\sigma}{\sqrt{n_{sample}}} \right]}{(q_\infty \pm \Delta q_\infty) (S_{ref} \pm \Delta S_{ref})} \quad (4.1)$$

$$C_D \pm \Delta C_D = \frac{5.981 \times \left[ O_D(V) \pm \frac{\sigma}{\sqrt{n_{sample}}} \right]}{(q_\infty \pm \Delta q_\infty) (S_{ref} \pm \Delta S_{ref})} \quad (4.2)$$

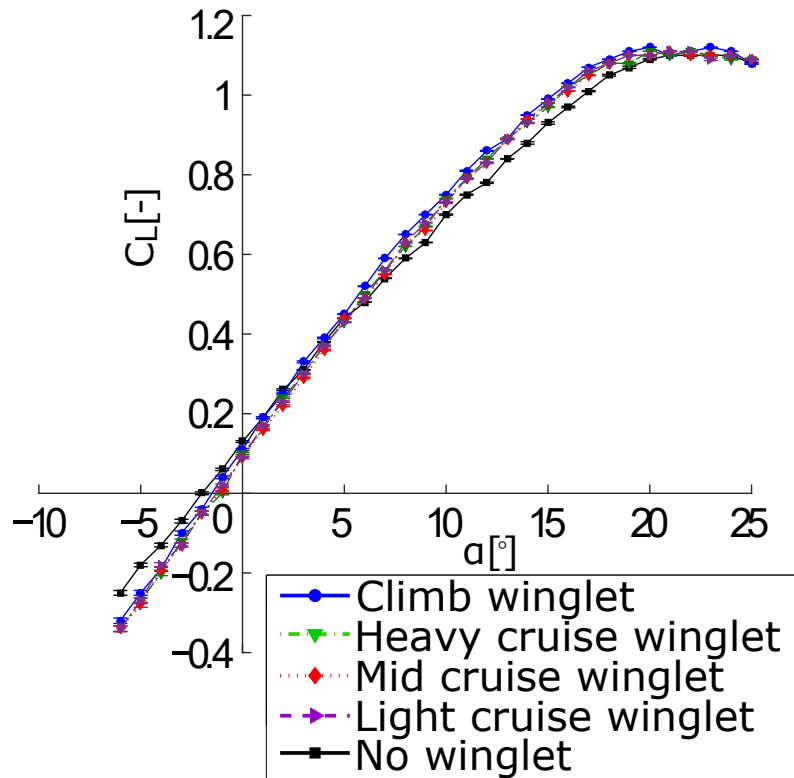
$$\frac{C_L}{C_D} \pm \Delta \frac{C_L}{C_D} = \frac{5.469 \times \left[ O_L(V) \pm \frac{\sigma_L}{\sqrt{n_{sample}}} \right]}{5.981 \times \left[ O_D(V) \pm \frac{\sigma_D}{\sqrt{n_{sample}}} \right]} \quad (4.3)$$

Propagation of uncertainty is made using multiplication and division equations:

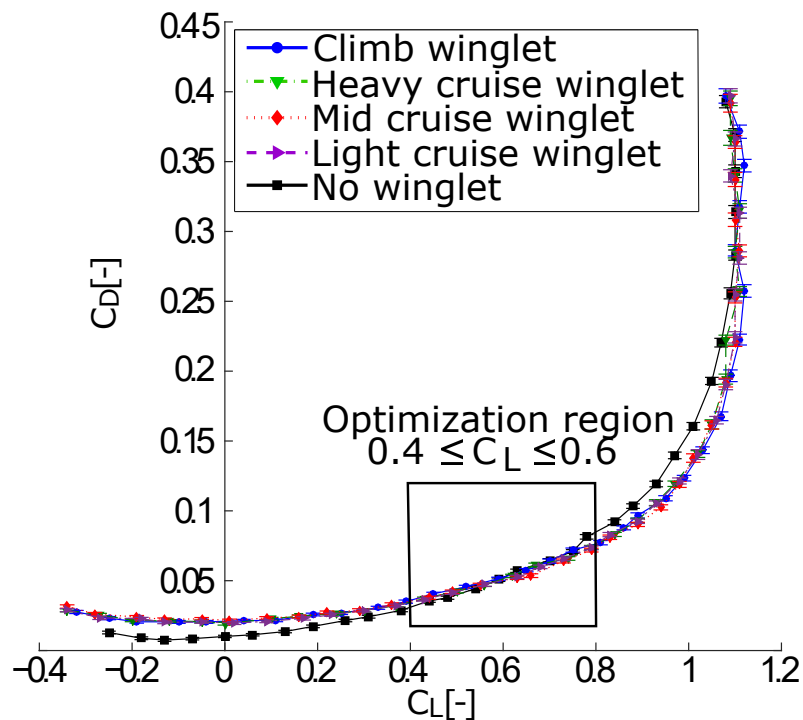
$$(A \pm \Delta A) \times (B \pm \Delta B) = AB \pm A\Delta B \pm B\Delta A \quad (4.4)$$

$$\frac{A + \Delta A}{B + \Delta B} = \frac{A}{B} \pm \frac{A\Delta B + B\Delta A}{B^2} \quad (4.5)$$

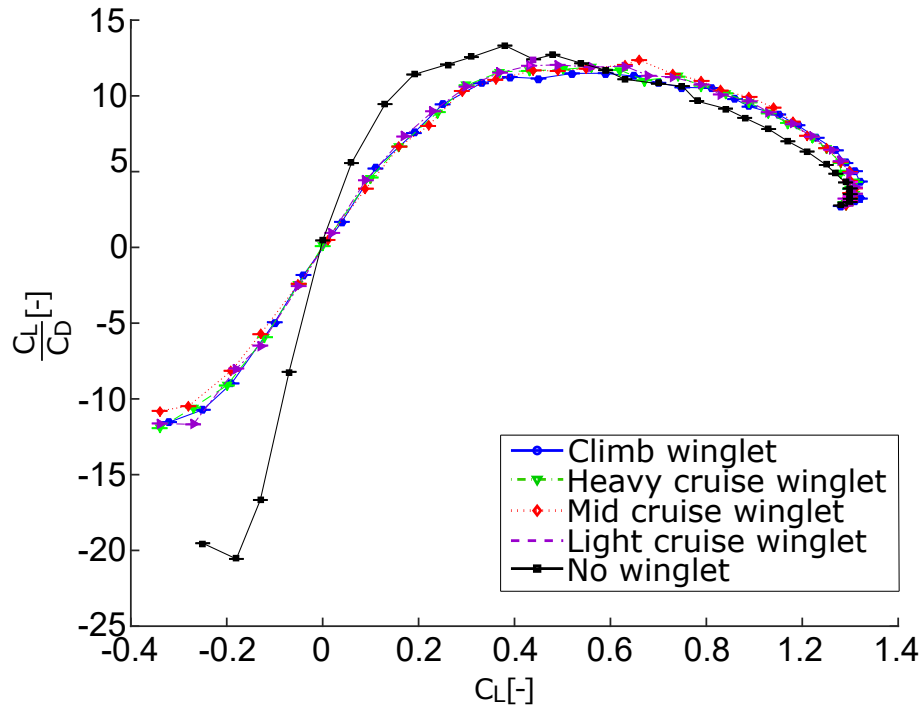
The model frontal area corresponds to less than 8% of test section area, implying negligible alpha, lift and drag variations due to the wind tunnel closed section (LAI et al., 2012). Figures 47 to 49 shows the comparison of the lift and drag coefficients; and lift to drag ratio of the four winglets and wing with no winglet.

Figure 47: Lift coefficient comparison for  $Re = 2.5 \times 10^5$  and  $M = 0.07$ 

Source: The author

Figure 48: Drag coefficient comparison for  $Re = 2.5 \times 10^5$  and  $M = 0.07$ 

Source: The author

Figure 49: Lift to drag ratio comparison for  $Re = 2.5 \times 10^5$  and  $M = 0.07$ 

Source: The author

The winglets increased the  $C_{L_{max}}$  and  $\frac{L}{D}$  for  $C_L \geq 0.6$ . Looking inside the optimization region ( $0.4 \leq C_L \leq 0.6$ ),  $\frac{L}{D}$  was reduced with winglet installed compared to no winglet configuration (Table 14). This can be explained by the fact the winglets geometries are optimized for a transonic ( $M \geq 0.6$ ) and high  $Re$  flow, different from low  $M$  and  $Re$  flow on wind tunnel experiment. This impact on flow separation, which increases the winglet pressure drag. Also, airfoils with great camber are a problem at transonic conditions, once the camber produces high-speed regions that can produce shock waves and wave drag as consequence. So the optimized winglets did not show the expected performance inside the optimization region at low  $M$  and  $Re$ .

Table 14: Lift coefficient and lift to drag ratio maximum values

	$C_{L_{max}}$ [-]	$\Delta C_{L_{max}}$ [%]	$\frac{C_L}{C_{D_{max}}}$	$\Delta \frac{C_L}{C_{D_{max}}}$ [%]
No tip	$1.10 \pm 0.0011$	-	$13.19 \pm 0.003$	-
Climb winglet	$1.12 \pm 0.0003$	$1.82 \pm 0.08$	$11.48 \pm 0.005$	$-13.00 \pm 0.16$
Heavy cruise winglet	$1.11 \pm 0.001$	$0.91 \pm 0.12$	$11.91 \pm 0.002$	$-9.69 \pm 0.03$
Mid cruise winglet	$1.11 \pm 0.001$	$0.91 \pm 0.25$	$12.31 \pm 0.003$	$-6.67 \pm 0.34$
Light cruise winglet	$1.11 \pm 0.001$	$0.91 \pm 0.26$	$11.95 \pm 0.003$	$-9.39 \pm 0.38$

Source: The author

In addition, operating outside its optimal point results on a configuration which parasite drag increase due winglet installation is greater than induced drag reduction

(Figure 9). The wing equipped with the winglets presents less drag at higher lift coefficients, when induced drag is greater than the parasite drag. The winglet optimized for mid cruise condition presented the maximum lift to drag ratio, being considered the best configuration.

## 4.2 Wake mapping

### 4.2.1 Methodology

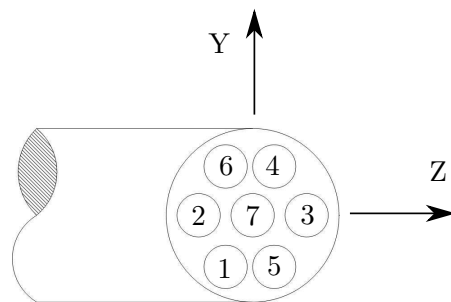
In order to get further insight on winglet effect on wing tip flow and induced drag, a seven-hole probe was used to measure the velocities components on a plane behind the wing tip trailing edge.

Seven-hole probe flow mapping technique consists of using seven holes on the probe (Fig. 50) to measure pressure on the model wake. A relation between these pressure measurements and flow incidence angles are established using a previous probe calibration.

The seven-hole probe calibration for low flow incidence angles ( $\alpha_p, \beta_p \leq 30^\circ$ ) is performed by measuring all the holes total pressures ( $P_{total_i}$ ) at known probe positions on a uniform flow (ZILLIAC, 1993). The probe is positioned using two protractors, defining probe angle relative to wind tunnel Y direction ( $\alpha_p$ ) and Z direction ( $\beta_p$ ). Three pressure coefficients are calculated as shown in Eq. 4.6, where  $P_{total_m}$  is the mean of all pressures measured by all probe holes.

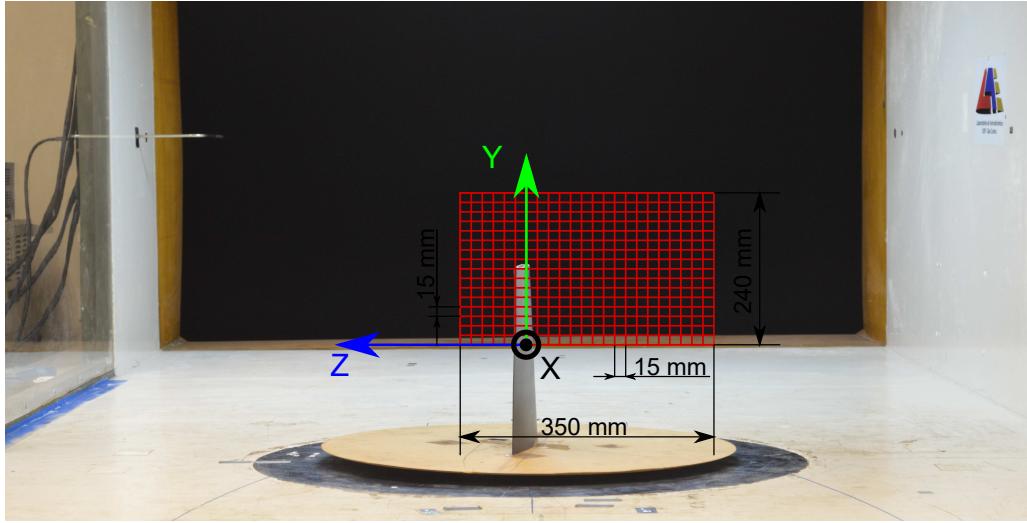
$$C_{p_i} = \frac{P_{total_i} - P_{total_{i+3}}}{P_{total_7} - P_{total_m}} \quad i = 1, 2, 3 \quad (4.6)$$

Figure 50: Seven-hole drawing with wind tunnel coordinates



Source: The author

Figure 51: Wake mapping mesh positioning in relation to the tunnel walls



Source: The author

The holes numbers ( $i$ ) are referred to the probe presented on Fig. 50 and wind tunnel coordinates system is shown in Fig. 51. A database was created to store the groups  $[\alpha_p, \beta_p, C_{p1}, C_{p2}, C_{p3}]$  that relate the flow angle with the pressure on the probe holes. A neural network was trained using pressure for incidence angle data varying  $1^\circ$  in relation to both Y and Z directions. This network is used to find flow incidence angles  $\alpha_p$  and  $\beta_p$  that corresponds to measured values of  $C_{p_i}$ . The velocity components intensity is calculate using Eq. 4.8 using the total pressure and incidence angles data.

$$\frac{V}{U_\infty} = \sqrt{\max\left(\frac{P_{total_i} - P_{total_\infty}}{q_\infty}\right) + 1} = \sqrt{C_{p_{max}} + 1} \quad (4.7)$$

$$[\bar{u}, \bar{v}, \bar{w}] = [\cos(\alpha_p) \times \cos(\beta_p), -\sin(\alpha_p), \sin(\beta_p)] \times \frac{V}{U_\infty} \quad (4.8)$$

The system used on the experiment consists of a Pitot tube upstream the model to measure the total and dynamic pressures; an Aeroprobe L-shaped seven-hole probe; Aeroprobe differential pressure data acquisition hardware (DAQ) and a Dantec traverse system for probe positioning.

The pressure sensors on the DAQ measure the relation between the probe pressure and the Pitot tube total pressure divided by the Pitot tube dynamic pressure. The flow velocity is calculated using Eq. 4.7 from DAQ output.

Wake mapping was performed at a distance of  $c_{ref}$  behind wing tip trailing edge using a mesh points positions ranging from  $-250 \leq Z \leq 100$  mm and  $0 \leq Y \leq 240$  mm with variations of 15 mm on both directions. The mesh points and positioning in relation

to the tunnel walls are shown in Fig. 51. The probe is stopped for 5 seconds on every mesh node to acquire the pressure data.

The wing incidence angle is fixed at  $12^\circ$  at all measurements, resulting in a  $C_L = 0.8$  to aerodynamic balance results. This condition was selected for representing a condition where wing equipped with winglets present higher  $\frac{L}{D}$  than the one with no winglet. Also, at higher  $C_L$  the vortex size and strength are greater and easier to measure and analyse.

#### 4.2.2 Results

The velocity vector field and vorticity map obtained from the seven-hole probe mapping are shown on Fig. 52 to 56. Vortex and wake regions present great variation on velocity direction and intensity, resulting on  $\vec{\omega} \neq 0$ . Vorticity is a indicative of the presence of vortex and wake, once it is defined as:

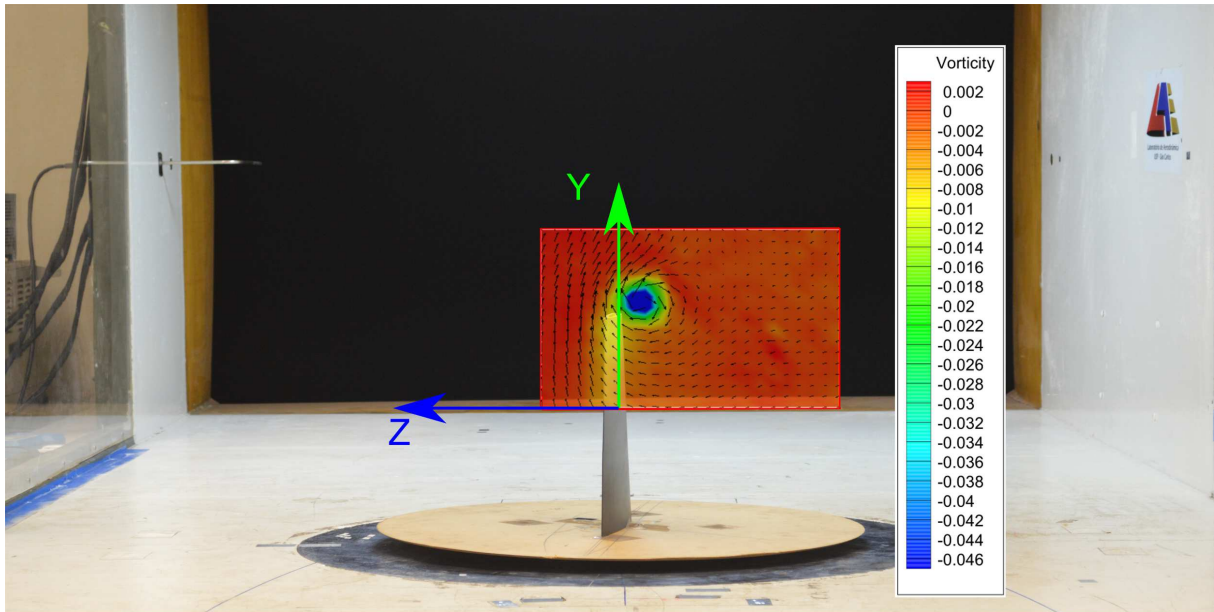
$$\vec{\omega} = \nabla \times \vec{u} \quad (4.9)$$

This way, vorticity maps are a useful method to identify these regions. The induced drag is a function of vorticity, as can be seen from Maskell's equation:

$$C_{D_i} = \frac{\int \int_{wake} \bar{\omega}_x \bar{\Psi} ds}{S_{ref}} \quad (4.10)$$

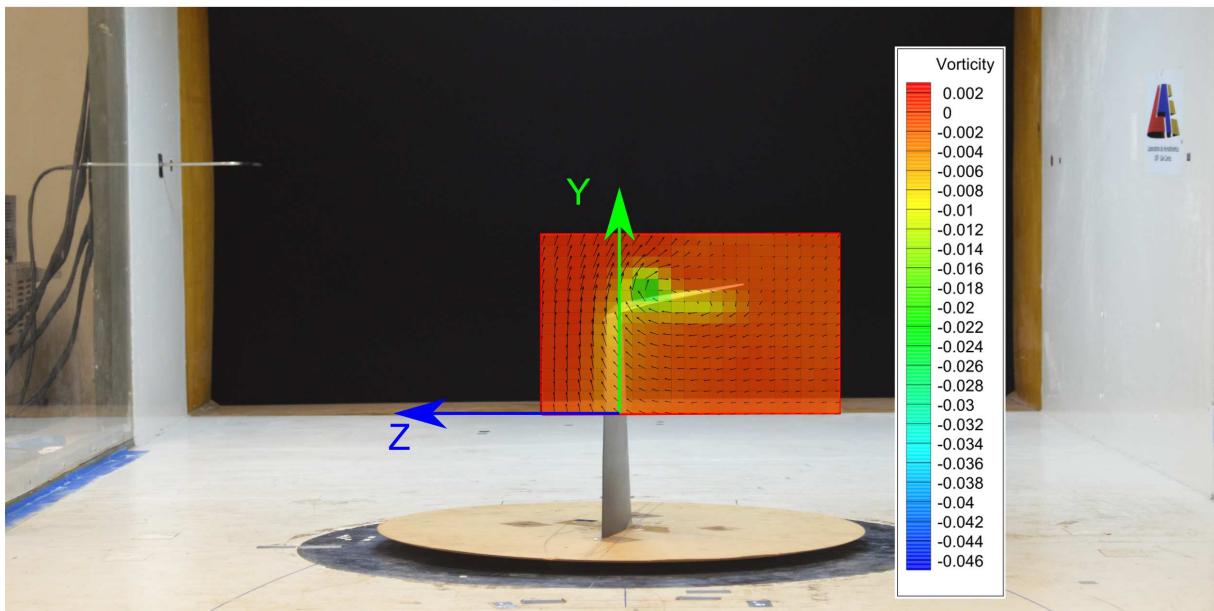
This means that regions with great  $|\omega_x|$  are related to induced drag production. Observing the measured vorticity maps it is visible that the winglets reduced wing tip vortex size and strength, resulting in a lift-induced drag reduction. The velocity vectors show the rotation around the wing tip due to pressure differences from pressure and suction regions.

Figure 52: Vector field and  $\bar{\omega}_x$  on plane at  $c_{ref}$  behind the wing tip trailing edge at  $\alpha = 12^\circ$ ,  $M = 0.07$  and  $Re = 2.5 \times 10^5$  for no tip configuration



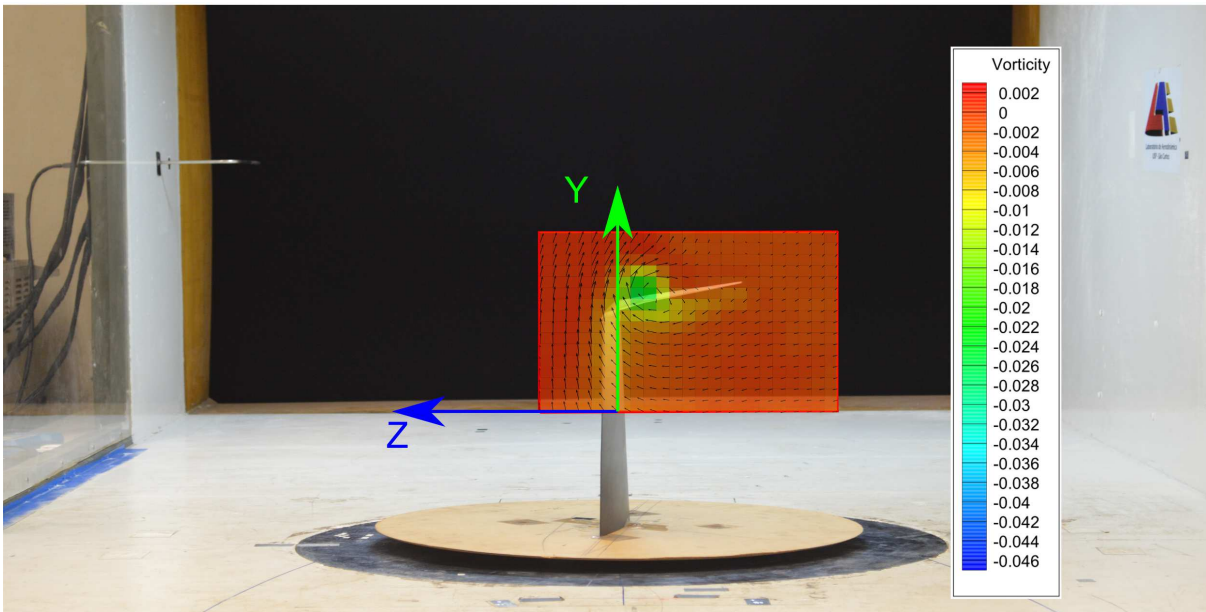
Source: The author

Figure 53: Vector field and  $\bar{\omega}_x$  on plane at  $c_{ref}$  behind the wing tip trailing edge at  $\alpha = 12^\circ$ ,  $M = 0.07$  and  $Re = 2.5 \times 10^5$  for climb configuration



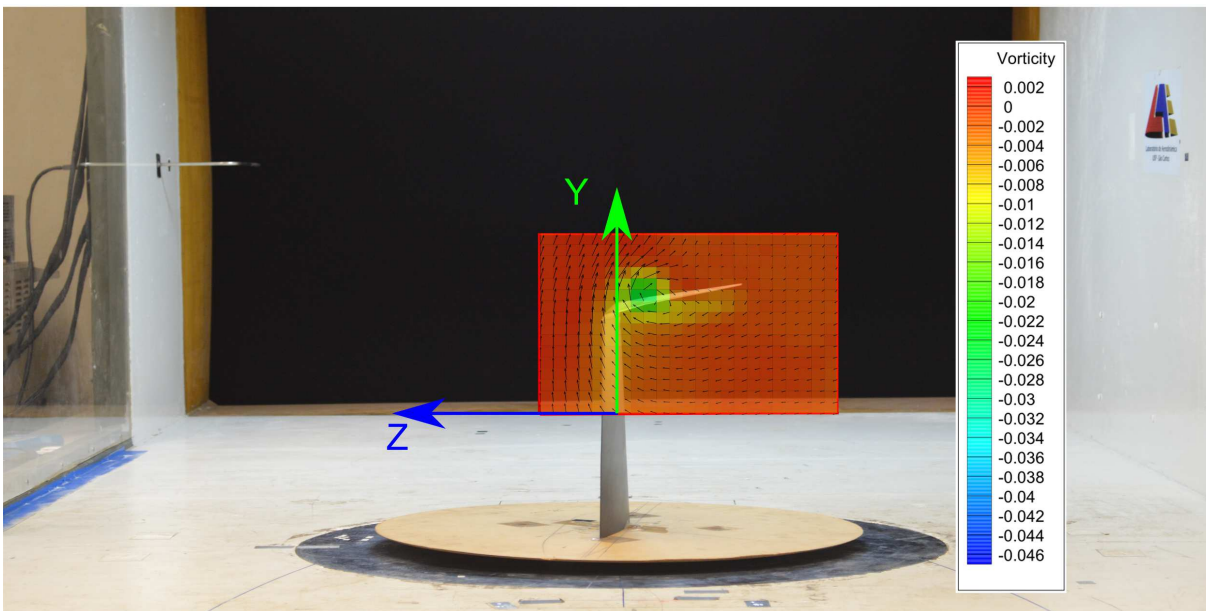
Source: The author

Figure 54: Vector field and  $\bar{\omega}_x$  on plane at  $c_{ref}$  behind the wing tip trailing edge at  $\alpha = 12^\circ$ ,  $M = 0.07$  and  $Re = 2.5 \times 10^5$  for heavy cruise configuration



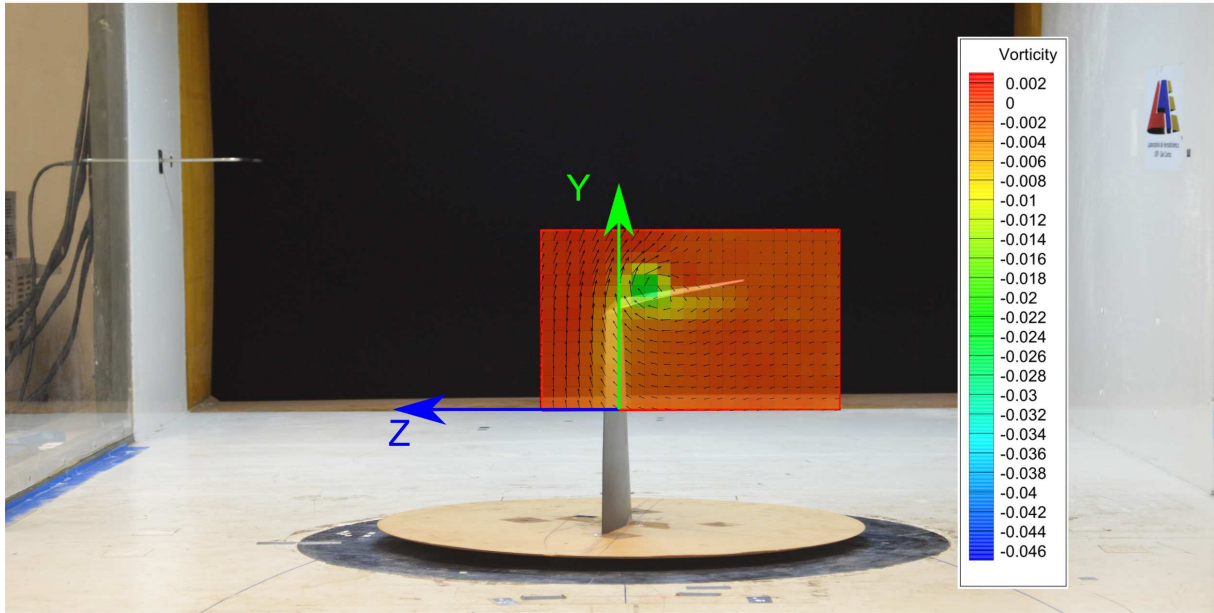
Source: The author

Figure 55: Vector field and  $\bar{\omega}_x$  on plane at  $c_{ref}$  behind the wing tip trailing edge at  $\alpha = 12^\circ$ ,  $M = 0.07$  and  $Re = 2.5 \times 10^5$  for mid cruise configuration



Source: The author

Figure 56: Vector field and  $\bar{\omega}_x$  on plane at  $c_{ref}$  behind the wing tip trailing edge at  $\alpha = 12^\circ$ ,  $M = 0.07$  and  $Re = 2.5 \times 10^5$  for light cruise configuration



Source: The author

An estimative of induced drag can be obtained using Maskell's equations (Eq. 4.15) and is presented in the next section.

### 4.3 Induced drag calculation

Winglets are used to reduce wing drag by using the vortex size and moving it away from tip. They also use the wing tip rotating flow to produce a force that has a component aligned with the flight path. Knowing this, winglets greatly affect wing induced drag. Two methodologies were used to calculate induced drag force measurements and flow mapping results in order to get a deeper look at the effect of different optimized winglets geometries on induced drag and further conclusions on the camber morphing winglet impact on performance.

#### 4.3.1 Drag polar method

Using the drag polar theory presented at (ROSKAM; LAN, 2016), the balance drag data was fitted to a parabolic equation as:

$$C_D = C_{D_0} + kC_L^2 \quad (4.11)$$

$C_{D_0}$  corresponds to the zero lift coefficient and  $k = \frac{1}{\pi A Re}$  is the drag coefficient derivative in relation to lift coefficient squared. A polynomial fit was performed using the

MatLab fitting function. The induced drag is calculated as:

$$C_{D_i} = kC_L^2 = \frac{C_L^2}{\pi AR_e} \quad (4.12)$$

The  $e$  of the wing with no tip is calculated from the  $e = \frac{1}{k\pi AR}$  and  $AR = \frac{b^2}{S_w}$ . It is assumed constant and is used to calculate the  $AR_{eff}$  of configurations with winglets installed. Table 15 shows the calculated values of  $C_{D_0}$ ,  $k$  and  $AR_{eff}$  for different configurations. All winglets showed a reduction on  $k$  when compared to no winglet configuration, presenting an expected increase on wing effective aspect ratio ( $AR_{eff}$ ) and induced drag reduction. The  $C_{D_0}$  increased is due the additional model wetted area added by winglet, resulting on additional parasite drag. These results agree with the winglet design theory and examples in literature.

Table 15: Coefficients of parabolic drag polar fit

<b>Winglet configuration</b>	$k$ [-]	$C_{D_0}$ [-]	$AR_{eff}$
No winglet	0.1090	0.01308	4.73
Climb configuration	0.0904	0.02098	5.67
Heavy cruise configuration	0.0872	0.02095	5.87
Mid cruise configuration	0.0859	0.02114	5.96
Light cruise configuration	0.0886	0.01995	5.78

Source: The author

Analysing induced drag at  $M = 0.07$ ,  $Re = 2.5 \times 10^5$  and  $\alpha = 12^\circ$ , corresponding around  $C_L = 0.8$ , it is possible to see that all configurations, except climb configuration reduced induced drag as expected (Table 16). Mid cruise optimized winglet showed the greatest induced drag reduction.

Table 16: Induced drag at  $M = 0.07$ ,  $Re = 2.5 \times 10^5$  and  $\alpha = 12^\circ$  calculated using parabolic drag polar fit

<b>Winglet configuration</b>	$C_{D_i}$ [-]	$\Delta C_{D_i}$ [%]
No winglet	0.0679	-
Climb configuration	0.0669	0.90
Heavy cruise configuration	0.0615	-7.24
Mid cruise configuration	0.0609	-8.14
Light cruise configuration	0.0610	-7.99

Source: The author

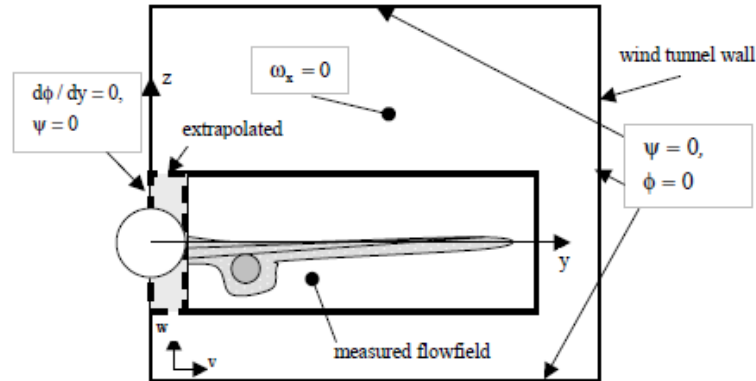
#### 4.3.2 Maskell's equation method

The induced drag was calculated using the Maskell's equation (Eq. 4.15) from wake mapping data (GANZEVLES; BRUIN; PUFFERT-MEIßNER, 2002). This method consists

on calculating the mapped flow stream function ( $\bar{\Psi}$ ) by solving a Poisson's equation (Eq. 4.13) setting  $\bar{\Psi} = 0$  at tunnel walls (Fig. 57) as boundary condition.

$$\frac{\partial^2 \Psi}{\partial z^2} + \frac{\partial^2 \Psi}{\partial y^2} = -\bar{\omega}_x \quad (4.13)$$

Figure 57: Stream function boundary conditions



Source: Ganzevles, Bruin e Puffert-Meißner (2002)

Flow vorticity is calculated using flow velocities components as:

$$\vec{\omega} = \nabla \times \vec{u} \quad (4.14)$$

Equations 4.13 and 4.14 are solved using a second order finite difference scheme. The Maskell's equation uses the vorticity and stream function to calculate the induced drag as:

$$C_{D_i} = \frac{\int \int_{wake} \bar{\omega}_x \bar{\Psi} ds}{S_{ref}} \quad (4.15)$$

This methodology assumes that the vorticity is zero outside the wake region, limiting the integration only to the wake region. The measured vorticity maps (Fig. 52 to 56) shows that the zero vorticity outside wake region is plausible and can be used for that case. Applying the presented methodology, wing induced drag was calculated for  $M = 0.07$ ,  $Re = 2.5 \times 10^5$  and  $\alpha = 12^\circ$ , corresponding around  $C_L = 0.8$ . resulting in a lift-induced drag reduction as shown on Maskell's equation (Eq. 4.15). Table ?? shows  $C_{D_i}$  calculated using Maskell's equation, showing a lift-induced drag reduction for all configurations reaching up to 4.71 %. The winglet optimized for the light cruise condition shows the induced drag reduction.

Table 17: Induced drag calculation methods comparison

<b>Winglet configuration</b>	$C_{D_i}$ [-]	$\Delta C_{D_i}$ [%]
No winglet	0.0679	-
Climb configuration	0.0650	-4.27
Heavy cruise configuration	0.0678	-0.15
Mid cruise configuration	0.0667	-1.77
Light cruise configuration	0.0647	-4.71

Source: The author

### 4.3.3 Methodology comparison

Parabolic equation and Maskell's equation induced drag methods were compared in order to check if the obtained results are similar. Table 18 summarizes the induced drag calculate at Induced drag calculation methods comparison at  $M = 0.07$ ,  $Re = 2.5 \times 10^5$  and  $\alpha = 12^\circ$  using wind tunnel force measuring and flow mapping results.

Table 18: Induced drag calculation methods comparison at  $M = 0.07$ ,  $Re = 2.5 \times 10^5$  and  $\alpha = 12^\circ$

<b>Winglet configuration</b>	<b>Maskell's equation</b>		<b>Parabolic drag equation</b>	
	$C_{D_i}$ [-]	$\Delta C_{D_i}$ [%]	$C_{D_i}$ [-]	$\Delta C_{D_i}$ [%]
No winglet	0.0679	-	0.0663	-
Climb configuration	0.0650	-4.27	0.0669	0.90
Heavy cruise configuration	0.0678	-0.15	0.0615	-7.24
Mid cruise configuration	0.0667	-1.77	0.0609	-8.14
Light cruise configuration	0.0647	-4.71	0.0610	-7.99

Source: The author

The induced drag calculated using Maskell's equation seems to be greater than values calculated using parabolic drag equation. However, the results for climb configuration are contradictory, once Maskell's equation shows that this configuration reaches the second best induced drag reduction while parabolic equation results show a lift-induced drag increase.

Maskell's equation method result quality highly depends on mapping mesh size and pressure sensors precision, while the parabolic equation method result quality depends on balance sensitivity and precision, and fit algorithm quality. Both are good methods for drag components estimation and computational simulations can be used to analyse which of them is more accurate.

## 5 CONCLUSIONS

This study presented an investigation of the impact of using a camber morphing winglet using numerical simulation and wind tunnel experiments.

The genetic algorithm optimization results showed that the camber morphing winglet concept described improved the original winglet reduced total drag by up to 0.58% at climb and heavy, mid and light cruise conditions. A reduction on lift independent drag components occurred for climb, mid and light cruise conditions, showing the concept capability of affecting the total drag in different ways. The winglet airfoil sections evolution showed an expected tendency of reducing the sections camber as the aircraft lift is reduced, being in accordance with the experiments presented by Cerón-Muñoz e Catalano (2006).

The camber morphing winglet mission optimization showed mission fuel consumption reduction of by 4.3% and 7% in comparison with the original winglet for a maximum range (3100 NM) and 1000 NM mission, respectively. A weight sensitiveness analysis revealed that the camber morphing winglet allowed 900 Kg additional load to be carried, having the same fuel consumption as the original winglet. This additional load can be comprised of morphing system weight and extra payload. This shows a performance improvement even when morphing system's negative effects are considered on analysis.

Wind tunnel experiments with winglets optimized geometries gave a deep understanding of this device effects on forces acting on the wing and wing tip vortex structure. The winglets increased wing effective aspect ratio ( $AR_{eff}$ ), reducing induced drag. This increase on the  $AR_{eff}$  was pointed out by wing tip vortex size and strength reduction seen on the flow mapping. Results showed that the winglets increased maximum lift coefficient ( $C_{L_{max}}$ ), however reduced maximum lift to drag ratio ( $\frac{L}{D_{max}}$ ) on optimization region ( $0.4 \leq C_L \leq 0.6$ ). This efficiency reduction can be explained by the fact that winglets geometries were optimized for flow conditions different from wind tunnel experiments, operating outside their optimal point. As a result the parasite drag increase due winglet installation is greater than induced drag reduction at the optimization region. At higher  $C_L$  values, winglet configurations efficiency was greater than no winglet configuration.

Induced drag calculations methods comparison showed that parabolic drag polar method calculated values are smaller than the ones calculated using Maskell's equation. A great difference is seen for climb optimized configuration, the case that Maskell's method found a lift-induced drag reduction and parabolic drag polar found a lift-induced drag increase. Both methods can be used to get insight on how winglet geometry affects drag components and further investigation is necessary to define which one is more accurate.

The concept of the camber morphing winglet proved its capability to improve

aircraft performance. The present analysis brings a potential indication of even better results for concept application on a bigger commercial jet. Investigations are limited only by aerodynamic and performance tools accuracy. Future work can use computational fluid dynamics (CFD) simulations and wind tunnel experiments with a functional camber morphing system at flow conditions closer to real flight, giving a further evaluation of the concept. Also, the optimization process developed in this work is useful to design a winglet for a new aircraft project.

The presented concept shows performance improvement potential using a feasible device. Further analysis must be done for application on the aeronautical industry, but the camber morphing winglet system feasibility and greater certification ease than other morphing structures concepts, once the failure of this system would not compromise the aircraft operation, makes it an interesting research topic. Overall, this work presented a contribution to improving aircraft efficiency and making aviation more sustainable.

## BIBLIOGRAPHY

AGÊNCIA NACIONAL DE AVIAÇÃO CIVIL. **Type Certificate Data Sheet EA-2014T04**. 2014. Disponível em: <<https://sistemas.anac.gov.br/certificacao/produtos/Espec/EA-2014T04-04i.pdf>>. Acesso em: 31 jan. 2019.

Anderson Jr., J. D. **Fundamentals of Aerodynamics**. [S.l.]: McGraw-Hill Education, 2010. ISBN 978-0-07-339810-5.

BARBARINO, S. et al. A review of morphing aircraft. **Journal of Intelligent Material Systems and Structures**, v. 22, n. 9, p. 823–877, jun 2011.

BIRKEMEYER, J.; ROSEMANN, H.; STANEWSKY, E. Shock control on a swept wing. **Aerospace Science and Technology**, Elsevier BV, v. 4, n. 3, p. 147–156, apr 2000.

BLONDEAU, J.; RICHESON, J.; PINES, D. Design of a morphing aspect ratio wing using an inflatable telescoping spar. In: **44th AIAA/ASME/ASCE/AHS/ASC Structures, Structural Dynamics, and Materials Conference**. [S.l.]: American Institute of Aeronautics and Astronautics, 2003.

Boeing Press Release. **Boeing 787 Dreamliner Livery Change Enhances Airplane Performance**. 2006. Disponível em: <[http://www.boeing.com/commercial/news/2006/q3/060710d\\_nr.html](http://www.boeing.com/commercial/news/2006/q3/060710d_nr.html)>. Acesso em: 24 jul. 2019.

BOURDIN, P.; GATTO, A.; FRISWELL, M. I. Aircraft control via variable cant-angle winglets. **Journal of Aircraft**, American Institute of Aeronautics and Astronautics (AIAA), v. 45, n. 2, p. 414–423, mar 2008.

BRASLOW, N. H. D. A. L. **A History of Suction-Type Laminar-Flow Control with Emphasis on Flight Research. Monograph in Aerospace History, No. 13, 1999**. Books Express Publishing, 2011. ISBN 1780393180. Disponível em: <[https://www.ebook.de/de/product/15313079/albert\\_1\\_braslow\\_nasa\\_history\\_division\\_a\\_history\\_of\\_suction\\_type\\_laminar\\_flow\\_control\\_with\\_emphasis\\_on\\_flight\\_research\\_monograph\\_in\\_aerospace\\_history\\_no\\_13\\_1999.html](https://www.ebook.de/de/product/15313079/albert_1_braslow_nasa_history_division_a_history_of_suction_type_laminar_flow_control_with_emphasis_on_flight_research_monograph_in_aerospace_history_no_13_1999.html)>.

BUSCHER, A.; RADESPIEL, R.; STREIT, T. Modelling and design of wing tip devices at various flight conditions using a databased aerodynamic prediction tool. **Aerospace Science and Technology**, Elsevier BV, v. 10, n. 8, p. 668–678, dec 2006.

BUSINESS & COMMERCIAL AVIATION. Update: Business jets specification and performance data. *Aviation Week*, v. 94, maio 2015. Disponível em: <[http://aviationweek.com/site-files/aviationweek.com/files/uploads/2015/05/Business%20Airplane%20Tables\\_May\\_2015\\_revised.pdf](http://aviationweek.com/site-files/aviationweek.com/files/uploads/2015/05/Business%20Airplane%20Tables_May_2015_revised.pdf)>. Acesso em: 31 jan. 2019.

CARTER, D. L. et al. The quest for efficient transonic cruise. In: **7th AIAA ATIO Conf, 2nd CEIAT Int Conf on Innov and Integr in Aero Sciences, 17th LTA Systems Tech Conf, followed by 2nd TEOS Forum**. [S.l.: s.n.], 2007. p. 7812.

CAYIROGLU, I.; KILIC, R. Wing aerodynamic optimization by using genetic algorithm and ansys. **Acta Physica Polonica A**, Institute of Physics, Polish Academy of Sciences, v. 132, n. 3-II, p. 981–985, sep 2017.

CERÓN-MUÑOZ, H. D.; CATALANO, F. M. Experimental analysis of the aerodynamic characteristics adaptive of multi-winglets. **Proceedings of the Institution of Mechanical Engineers, Part G: Journal of Aerospace Engineering**, SAGE Publications, v. 220, n. 3, p. 209–215, mar 2006.

CÉRON-MUÑOZ, H. D. et al. Experimental investigation of wing-tip devices on the reduction of induced drag. **Journal of Aircraft**, American Institute of Aeronautics and Astronautics (AIAA), v. 50, n. 2, p. 441–449, mar 2013.

CHEN, P. C. et al. Variable stiffness spar approach for aircraft maneuver enhancement using ASTROS. **Journal of Aircraft**, American Institute of Aeronautics and Astronautics (AIAA), v. 37, n. 5, p. 865–871, sep 2000.

COIMBRA, R. F. de F. **Influência de dispositivos de ponta de asa no desempenho de um avião agrícola**. 1997. 171 p. Dissertação (Mestrado) — Escola de Engenharia de São Carlos, 1997.

COLLIER, F. **Fundamental.Aeronautics.Program.Subsonic.Fixed.Wing.Project.Reference.Document**. Disponível em: <[https://www.hq.nasa.gov/office/aero/nra\\_pdf/sfw\\_proposal\\_c1.pdf](https://www.hq.nasa.gov/office/aero/nra_pdf/sfw_proposal_c1.pdf)>. Acesso em: 24 jul. 2019.

COSIN, R. et al. Mission adaptive wing optimization with wind tunnel hardware in the loop. In: **13th AIAA/ISSMO Multidisciplinary Analysis Optimization Conference**. [S.l.]: American Institute of Aeronautics and Astronautics, 2010.

De Jong, K. A. **Analysis of the behavior of a class of genetic adaptive systems**. [S.l.], 1975.

DUAN, L.; CHOUDHARI, M. Effects of riblets on skin friction and heat transfer in high-speed turbulent boundary layers. In: **50th AIAA Aerospace Sciences Meeting including the New Horizons Forum and Aerospace Exposition**. [S.l.]: American Institute of Aeronautics and Astronautics, 2012.

ELHAM, A.; TOOREN, M. J. van. Winglet multi-objective shape optimization. **Aerospace Science and Technology**, Elsevier BV, v. 37, p. 93–109, ago. 2014.

ESHELBY, M. **Aircraft Performance: Theory and Practice**. Reston: AIAA, 2000. (AIAA Education Series).

FEDERATION AVIATION ADMINISTRATION - FAA. **14 CFR Part 135 §135.223 IFR: Alternate airport requirements**. 1978. Disponível em: <[https://www.ecfr.gov/cgi-bin/text-idx?SID=5650f99e10b82f8dc0a7d4fdb8af009a&mc=true&node=se14.3.135\\_1223&rgn=div8](https://www.ecfr.gov/cgi-bin/text-idx?SID=5650f99e10b82f8dc0a7d4fdb8af009a&mc=true&node=se14.3.135_1223&rgn=div8)>. Acesso em: 31 jan. 2019.

\_\_\_\_\_. **14 CFR Part 91 §91.167 Fuel requirements for flight in IFR conditions**. 1997. Disponível em: <[https://www.ecfr.gov/cgi-bin/text-idx?c=ecfr&rgn=div5&view=text&node=14:2.0.1.3.10&idno=14#se14.2.91\\_1167](https://www.ecfr.gov/cgi-bin/text-idx?c=ecfr&rgn=div5&view=text&node=14:2.0.1.3.10&idno=14#se14.2.91_1167)>. Acesso em: 31 jan. 2019.

FIELD, J. **The FAA Approves Boeing's 777-X Folding Wingtips**. 2018. Disponível em: <<https://airwaysmag.com/industry/the-faa-approves-boeings-777-x-folding-wingtips/>>. Acesso em: 25 apr. 2019.

- 
- FLORANCE, J. R. et al. Variable stiffness spar wind-tunnel modal development and testing. In: **45th AIAA/ASME/ASCE/AHS/ASC Structures, Structural Dynamics and Materials Conference**. Palm Springs, CA: [s.n.], 2004.
- Gad-el-Hak, M. Compliant coatings for drag reduction. **Progress in Aerospace Sciences**, Elsevier BV, v. 38, n. 1, p. 77–99, jan 2002.
- GAMBOA, P. et al. Optimization of a morphing wing based on coupled aerodynamic and structural constraints. **AIAA Journal**, American Institute of Aeronautics and Astronautics (AIAA), v. 47, n. 9, p. 2087–2104, sep 2009.
- GANZEVLES, F.; BRUIN, A. de; PUFFERT-MEIßNER, W. **A quantitative analysis of viscous and lift-induced drag components from detailed wake measurements behind a half model**. 2002.
- GERN, F. et al. Transport weight reduction through mdo: The strut-braced wing transonic transport. In: **35th AIAA Fluid Dynamics Conference and Exhibit**. Toronto, Ontario Canada: [s.n.], 2005.
- GOLDBERG, D. E. **Genetic Algorithms in Search, Optimization, and Machine Learning**. [S.l.]: Addison-Wesley Professional, 1989. ISBN 0201157675.
- HALPERT, J. et al. Aerodynamic optimization and evaluation of kc-135r winglets, raked wingtips and a wingspan extension. In: **48th AIAA Aerospace Sciences Meeting Including the New Horizons Forum and Aerospace Exposition**. [S.l.]: American Institute of Aeronautics and Astronautics, 2010.
- HETRICK, J. et al. Flight testing of mission adaptive compliant wing. In: **48th AIAA/ASME/ASCE/AHS/ASC Structures, Structural Dynamics, and Materials Conference**. [S.l.]: American Institute of Aeronautics and Astronautics, 2007.
- HEYSON, H. H.; RIEBE, G. D.; FULTON, C. L. **Theoretical parametric study of the relative advantages of winglets and wing-tip extensions**. Washington, DC, 1977. (NASA TP 1020).
- INTERNATIONAL AIR TRANSPORT ASSOCIATION - IATA. **IATA Technology Roadmap**. 2013. Disponível em: <<https://www.iata.org/whatwedo/environment/Documents/technology-roadmap-2013.pdf>>. Acesso em: 31 jan. 2019.
- \_\_\_\_\_. **IATA Fuel Fact Sheet**. 2018. Disponível em: <[https://www.iata.org/pressroom/facts\\_figures/fact\\_sheets/Documents/fact-sheet-fuel.pdf](https://www.iata.org/pressroom/facts_figures/fact_sheets/Documents/fact-sheet-fuel.pdf)>. Acesso em: 31 jan. 2019.
- INTERNATIONAL CIVIL AVIATION ORGANIZATION - ICAO. **Assembly Resolutions in Force A38-18**. 2013. Disponível em: <<https://www.icao.int/meetings/glads-2015/documents/a38-18.pdf>>. Acesso em: 31 jan. 2019.
- JAMESON, A.; CAUGHEY, D. A finite volume method for transonic potential flow calculations. In: **3rd Computational Fluid Dynamics Conference**. [S.l.]: American Institute of Aeronautics and Astronautics, 1977.
- JONES, R. T.; LASLNSKI, T. A. Effect of winglets on the induced drag of ideal wing shapes. **NASA TM 81230**, 1980.

JUPP, J. Wing aerodynamics and the science of compromise. **The Aeronautical Journal**, Cambridge University Press (CUP), v. 105, n. 1053, p. 633–641, nov 2001.

KARAS, O. V.; KOVALEV, V. E. **BLWF 58 User's Guide**. [S.l.; s.n.], 2004.

KHALIL, E. E. et al. Air craft winglet design and performance: Cant angle effect. In: **14th International Energy Conversion Engineering Conference**. [S.l.]: American Institute of Aeronautics and Astronautics, 2016.

KROO, I. Drag due to lift: Concepts for prediction and reduction. **Annual Review of Fluid Mechanics**, Annual Reviews, v. 33, n. 1, p. 587–617, jan 2001.

\_\_\_\_\_. Non-planar wing concepts for increased aircraft efficiency. **VKI Lecture Series on Innovative Configurations and Advanced Concepts for Future Civil Aircraft**, 2005.

LAI, C. et al. Influence of cooling exit flow on aerodynamic performance with different outlet layouts. **International Journal of Vehicle Design**, Inderscience Publishers, v. 59, n. 4, p. 331, 2012.

MAIR, W. A.; BIRDSALL, D. L. **Aircraft Performance (Cambridge Aerospace Series)**. [S.l.]: Cambridge University Press, 1996. ISBN 0521568366.

MANN, A.; ELSHOLZ, I. The m-daw project - investigations in novel wing tip device design. In: **43rd AIAA Aerospace Sciences Meeting and Exhibit**. [S.l.]: American Institute of Aeronautics and Astronautics, 2005.

MARTINS, A. L.; CATALANO, F. M. Drag optimization for transport aircraft mission adaptive wing. **Journal of the Brazilian Society of Mechanical Sciences and Engineering**, FapUNIFESP (SciELO), v. 25, n. 1, p. 1–8, mar 2003.

MCLEAN, J. D.; RANDALL, J. L. Computer program to calculate three-dimensional boundary layer flows over wings with wall mass transfer. **NASA-CR-3123, D6-46976**, 1978.

NEAL, D. et al. Design and wind-tunnel analysis of a fully adaptive aircraft configuration. In: **45th AIAA/ASME/ASCE/AHS/ASC Structures, Structural Dynamics, Materials Conference**. [S.l.]: American Institute of Aeronautics and Astronautics, 2004.

NEAL, D. A.; FARMER, J.; INMAN, D. Development of a morphing aircraft model for wind tunnel experimentation. In: **47th AIAA/ASME/ASCE/AHS/ASC Structures, Structural Dynamics, and Materials Confere**. Newport, Rhode Island: [s.n.], 2006.

NING, A.; KROO, I. Multidisciplinary considerations in the design of wings and wing tip devices. **Journal of Aircraft**, American Institute of Aeronautics and Astronautics (AIAA), v. 47, n. 2, p. 534–543, mar 2010.

OGAWA, H.; BABINSKY, H. Evaluation of wave drag reduction by flow control. **Aerospace Science and Technology**, Elsevier BV, v. 10, n. 1, p. 1–8, jan 2006.

OJHA, S. K. **Flight Performance of Aircraft (Aiaa Education Series)**. [S.l.]: Amer Inst of Aeronautics &, 1995. ISBN 1563471132.

OYAMA, A. et al. Transonic wing optimization using genetic algorithm. In: **13th Computational Fluid Dynamics Conference**. [S.l.]: American Institute of Aeronautics and Astronautics, 1997.

Razvan Apetrei. **Reasons behind the shape of aircraft wings**. 2017. Disponível em: <[www.razvanpetrei.com/reasons-behind-the-shape-of-aircraft-wings](http://www.razvanpetrei.com/reasons-behind-the-shape-of-aircraft-wings)>. Acesso em: 21 jun. 2018.

ROSKAM, J. **Airplane Design Part I : Preliminary Sizing of Airplanes**. [S.l.]: Design, Analysis and Research Corporation (DARcorporation), 2015. ISBN 9781884885426.

ROSKAM, J.; LAN, C. T. **Airplane Aerodynamics and Performance**. [S.l.]: DARcorporation, 2016. ISBN 1884885446.

SAMUEL, J. B.; PINES, D. J. Design and testing of a pneumatic telescopic wing for unmanned aerial vehicles. **Journal of Aircraft**, American Institute of Aeronautics and Astronautics (AIAA), v. 44, n. 4, p. 1088–1099, jul 2007.

SCHRAUF, G. Status and perspectives of laminar flow. **The Aeronautical Journal**, Cambridge University Press (CUP), v. 109, n. 1102, p. 639–644, dec 2005.

SICLARI, M.; NOSTRAND, W. V.; AUSTIN, F. The design of transonic airfoil sections for an adaptive wing concept using a stochastic optimization method. In: **34th Aerospace Sciences Meeting and Exhibit**. [S.l.]: American Institute of Aeronautics and Astronautics, 1996.

SMITH, D. D. et al. Multi-objective optimization for the multiphase design of active polymorphing wings. **Journal of Aircraft**, American Institute of Aeronautics and Astronautics (AIAA), v. 49, n. 4, p. 1153–1160, jul 2012.

SMITH, S. B.; NELSON, D. W. Determination of the aerodynamic characteristics of the mission adaptive wing. **Journal of Aircraft**, American Institute of Aeronautics and Astronautics (AIAA), v. 27, n. 11, p. 950–958, nov 1990.

SZODRUCH, J. The influence of camber variation on the aerodynamics of civil transport aircraft. In: **23rd Aerospace Sciences Meeting**. [S.l.]: American Institute of Aeronautics and Astronautics, 1985.

TAKENAKA, K. et al. Multidisciplinary design exploration for a winglet. **Journal of Aircraft**, American Institute of Aeronautics and Astronautics (AIAA), v. 45, n. 5, p. 1601–1611, sep 2008.

THIERENS, D.; GOLDBERG, D. Convergence models of genetic algorithm selection schemes. In: **Parallel Problem Solving from Nature PPSN III**. [S.l.]: Springer Berlin Heidelberg, 1994. p. 119–129.

THORNTON, S. V. **Reduction of Structural Loads Using Maneuver Load Control on the Advanced Fighter Technology Integration (AFTI)/F-111 Mission Adaptive Wing**. [S.l.], 1993.

URSACHE, N. et al. Morphing winglets for aircraft multi-phase improvement. In: **7th AIAA ATIO Conf, 2nd CEIAT Conf on Innov and Integr in Aero Sciences, 17th LTA Systems Tech Conf followed by 2nd TEOS Forum**. [S.l.]: American Institute of Aeronautics and Astronautics, 2007.

WALL, R. Sketching the a30x. **Aviation Week & Space Technology**, v. 168, n. 5, p. 40, fev. 2008.

WALL, R.; NORRIS, G. Demand driven. **Aviation Week & Space Technology**, v. 169, n. 2, p. 144–145, jul. 2008.

WEISSINGER, J. The lift distribution of swept-back wings. **NACA TM-1120**, abr. 1947.

WHITCOMB, R. T. A design approach and selected wind-tunnel results at high subsonic speeds for wing-tip mounted winglets. **NASA Technical Note D-8260**, ago. 1976.

YU, N. Grid generation and transonic flow calculations for three-dimensional configurations. In: **13th Fluid and Plasma Dynamics Conference**. [S.l.]: American Institute of Aeronautics and Astronautics, 1980.

ZHANG, K. shi; HEPPERLE, M. **Evaluation of the BLWF Code – A Tool for the Aerodynamic Analysis of Transonic Transport Aircraft Configurations**. [S.l.], 2010.

ZILLIAC, G. G. Modelling, calibration, and error analysis of seven-hole pressure probes. **Experiments in Fluids**, Springer Nature, v. 14, n. 1-2, p. 104–120, dec 1993.

## **Appendix**



## **APPENDIX A – BLWF INPUT FILE EXAMPLE**

This appendix shows the input file for the BLWF code. It contains all the flow parameters and geometry information used in this work. The geometry data is proprietary classified. Check Karas e Kovalev (2004) for further information on the input file format and parameters.

```

1  GENERIC_1
2  [ MACH ][ ALPHA ][ BETA ][ RE ][ CAX ][ SW ]
3  0.8124  1.2000  0.0000  1.05E+007  2.6621  21.2668
4  [ ICL ][ CL ][ DCLDA ]
5  0.000  0.600  0.100
6  [ PSE ][ DELWING ][ IBEAM ][ IAIL ][ IROT ][ IBLF ]
7  1.000  0.000  0.000  0.000  0.000  0.000
8  [ PA1 ]
9  0.5000
10 [ PA2 ]
11 1.000
12 [ IBL_W ][ IBL_HT ][ IBL_VT ][ IBL_UG ][ IBL_LG ][ IBL_F ]
13 1.000  0.000  0.000  0.000  0.000  0.000
14 [ REFCHD ][ REFSPN ][ REFLOC ][ REFYCG ][ REFZCG ]
15 2.6621  10.8200  0.2500  9.0000  0.0000
16 -----
17 LOCATION OF THE TRANSITION LINE AND B.L. PARAMETERS
18 FOR WING
19 [ NTR_W ][ VG_W ][ NP_W ][ FLE_W ][ SPANBL_W ]
20 4.000  1.200  11.000  1.000  1.000
21 [ SPAN_W ][ XTRU_WL ][ XTRL_WL ][ XTRU_WR ][ XTRL_WR ]
22 0.000  0.010  0.010  0.010  0.010
23 0.300  0.010  0.010  0.010  0.010
24 0.700  0.010  0.010  0.010  0.010
25 1.000  0.010  0.010  0.010  0.010
26 FOR HORIZONTAL TAIL
27 [ NTR_TH ][ VG_H ][ NP_H ][ FLE_H ][ SPANBL_H ]
28 2.000  1.260  21.000  0.000  1.000
29 [ SPAN_TH ][ XTRU_HL ][ XTRL_HL ][ XTRU_HR ][ XTRL_HR ]
30 0.000  0.020  0.020  0.020  0.020
31 1.000  0.020  0.020  0.020  0.020
32 FOR VERTICAL TAIL
33 [ NTR_TV ][ VG_V ][ NP_V ][ FLE_V ][ SPANBL_V ]
34 2.000  1.260  21.000  0.000  1.000
35 [ SPAN_TV ][ XTR_VL ][ XTR_VR ]
36 0.000  0.020  0.020
37 1.000  0.020  0.020
38 FOR UPPER WINGLET
39 [ NTR ][ VG ][ NP ][ FLE ][ SPANBL ]
40 2.000  1.260  21.000  0.000  1.000
41 [ SPAN ][ XTRI_L ][ XTRO_L ][ XTRI_R ][ XTRO_R ]
42 0.000  0.020  0.020  0.020  0.020
43 1.000  0.020  0.020  0.020  0.020
44 FOR LOWER WINGLET
45 [ NTR ][ VG ][ NP ][ FLE ][ SPANBL ]
46 2.000  1.260  21.000  0.000  1.000
47 [ SPAN ][ XTRI_L ][ XTRO_L ][ XTRI_R ][ XTRO_R ]
48 0.000  0.020  0.020  0.020  0.020
49 1.000  0.020  0.020  0.020  0.020
50 FOR BODY
51 [ XTR_F ][ VG_F ][ NP_F ]
52 0.010  1.200  21.000
53 -----
54 CALCULATION PARAMETERS
55 [ FCONT ][ FCONTM ][ KGMRES ]
56 0.000  0.000  -9.000
57 ----- FOR FIRST MESH -----
58 WING-BODY CALCULATION PARAMETERS
59 [ NIT ][ NORD1 ][ NORD2 ][ FH ]
60 45.000  1000.00  20.000  1.000
61 [ P1W ][ P2W ][ P4W ][ PLWF ][ PHWF ][ FLHWF ][ PWF_WF ]
62 1.000  1.001  1.000  0.700  1.500  4.000  0.300
63 TAIL CALCULATION PARAMETERS
64 [ NIT2_T ][ NIT3_T ][ NORD1_T ][ NORD2_T ]
65 1.000  2.000  1000.000  20.000
66 [ P1T ][ P2T ][ P4T ][ PLT ][ PHT ][ FLHT ]
67 1.2000  1.001  1.000  0.700  1.500  4.000
68 [ PWF_TAL ][ PTAL_WF ][ PTAL_TAL ]
69 1.200  1.200  1.200

```

```

70             NACELLE CALCULATION PARAMETERS
71 [ NIT2_N ] [ NIT3_N ]
72   1.000     4.000
73 [ P1N ] [ P2N ] [ P4N ] [ PLN ] [ PHN ] [ FLHN ]
74   1.200     1.000     1.000     0.050     1.700     4.000
75 [ PWF_NAC ] [ PNAC_WF ] [ PNAC_NAC ]
76   1.200     0.400     0.300
77             CALCULATION PARAMETERS FOR VISCOUS-INVISCID ITERATIONS
78 [ NBL ]
79   7.000
80 [ IBL ]
81   6.000
82   12.000
83   18.000
84   24.000
85   30.000
86   36.000
87   42.000
88 [ PB_W ] [ PB_HT ] [ PB_VT ] [ PB_UG ] [ PB_LG ]
89   1.200     1.200     1.200     1.200     1.200
90 ----- FOR SECOND MESH -----
91             WING-BODY CALCULATION PARAMETERS
92 [ NIT ] [ NORD1 ] [ NORD2 ] [ FH ]
93   48.000     1.000     10.000     0.000
94 [ P1W ] [ P2W ] [ P4W ] [ PLWF ] [ PHWF ] [ FLHWF ] [ PWF_WF ]
95   0.1000     1.002     1.000     0.700     1.500     5.000     0.100
96             TAIL CALCULATION PARAMETERS
97 [ NIT2_T ] [ NIT3_T ] [ NOR1_T ] [ NOR2_T ]
98   1.000     2.000     1.000     10.000
99 [ P1T ] [ P2T ] [ P4T ] [ PLT ] [ PHT ] [ FLHT ]
100   0.100     1.002     1.000     0.700     1.500     5.000
101 [ PWF_TAL ] [ PTAL_WF ] [ PTAL_TAL ]
102   0.200     0.200     0.100
103             NACELLE CALCULATION PARAMETERS
104 [ NIT2_N ] [ NIT3_N ]
105   1.000     4.000
106 [ P1N ] [ P2N ] [ P4N ] [ PLN ] [ PHN ] [ FLHN ]
107   0.100     1.001     1.000     0.050     1.700     4.000
108 [ PWF_NAC ] [ PNAC_WF ] [ PNAC_NAC ]
109   0.200     0.200     0.100
110             CALCULATION PARAMETERS FOR VISCOUS-INVISCID ITERATIONS
111 [ NBL ]
112   14.000
113 [ IBL ]
114   3.000
115   6.000
116   9.000
117   12.000
118   15.000
119   18.000
120   21.000
121   24.000
122   27.000
123   30.000
124   33.000
125   36.000
126   39.000
127   42.000
128 [ PB_W ] [ PB_HT ] [ PB_VT ] [ PB_UG ] [ PB_LG ]
129   0.200     0.200     0.200     0.200
130   0.200
131 -----
132             BOUNDARY LAYER PARAMETERS
133 [ NDF ] [ NVB ] [ CFXMIN ]
134   5.000     2.000     -10.000
135 -----
136             FLOW PLOTTING PARAMETERS
137             FOR WING-BODY
138 [ FPLOT1 ] [ FPLOT2 ] [ FPLOT3 ] [ FPLOT4 ] [ FPLOT5 ] [ FPLOT6 ] [ FPLOT7 ] [ FPLOT8 ]

```

```

138 0.000 0.000 0.000 0.000 0.000 0.000 0.000 0.000
139 [ CPMINW ][ CPMINF ]
140 -2.000 -1.000
141 [ NZOUT ][ NFOUT ][ NXOUT ][ NZOUT_G]
142 20.00 18.000 20.000 7.0
143 [ ZOUT ][ FOUT ][ XOUT ][ ZOUT_G ]
144 0.1260 -180.000 0.050 0.1
145 0.1720 -160.000 0.100 0.2
146 0.2180 -140.000 0.150 0.4
147 0.2640 -120.000 0.200 0.6
148 0.3100 -100.000 0.250 0.8
149 0.3560 -80.000 0.300 0.9
150 0.4020 -60.000 0.350 1.0
151 0.4480 -40.000 0.400
152 0.4940 -20.000 0.450
153 0.5400 0.000 0.500
154 0.5860 20.000 0.550
155 0.6320 40.000 0.600
156 0.6780 60.000 0.650
157 0.7240 80.000 0.700
158 0.7700 100.000 0.750
159 0.8160 120.000 0.800
160 0.8620 140.000 0.850
161 0.9080 160.000 0.900
162 0.9540 0.950
163 0.9800 1.000
164 FOR TAIL
165 [ TPLOTT1 ][ TPLOTT2 ][ TPLOTT3 ][ TPLOTT4 ][ TPLOTT5 ][ TPLOTT6 ][ TPLOTT7 ][ TPLOTT8]
166 0.000 0.000 0.000 0.000 0.000 0.000 0.000 0.000
167 [ CPMINT ]
168 -2.000
169 [ NZOUT ]
170 6.000
171 [ ZOUT ]
172 0.150
173 0.250
174 0.400
175 0.600
176 0.800
177 1.000
178 FOR NACELLE
179 [ NPLOTT4 ]
180 0.000
181 [ CPMINN ]
182 -2.400
183 [ NFOUT ]
184 6.000
185 [ FOUT ]
186 0.000
187 90.000
188 180.000
189 225.000
190 270.000
191 315.000
192 ISOBAR LEVELS
193 [ NCPOUT]
194 20.000
195 [ CPOUT ]
196 -1.500
197 -1.400
198 -1.300
199 -1.200
200 -1.100
201 -1.000
202 -0.900
203 -0.800
204 -0.700
205 -0.600
206 -0.500

```

```

207 -0.400
208 -0.300
209 -0.200
210 -0.100
211 0.000
212 0.100
213 0.200
214 0.300
215 0.400
216 -----
217 MESH PLOTTING PARAMETERS
218 FOR WING-BODY
219 [ FPICT1 ][ FPICT2 ][ FPICT3 ][ FPICT4 ][ FPICT5 ][ FTP1 ][ FTP3 ]
220 0.000 0.000 0.000 0.000 0.000 1.000 0.000
221 [ XMIN ][ XMAX ][ YMIN ][ YMAX ][ ZMIN ][ ZMAX ]
222 -1.000 19.000 -10.000 10.000 0.000 30.000
223 FOR TAIL
224 [ FTPICT1 ][ FTPICT2 ][ FTPICT3 ][ FTPICT4 ][ FTPICT5 ]
225 0.000 0.000 0.000 0.000 0.000
226 [ XMIN ][ XMAX ][ YMIN ][ YMAX ][ ZMIN ][ ZMAX ]
227 10.000 20.000 -5.000 5.000 0.000 20.000
228 FOR NACELLE
229 [ FNP ICT1 ][ FNP ICT2 ][ FNP ICT3 ][ FNP ICT4 ][ FNP ICT5 ]
230 0.000 0.000 0.000 0.000 0.000
231 -----
232 WING/BODY MESH PARAMETERS AND WING POSITION
233 [ NY ][ NZ ][ NT ][ NTN1 ][ NTN2 ][ NY_BETA ]
234 14. 20. 14. 4.000 0.000 1.000
235 [ NXS ][ NXW1 ][ NXW2 ][ NXW3 ]
236 32.000 13.000 6.000 6.000
237 [ XW12 ][ PXW12 ][ XW23 ][ PXW23 ]
238 19.000 0.700 23.000 1.000
239 [ PZROOT ][ PZTIP ][ PXLE ][ PXTE ][ PYTE ][ PZA ][ PZB ]
240 1.000 0.250 1.000 2.000 1.000 -0.150 -1.000
241 [ Z1 ][ PZ11 ][ PZ12 ]
242 0.230 1.000 0.450
243 [ Z2 ][ PZ21 ][ PZ22 ]
244 0.650 0.650 0.650
245 [ XLEW ][ YLEW ]
246 7.20556 -1.13744
247 -----
248 HORIZONTAL TAIL MESH PARAMETERS AND HORIZONTAL TAIL POSITION
249 [ ITH ]
250 2.000
251 [ NX_TH ][ NY_TH ][ NZ_TH ][ NT_TH ]
252 96. 10. 16. 10.
253 [ PZROOT ][ PZTIP ][ PXLE ][ PXTE ][ PYTE ]
254 .25 .25 1. 1. 1.
255 [ XRB_TH ][ YRB1_TH ][ YRB2_TH ][ ZRB_TH ]
256 0.5 0.5 1.0 1.5
257 [ XLETH ][ YLETH ]
258 17.42244 3.62843
259 -----
260 VERTICAL TAIL MESH PARAMETERS AND VERTICAL TAIL POSITION
261 [ ITV ]
262 1.000
263 [ NX_TV ][ NY_TV ][ NZ_TV ][ NT_TV ]
264 96. 14. 14. 10.
265 [ PZROOT ][ PZTIP ][ PXLE ][ PXTE ][ PYTE ]
266 .25 .25 1. 1. 1.
267 [ XRB_TV ][ ZRB_TV ][ YRB_TV ]
268 0.5 0.30 1.3
269 [ XLETV ][ YLETV ]
270 13.07403 0.78200
271 -----
272 FIRST NACELLE MESH PARAMETERS AND NACELLE POSITION
273 [ INAC1 ]
274 1.0
275 [ NYN ] [ NZN ]

```

```

276      6.0      8.0
277 [ NXNS ] [ NXNW1 ] [ NXNW2 ] [ NXNA1 ] [ NXNA2 ] [ DXW1 ]
278      12.0     8.0      8.0      2.0      6.0      1.0
279 [ PXLEN ] [ PYTEN ] [ PXTEN1 ] [ PXTEN2 ] [ PXNW1 ] [ PXNW2 ]
280      1.0      1.0      2.0      0.3      4.0      15.0
281 [ Xlern ] [ RB1 ] [ RB2 ] [ RB3 ] [ RB4 ] [ YOB ] [ DYBW ] [ DYBN ]
282      1.00     0.70     0.70     0.50     0.50     0.00     0.0     0.002
283 [ XLEN ] [ YLEN ] [ ZLEN ] [ NIUL ]
284      12.563   0.96     1.880     1.0

```

-----

SECOND NACELLE MESH PARAMETERS AND NACELLE POSITION

```

287 [ INAC1 ]
288      0.000

```

-----

UPPER WINGLET MESH PARAMETERS. WINGLET POSITION.

```

291 [ IG ]
292      1.0
293 [ GAMMA ] [ FI ]
294      6.0000   71.850
295 [ XLEGW ] [ NXLEGW ] [ PXLEGW ]
296      0.4930   16.000   .50
297 [ XTEGW ] [ NXTEGW ] [ PXTEGW ]
298      1.0000   00.000   .50
299 [ NYJTEG ] [ NYJB ] [ NZKB ] [ PZROOTG ] [ PZTIPG ]
300      6.      3.      3.      .50     .25

```

-----

LOWER WINGLET MESH PARAMETERS. WINGLET POSITION.

```

303 [ IG ]
304      0.000

```

-----

WING/BODY DATA

```

307 [ FNS ]
308      4.00000
309 [ Z ] [ XLE ] [ YLE ] [ CHORD ] [ THICK ] [ EPSIL ] [ FSEC ]

```

# GEOMETRY DATA

311  
312  
313  
314  
315  
316  
317  
318  
319  
320  
321  
322  
323  
324  
325  
326  
327  
328  
329  
330  
331  
332  
333  
334  
335  
336  
337  
338  
339  
340  
341  
342  
343  
344

345  
346  
347  
348  
349  
350  
351  
352  
353  
354  
355  
356  
357  
358  
359  
360  
361  
362  
363  
364  
365  
366  
367  
368  
369  
370  
371  
372  
373  
374  
375  
376  
377  
378  
379  
380  
381  
382  
383  
384  
385  
386  
387  
388  
389  
390  
391  
392  
393  
394  
395  
396  
397  
398  
399  
400  
401  
402  
403  
404  
405  
406  
407  
408  
409  
410  
411  
412  
413

# GEOMETRY DATA

# GEOMETRY DATA

414  
415  
416  
417  
418  
419  
420  
421  
422  
423  
424  
425  
426  
427  
428  
429  
430  
431  
432  
433  
434  
435  
436  
437  
438  
439  
440  
441  
442  
443  
444  
445  
446  
447  
448  
449  
450  
451  
452  
453  
454  
455  
456  
457  
458  
459  
460  
461  
462  
463  
464  
465  
466  
467  
468  
469  
470  
471  
472  
473  
474  
475  
476  
477  
478  
479  
480  
481  
482

483  
484  
485  
486  
487  
488  
489  
490  
491  
492  
493  
494  
495  
496  
497  
498  
499  
500  
501  
502  
503  
504  
505  
506  
507  
508  
509  
510  
511  
512  
513  
514  
515  
516  
517  
518  
519  
520  
521  
522  
523  
524  
525  
526  
527  
528  
529  
530  
531  
532  
533  
534  
535  
536  
537  
538  
539  
540  
541  
542  
543  
544  
545  
546  
547  
548  
549  
550  
551

# GEOMETRY DATA

2139  
2140  
2141  
2142  
2143  
2144  
2145  
2146  
2147  
2148  
2149  
2150  
2151  
2152  
2153  
2154  
2155  
2156  
2157  
2158  
2159  
2160  
2161  
2162  
2163  
2164  
2165  
2166  
2167  
2168  
2169  
2170  
2171  
2172  
2173  
2174  
2175  
2176  
2177  
2178  
2179  
2180  
2181  
2182  
2183  
2184  
2185  
2186  
2187  
2188  
2189  
2190  
2191  
2192  
2193  
2194  
2195  
2196  
2197  
2198

-----  
HORIZONTAL TAIL SECTION DATA

-----  
VERTICAL TAIL SECTION DATA

----- (Engine type - ##### ) -----  
NACELLE DATA1

# GEOMETRY DATA

-----  
----- (Engine type - ##### ) -----  
NACELLE DATA2

[ NC ]  
0.000

-----  
UPPER WINGLET SECTION DATA

[ NC ]  
2.0

```
2207 [ ZLE ][ XLE ][ YLE ][ CHORD ][ THICK ][ EPSIL ][ AG ]
2208
2209
2210
2211 -----
2212 LOWER WINGLET SECTION DATA
2213 [ NC ]
2214 0.000
2215 -----
2216 AIRFOIL DATA FOR NACELLES / WINGLETS
2217 [ NA ]
2218 19.000
2219 [ YSYM ][ NU ][ NL ] Section: nacelle up_profile 0
```

2220  
2221  
2222  
2223  
2224  
2225  
2226  
2227  
2228  
2229  
2230  
2231  
2232  
2233  
2234  
2235  
2236  
2237  
2238  
2239  
2240  
2241  
2242  
2243  
2244  
2245  
2246  
2247  
2248  
2249  
2250  
2251  
2252  
2253  
2254  
2255  
2256  
2257  
2258  
2259  
2260  
2261  
2262  
2263  
2264  
2265  
2266  
2267  
2268  
2269  
2270  
2271  
2272  
2273  
2274

# GEOMETRY DATA

2275  
2276  
2277  
2278  
2279  
2280  
2281  
2282  
2283  
2284  
2285  
2286  
2287  
2288  
2289  
2290  
2291  
2292  
2293  
2294  
2295  
2296  
2297  
2298  
2299  
2300  
2301  
2302  
2303  
2304  
2305  
2306  
2307  
2308  
2309  
2310  
2311  
2312  
2313  
2314  
2315  
2316  
2317  
2318  
2319  
2320  
2321  
2322  
2323  
2324  
2325  
2326  
2327  
2328  
2329  
2330  
2331  
2332  
2333  
2334  
2335  
2336  
2337  
2338  
2339  
2340  
2341  
2342  
2343

# GEOMETRY DATA

2344  
2345  
2346  
2347  
2348  
2349  
2350  
2351  
2352  
2353  
2354  
2355  
2356

2357  
2358  
2359  
2360

2361  
2362  
2363  
2364  
2365  
2366  
2367  
2368  
2369  
2370

# GEOMETRY DATA

2371  
2372  
2373  
2374  
2375  
2376  
2377  
2378  
2379  
2380  
2381  
2382  
2383  
2384  
2385  
2386  
2387  
2388  
2389  
2390  
2391  
2392  
2393  
2394  
2395  
2396  
2397  
2398  
2399  
2400  
2401  
2402  
2403  
2404  
2405  
2406  
2407  
2408